Padova University, Padova, Italy

Department of Information Engineering

Ph.D. School in Information Engineering

Section: *Bioengineering* - Cycle: *XXVIII*

Mathematical Modeling of Cellular Mechanisms in Endocrine Secretory Cells

School director: Ch.mo Prof. Matteo Bertocco

Coordinator: Prof. Giovanni Sparacino

Supervisor: Dott. Morten Gram Pedersen

PhD candidate: Ing. Alessia Tagliavini

Mathematical Modeling of Cellular Mechanisms in Endocrine Secretory Cells

ABSTRACT

The endocrine secretory system is a small collection of cells with the specific aim to act like a sensor and to directly or indirectly control the critical functions of different other target cells. Their specific role is to release into circulation different kinds of hormones.

Some endocrine cells release hormones that maintain background levels of the cell metabolism and the chemical "steady state" of the blood. In particular, keeping glucose concentration in the blood within a limited target range of euglycemia [80-120 mg/dl] is a very important task for the endocrine system. Although the endocrine cells involved in the glucose regulatory mechanism are various, it is well known that the pancreatic β-cells secreting the insulin hormone are the direct and main responsible to maintain euglycemia. Indeed, insulin is secreted because of an increased glucose blood concentration in order to induce other cells to metabolize glucose, bringing its blood concentration back under the physiological limited range. There are also other hormones involved in the regulation of the blood glucose level, such as the insulinotropic gut hormones, i.e., glucagon-like peptide-1 (GLP-1) secreted by intestinal L-cells scattered in the intestinal epithelium among enterocytes and other secretory cells. GLP-1, together with other hormones, is responsible for the incretin effect, i.e., it potentates glucose-induced insulin secretion, and is dependent on the presence of nutrients in the lumen of the

small intestine, which is the reason why insulin response when glucose is orally ingested is greater than when glucose is intravenously administrated. Unfortunately, there is still not a complete understanding about the molecular mechanisms underlying the stimulus-secretion coupling in L-cells and about the mechanisms underlying disturbances in pulsatile insulin secretion even though they are early markers of diabetes.

Other endocrine cells respond to specific input and release potent, long acting hormones. A subgroup of this kind of cells are endocrine cells of the pituitary gland (i.e., melanotrophs, lactotrophs, somatotrophs, thyrotrophs, corticotrophs, and gonadotrophs). They secrete a number of hormones in response to input from the hypothalamus. These hormones act on other endocrine glands and other tissues including the brain to regulate, e.g., growth, reproduction, behavior, temperature, and water intake.

Because of the extreme importance of the endocrine system and the need of a deeper understanding of the stimulus-secretion coupling in these cells, a combination of experimental data and mathematical modeling will be exploited to better investigate the cellular mechanisms involved.

All the endocrine excitable cells share common critical features to induce exocytosis: they depolarize after exposure to the stimuli, as a consequence calcium channels open letting the calcium enter into the cell; the increase in calcium concentration triggers the fusion of the vesicles often docked to the membrane releasing their hormone outside the cell.

In this work, for three main representative categories of excitable en-

docrine cells (β-cells, L-cells and pituitary cells), different cellular mechanisms, often associated to the secretion machinery, will be investigated, taking advantage of a combination of mathematical modeling and experimental data.

Regarding the β-cells, the presented work focuses on the effect on the intracellular calcium oscillations, responsible of exocytosis, of reactive oxygen (ROS) and nitrogen species (NOS), which are common products of the mitochondrial electronic chain. In particular, ROS/NOS have been shown to lead disturbances in insulin secretion and β-cell damage. However, ROS/NOS have also been shown to exert a stimulating short-term effect on insulin release. In order to investigate this twofold effect and the cellular mechanisms implied, a previous mathematical model of β-cell Ca^{2+} handling is adapted to MIN6 cells, a pancreatic β-cell line, and used to interpret experimental results. Our experiment and model results suggest a presumed link between ROS/RNS and disturbed pulsatile insulin secretion. Specifically, moderate ROS/RNS levels act on Endoplasmic Reticulum Ca^{2+} handling mechanisms, whereas higher levels of ROS/RNS also target other components involved in creating oscillatory behaviour.

The Thesis moves to pituitary cells, where we analyze the effect on excitation-secretion coupling generated by the two typical electrical behaviors of pituitary cells: continuous spiking and so-called pseudo-plateau bursting. Experimental data show that a greater amplitude of Ca^{2+} fluctuations is associated with the bursting pattern than with spiking. This observation leads to the hypothesis that bursting cells release more hor-

mone than spiking cells. Unfortunately, testing this hypothesis and measuring the secreted hormone level is difficult due to the small size of the cells (<10 μm diameter) and the necessity of using cell populations, which may include both spikers and bursters. Therefore, we use computer simulation to explore this hypothesis. We develop a stochastic mathematical model of single Ca^{2+} channel activity dependent on experimental electrophysiological recordings. The stochastic Ca^{2+} channel gating is then used to simulate the associated buffered Ca^{2+} diffusion with the modeling program CalC (Calcium Calculator). We use the computed submembrane Ca^{2+} profiles at varying distances from the calcium channels to drive an exocytosis model to get the resulting hormone release. We consider scenarios where Ca^{2+} channels were either spatially discrete or located in clusters and vary the distance of the channels from the release sites. We find that bursting is always at least as effective as spiking at evoking hormone release, and is often considerably more effective, even when normalizing to Ca^{2+} influx.

From calcium diffusion and secretion in pituitary cells, we move our interest to the glucose-sensing mechanism and hormone secretion in intestinal L-cells. There are two main mechanisms implicated in glucose-triggered secretion of GLP-1. One mechanism involves glucose metabolism and closure of ATP-sensitive K^+ channels, the other mechanism exploits the electrogenic nature of SGLTs. Glucose uptake is mostly dominated by GLUT2 facilitative glucose transport, and therefore this transporter is mostly involved in the glucose metabolism pathway. In order to elucidate the role of these two possible pathways in a physiological set-

ting difficult to obtained experimentally, we develop a first mathematical time-spatial model of L-cell. In particular we model the electrical activity, the main currents, and other different mechanisms: glucose transportation inside the cell thought transporters SGLT and GLUT2 as well as its diffusion inside the cell; calcium influx and diffusion associated to calcium current; sodium influx and diffusion; ATP production and consumption dependent on glucose concentration. We exploit the whole cell spatial model developed to understand and have a deeper insight into the glucose-sensing mechanism and GLP-1 secretion. The model takes into account the spatial distribution of the cell, and therefore simulations permit to investigate the role of two transporters without the loss of cell polarization. Results suggest that SGLT1 transporter has a crucial role in triggering cell depolarization, and thus allowing Ca^{2+} influx and GLP-1 exocytosis. On the other hand, glucose metabolism alone is not sufficient to trigger cell depolarization, but it likely affects exocytosis machinery, still playing a minor role in GLP-1 secretion.

In conclusion, in this work, we evaluated and investigated the main mechanisms which lead to hormone exocytosis in endocrine cells by means of mathematical models. We examined a subgroup of representative endocrine cells, β-cells, pituitary cells and L-cells, and focused on different aspects linked to specific stimulus-secretion coupling. For each type of cell, we developed or built on mathematical models, by mean of them we explained and interpreted results observed in experiments. Indeed, experiment might have limitations due to different factors, such as the need of specific inhibiting substances; limitation in technologies and the

impossibility to isolate the specific mechanism of interest. In all these cases, mathematical modeling results to be an essential tool to study biological mechanisms.

Modelli Matematici di Meccanismi Cellulari nelle Cellule Endocrine Secretorie

SOMMARIO

Il sistema secretorio endocrino è formato da un insieme di cellule, che hanno l' obiettivo di agire da sensore e direttamente, o indirettamente, di controllare delle funzioni critiche nelle cellule target. Nello specifico, il loro ruolo è quello di rilasciare nella circolazione sanguigna diversi tipi di ormoni.

Alcune cellule endocrine rilasciano ormoni che mantengono il metabolismo della cellula ad un livello basale e la così detta "steady-state" chimica del sangue. In particolare, un compito importante del sistema endocrino è mantenere la concentrazione di glucosio nel sangue nel range di euglicemia [80-120 mg/dl]. Sebbene le cellule endocrine coinvolte nel meccanismo di regolazione del glucosio nel sangue siano diverse, è risaputo che le β-cellule pancreatiche che secernano l'ormone insulina sono le principali responsabili nel mantenere l'euglicemia. Infatti, l'insulina viene secreta dopo un aumento della concentrazione di glucosio nel sangue e il suo effetto é quello di indurre le altre cellule a metabolizzare il glucosio presente nel sangue, riportando la sua concentrazione sotto il valore limite fisiologico. Oltre all'insulina, ci sono anche altri ormoni che agiscono per regolare il livello di glucosio nel sangue, come gli ormoni insulinotropici dell'intestino, per esempio glucagon-like peptide-1 (GLP-1) secreto dalle L-cellule intestinali, situate nell'epitelio intestinale tra gli enterociti e altre cellule secretorie. GLP-1, insieme ad altri

ormoni, è responsabile dell'effetto incretina, effetto che potenzia la secrezione di insulina indotta dal glucosio stimolata dai nutrienti nel lumen dell'intestino tenue, motivo per cui la risposta dell'insulina quando il glucosio é assunto oralmente risulta essere maggiore rispetto a quando è somministrato per via intravenosa. Sfortunatamente, si conosce ancora poco sia riguardo i meccanismi molecolari alla base dell' associazione stimolo-secrezione delle L-cellule e sia riguardo i disturbi nella secrezione dell'insulina pulsatile, pur essendo questi i primi segnali del diabete.

Altre cellule endocrine invece rispondono a specifici input e rilasciano ormoni potenti a lunga durata d'azione. Un sottogruppo di questo tipo di cellule é l'insieme delle cellule endocrine della ghiandola pituitaria (somatotrope, lactotrope, tirotrope, gonadotrope, corticotrope). Queste cellule secernono ormoni quando stimolate dall'ipotalamo. Gli ormoni cosí secreti agiscono su altre ghiandole endocrine e altri tessuti, incluso il cervello, per regolare ad esempio la crescita, la riproduzione, il comportamento, la temperatura, e l'assorbimento di acqua.

Data l'estrema importanza del sistema endocrino e il bisogno di capire piú in profonditá l'associazione stimolo-secrezione in queste cellule, in questa tesi verrá utilizzata una combinazione di dati sperimentali e modelli matematici proprio con l'obiettivo di studiare i meccanismi alla base di questo meccanismo. Tutte le cellule endocrine eccitabili condividono delle caratteristiche comuni per indurre l'esocitosi: si depolarizzano dopo l'esposizione allo stimolo, i canali di calcio voltaggio dipendenti si aprono, permettendo l'ingresso del calcio all'interno della cellula; l'aumento della

concentrazione di calcio induce la fusione delle vescicole che sono ancorate alla membrana rilasciando il loro ormone all' esterno della cellula.

In questa tesi verranno analizzati i meccanismi cellulari implicati nel processo di stimolazione della cellula associato all' esocitosi nelle tre categorie rappresentative di cellule endocrine eccitabili (β-cellule pancreatiche, L-cellule intestinali e cellule pituitarie), utilizzando una combinazione di dati sperimentali e modelli matematici.

Per quanto riguarda le β-cellule, il lavoro presentato si focalizza sull'effetto delle sostanze ossidative sulle oscillazioni del calcio intracellulare, responsabile dell'esocitosi. Le sostanze ossidative e nitrogene, ROS e NOS, rispettivamente, sono prodotti cellulari che si formano durante la catena di trasporto degli elettroni nei mitocondri. In particolare, si è visto che ROS/NOS portano a disturbi nella secrezione di insulina e al danneggiamento delle β-cellule. Tuttavia, é stata anche attribuita a queste sostanze un effetto a breve termine di stimolazione del rilascio di insulina. Per studiare questo duplice effetto e i meccanismi cellulari coinvolti, è stato adattato un modello matematico esistente relativo alle oscillazioni di calcio nelle β-cellule alle cellule MIN6, una linea pancreatica di β-cellule, ed é stato usato per interpretare i risultati sperimentali. I risultati sperimentai e del modello suggeriscono, presumibilmente, un collegamento tra ROS/NOS e i disturbi della secrezione di insulina pulsatile. Nello specifico, livelli moderati di NOS/ROS agiscono a livello di gestione del calcio del Reticolo Endoplasmatico, mentre livelli maggiori di ROS/NOS spesso hanno come target altre componenti che sono responsabili del comportamento oscillatorio.

Il lavoro in seguito si sposta in direzione delle cellule pituitarie, per le quali analizziamo l'effetto di associazione stimolo-secrezione generato da due comportamenti tipici elettrici delle cellule pituitarie: spiking continuo e il cosí detto "pseudo-plateau" bursting. I dati sperimentali mostrano che al pattern del bursting é associata un'ampiezza maggiore delle fluttuazioni del Ca^{2+} rispetto alle fluttuazioni con spiking. Questa osservazione porta a formulare l'ipotesi che quando le cellule fanno bursting rilasciano una quantitá maggiore di ormone. Sfortunatamente, testare questa ipotesi e misurare il livello di ormone secreto è difficile sia per le piccole dimensioni della cellula (dimetro <10 μm) che per la necessità di usare popolazione di cellule che può comprendere sia cellule che fanno bursting che cellule che fanno spiking. Per questo motivo, usiamo simulazioni per valutare questa ipotesi. I dati elettrofisiologici sperimentali dei due pattern misurati nella stessa cellula sono stati utilizzati come ingresso ad un modello matematico per l'attivitá stocastica del singolo canale di Ca^{2+}. L'apertura stocastica del canale di calcio viene poi utilizzata per simulare la diffusione di Ca^{2+} associata utilizzando il programma CalC (Calcium Calculator). In seguito, i profili di Ca^{2+} ottenuti nella regione appena sotto la membrana a varie distanze dal canale di calcio vengono utilizzati per guidare un modello di esocitosi ed ottenere la quantitá di ormone rilasciato corrispondente. Sono stati presi in considerazione sia uno scenario in cui i canali di Ca^{2+} sono distribuiti singolarmente tra la superficie della cellula, sia il caso in cui sono distribuiti suddivisi in cluster e variando la distanza dei canali dal sito di rilascio. Abbiamo trovato che bursting é sempre almeno tanto efficace ad indurre

esocitosi quanto spiking e spesso è piú efficace, anche quando viene normalizzato per la quantitá di Ca^{2+} entrante.

Dalla diffusione del calcio e la secrezione nelle cellule pituitarie, abbiamo spostato il nostro interesse al meccanismo di assorbimento del glucosio e secrezione ormonale nelle L-cellule intestinali. È stato sviluppato il primo modello spazio-temporale delle L-cellule, in particolare è stata modellata l' attivitá elettrica, le principali correnti e altri meccanismi quali il trasporto del glucosio all'interno della cellula attraverso i trasportatori SGLT1 e GLUT2 e la sua diffusione all'interno della cellula; il flusso di calcio associata alla corrente del calcio e diffusione; il flusso del Na^{+} e diffusione all'interno della cellula, e la produzione e l' utilizzo dell'ATP. Questo sistema di simulazione viene utilizzato per capire meglio i meccanismi delle L-cellule, focalizzandosi sul trasporto del glucosio all'interno della cellula sulla relazione tra glucosio e secrezione di GLP1.

In conclusione, in questa tesi sono stati esaminati e studiati attraverso modelli matematici i principali meccanismi che portano all'esocitosi ormonale delle cellule endocrine. Un sottogruppo rappresentativo di cellule endocrine, β-cellule, cellule pituitarie e L-cellule, è stato esaminato, ponendo l'attenzione sui diversi aspetti legati all'accoppiamento specifico stimolo-secrezione. Per ogni tipo di cellula, sono stati sviluppati o adattati dei modelli matematici che sono stati poi utilizzati per spiegare ed interpretare i risultati osservati sperimentalmente. Infatti, gli esperimenti possono avere dei limiti dovuti a diversi fattori come la necessitá di dover utilizzare delle specifiche sostanze inibitorie o alla mancanza di

una tecnologia appropriata, o all'impossibilità di isolare alcuni specifici meccanismi di interesse. É proprio in questi casi che i modelli matematici risultano essere uno strumento necessario e indispensabile per lo studio dei meccanismi biologici.

Contents

1 Introduction

In this introductory Chapter an overview of the endocrine system and its functions in the body will be provided. In particular, a physiological background will be briefly presented about β-cell and L-cell and their pivotal role in diabetes. Physiological functions of specific type of pituitary cells will be concisely illustrated, as well. Moreover, the main steps involved in the exocytosis mechanism will be delineated. Finally, the thesis outline will conclude the Chapter.

1.1 Physiological Background

The secretory endocrine system is a collection of glands that secrete different kind of hormones and control other target cells. Their main functions is to maintain the body's homeostasis: cellular metabolism within physiological levels, glucose and mineral homeostasis, reproduction, sexual development, heart rate and others [1]. The major endocrine glands

are: the pituitary gland, pancreas, pineal gland, thyroid gland, gastrointestinal tract.

The crucial role in regulating the body's machine makes the study of the cellular mechanisms in endocrine secretory cells of pivotal importance. In particular, impairment of these cells lead to serious dysfunctions such diabetes. Therefore, in this work, I try to get a deeper insight into the mechanisms implied during hormone exocytosis. Among all the endocrine secretory cells, I focus my attention on three main representative types of cells: pancreatic β-cells, pituitary cells and intestinal L-cells. Precisely, pancreatic β-cells and intestinal L-cells are specific endocrine secretory cells that are involved in maintaining blood glucose homeostasis, while pituitary cells are responsible of controlling many body functions such as regulating growth as well as reproduction [1].

β-CELLS

Pancreatic β-cells of the islet of Langherans are responsible for insulin secretion in response to increased glucose levels. Insulin is a peptide hormone and it maintains normal blood glucose levels by facilitating cellular glucose uptake, regulating carbohydrate, lipid and protein metabolism. Insulin is secreted from millions of islet cells in coordinated secretory bursts, as a consequence it shows a pulsatile pattern [2]. The stimulus response in healthy subject when glucose is intravenously administrated is biphasic [3]: after a glucose stimulus, there is an initial rapid phase of insulin secretion, due to the release of granules that are ready to fuse to the membrane, followed by a sustained second phase, where new granules are recruited from a reserve pool. However, the insulin response following oral glucose administration is much more variables. The reason of such different responses is that when glucose is orally intake, glucose absorption causes the secretion of series of gastro-intestinal hormones (GLP-1 and GIP) as well as and neural input associated with glucose ingestion modifying the insulin response [4] and slowing glucose rise.

β-cells impairment leads to diabetes mellitus (DM). Specifically, β-cells

dysfunction in type 2 diabetes mellitus (T2DM) is characterized by the near-absent first-phase glucose-induced insulin secretion. The cause of T2DM is a combination of resistance to insulin action, meaning that the tissue is no longer able to properly utilize glucose, and an inadequate compensatory insulin secretory response. This type of diabetes accounts for $\sim$ 90-95% of those with diabetes and most patients with this form of diabetes are obese [5].

Type 1 diabetes mellitus (T1DM) is an autoimmune disorder characterized by the complete impairment of the insulin-producing β-cells in the pancreas. As a consequence, endogenous secretion of insulin is no longer possible leading to life-threatening hyperglycemia and keto-acidosis. This form of diabetes accounts for only 5-10% of those with diabetes [5]. People affected by T1DM require external insulin administration either with daily injections or continuous insulin infusion [6]. Generally T1DM has an autoimmune origin and affects children or young adults, and in fact it is also called "juvenile diabetes".

The consequence of diabetes is the impossibility of maintaining blood glucose level within the euglycemia range of 80-120 mg/dl. Indeed, people with this disease are often subject to both short periods of hypoglycaemia and long period of hyperglycaemia, leading to several complications.

The chronic hyperglycemia of diabetes is associated with long-term damage, dysfunction, and failure of various organs, especially the eyes, kidneys, nerves, heart and blood vassels [5].

Hypoglycemia lead to insufficient glucose delivery to the brain and other neural tissues and usually include symptoms such as warmth and cognitive dysfunction such as confusion and lethargy. They can also progress to more serious impairment. One severe consequence of hypoglycemia is the risk of neurological injury [7].

For the past 80 years, insulin therapy for diabetes has been the only pharmacological alternative. However, keeping euglycemia is a complex mechanism that involves many different hormones and feedback systems. Therefore, insulin therapy substitutes only one of the hormones

involved in this glucose regulatory mechanism. Recently, especially for T2DM a novel therapeutic approach has risen that involves incretin hormones such GLP-1 hormones. Further, alternative treatments, aiming at enhancing endogenous GLP-1 secretion from the intestinal L-cells directly, are under investigation [8, 9] and L-cells function and role related to β-cells will be provided hereafter.

L-CELLS

L-cells are intestinal enteroendocrine cells located within the gastrointestinal mucosa. They act as nutrient sensors to release, among other hormones, the glucagon-like peptide-1, GLP-1. When luminal sugars, amino acids and fatty acids increase in response to meal intake, L-cells secrete GLP-1. Hormone diffuses across the basal lamina and enters the capillaries [9]. GLP-1, together with the other hormone glucose-dependent insulinotropic polypeptide (GIP), is important for the insulinotropic effect or so called incretin effect. The incretin effect induces an augmented glucose-induced insulin secretion, playing a role in keeping the glucose euglycemia. Moreover, GLP-1 inhibits glucagon secretion, which stimulates the hepatic glucose production and as a result would increase blood glucose concentration. In healthy subjects the incretin effects account for 25%-70% of the postprandial insulin release, depending on the food amount [9]. Moreover, the incretin effects slow gastric emptying, and they inhibit acid secretion, regulate appetite and food intake [9].

GLP-1 is quickly metabolized by dipeptidyl -peptidase-4 (DPP-4). The half-life for intravenously administered GLP-1 is short (less than 5 min) since it is rapidly degraded by DPP-4, located on the membrane of the endothelial cells [4]. Because of the rapid GLP1 degradation, DPP-4 inactivates 66%-75% of the GLP-1 before it reaches the portal vein [9], the possibility that the actions of GLP-1 are transmitted both via sensory neurons and GLP-1 receptor, i.e. β-cells, is raised [4].

Impairment of GLP-1 secretion can lead to different pathological conditions such as obesity and type 2 diabetes [4]. Obesity is associated to

GLP-1 secretion because of its role in regulating appetite and food intake, and when reduced may lead to development of such condition. The most important clinical interest in GLP-1 focuses on its role in the development and treatment of T2DM. Advanced T2DM patients show a high reduction or even loss of the incretin effect. Recent studies have established that the glucagonostatic effect may be as important as the insulinotropic effect in keeping blood glucose within physiological range [4].

PITUITARY CELLS

Pituitary gland consists of two functionally and anatomically well distinct entities: the neurohypophysis and adenohypophysis, Fig. 1.1.1. The neurohypophysis consist of posterior pituitary, whilst the adenohypophysis consist of intermediate and anterior pituitary lobe. The posterior pituitary receives direct neural input from the hypothalamus by the terminals of oxytocin and vasopressin neurons. The intermediate lobe is populated by melanotrophs [10].

The anterior pituitary is connected to the hypothalamus through a vascular network called the hypophyseal portal system. This gland is composed of a multiple cell types secreting six of the most important peptide hormones necessary for reproduction, lactation, growth, development, metabolic homeostasis and the response to stress [10].

- Corticotrophs: secrete adrenocorticotropic hormone (ACTH), responsible of the synthesis and release of glucocorticoids from the adrenal cortex
- Somatotrophs: secrete growth hormone (GH)
- Lactotrophs: secrete prolactin, which initiates milk synthesis (PRL)
- Gonadotrophs: secrete two hormones luteinizing hormone (LH) and follicle stimulating hormone (FSH).
- Thyrotrophs: secrete thyroid stimulating hormone (TSH), which

stimulates the synthesis and release of thyroxine and triiodothyronine from the thyroid gland.

These cells are electrically excitable and hormonal secretion from pituitary cells often arises in response to a electrical activity. However, the pattern of electrical activity varies among cells [10, 11].

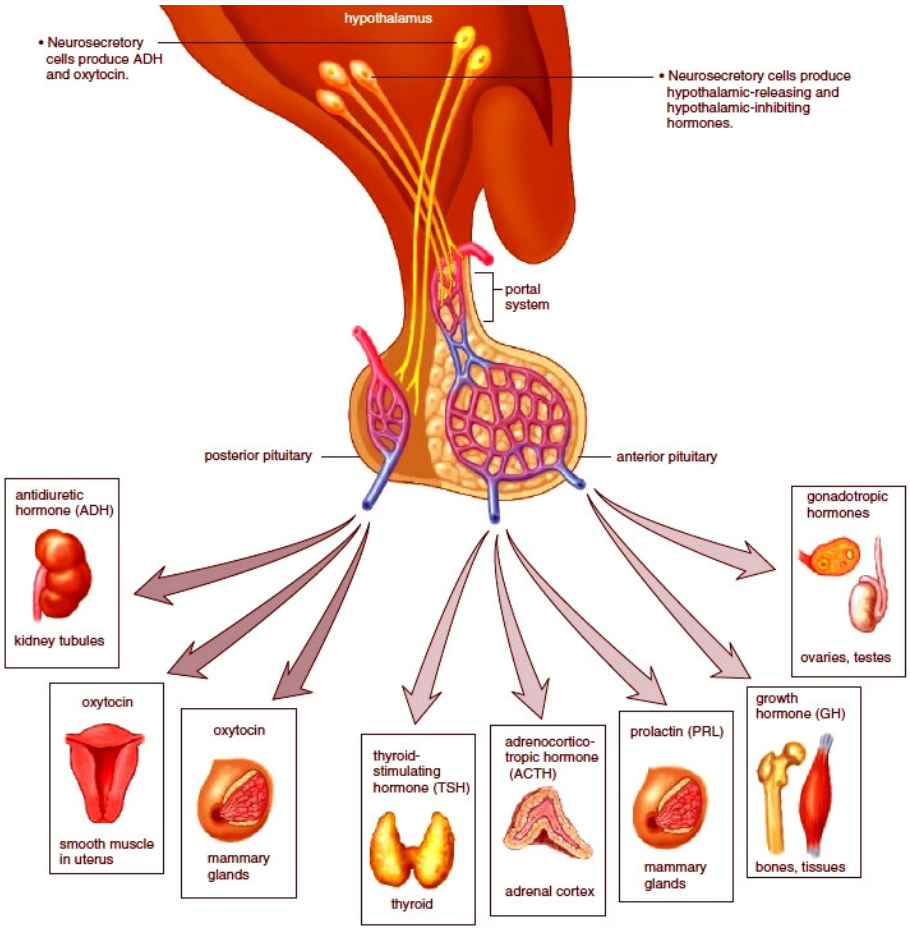

Figure 1.1.1: Connections from the hypotalamus to pituitary gland [11].

1.2 Exocytosis

In endocrine cells, hormone is contained in vesicles, which in response to a series of mechanisms, fused with the membrane and release their

content into the capillary blood. Exocytosis can be firmly regulated to control the vesicle-content release. In this case, granules fusion happens only in response to a physiological signal. In synapses, neurotransmitters are very rapidly released in a controlled manner from synaptic vesicles to mediate neurotransmission [12]. However, there exist a wide range of non neural cell types with numerous distinct physiological function that secrete granules in a regulated way. Among others, pituitary cells, L-cells and β-cells are part of the latter group of regulated secretory cells [12].

Depending on their ability to undergo exocytosis, synaptic vesicles and granules in endocrine cells are divided functionally into a readily releasable pool (RRP) and a reserve pool. The readily releasable granules, are immediately available for secretion and typically consists of 1%-5% of the total number of granules. After exocytosis of these granules, the RRP is resupplied of granules from the reserve pool, however it is still unclear if the process involves physical trans-location of granules within the cell, chemical modification of granules already situated at the membrane or a combination of both processes [13]. The fusion process involves the following steps, Fig. 1.2.1. Initially, the process involves the ATP-dependent priming step and the physical movement of vesicles to the submembrane region of the cell. Then, vesicles dock at release sites of the plasma membrane by the interaction of receptor for N-ethileimide-sensitive attachment (SNARE) proteins, which allow the close approach of the leaflets of the opposite bilayers. After the conversion to a fully releasable state, the mechanism involves triggered membrane fusion, release of granule contents and finally retrieval of the granule membrane [12].

Exocytosis might be triggered by a rise in cytosolic Ca^{2+}. This is the case of Ca^{2+}-triggered exocytosis. The Ca^{2+} rise stimulates vesicles translocation, their docking to the membrane as well as their fusion to the membrane. Moreover, stages after the membrane fusion, such as membrane retrieval and endocytosis, are Ca^{2+} regulated as well. In this case Ca^{2+} can be derived from entry of external Ca^{2+}, by Ca^{2+} release from intracellular Ca^{2+} stores or both [12]. The Ca^{2+} concentration inside the

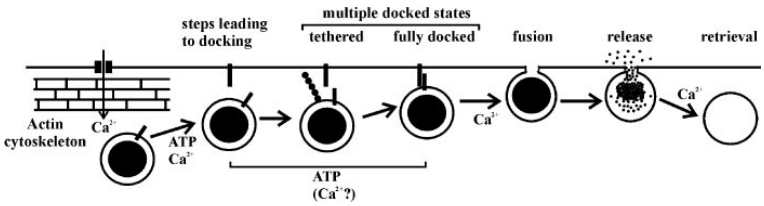

Figure 1.2.1: Schematic representation of the steps leading to secretory granule exocytosis in an neuroendocrine cells undergoing Ca^{2+}-triggered exocytosis. Granules recruitment occurs in a ATP-manner, while fusion and release is controlled by Ca^{2+} [12].

cell can increase in many different ways: second messenger-operated (SMOC), voltage-operated (VOC), receptor-activated (ROC), and Ca^{2+} release-activated (CRAC) Ca^{2+} channels. Moreover, buffering via Ca^{2+} uptake into mitochondria may influence the Ca^{2+} signal. Ca^{+2}-regulated exocytosis is also affected by spatial distribution of channels, Ca^{2+} entry pathways or stores, and local action of Ca^{2+} due to limited diffusion [12].

Basically, exocytosis can be tracked in real time in several different ways. The increase in the surface area of the plasma membrane induced by the granule fusion, can be detected electrically as an increase in plasma membrane capacitance (C_m). Indeed, C_m is the amount of charge needed to change the membrane potential by a fixed amount and therefore is directly proportional to surface area to be charged [1]. For instance, the fusion of a 300-nm-diameter granule with the plasma membrane yields an electrically detectable step in C_m, i.e. 2-3 fF [1]. Other measurements can be amperometric measurement of the release of single granule contents. This method consists in placing a carbon fibre electrode very close to the cell surface and measure the amperometric signal derived by the vesicles fusion. When a single granule releases its content, it results in the generation of a large spike-like signal. Moreover, fusion of secretory granules can be optically detected using total internal reflectance microscopy to collect light emission from a region of a cell near the plasma membrane after the loading of granules with a membrane-permeant fluorescent dye or transfection of the cell with DNA for a fluorescent granule cargo [1].

After exocytosis, three types of exo/endocytosis have been observed

to occur. The first type is the "*Kiss-and-run*", where the granule content is released through the fusion pore that transiently and reversibly opens during exocytosis. In this case, the granule content is released through a narrow fusion pore. The pore can be closed before the granule has fully released its content and without the fusion with the plasma membrane. Another mode is the "*semifusion*" where there is a large opening between the granule and the extracellular space but the granule remains structurally intact. This mode can be referred to as "*cavicapture*". Finally, the third mode is the "*full fusion*", where the granule membrane is integrated into the plasma membrane and the extra membrane is subsequently recaptured by conventional clathrin-mediated endocytosis. All the three possible exo/endocytosis types are shown in Fig. 1.2.2 [3, 14].

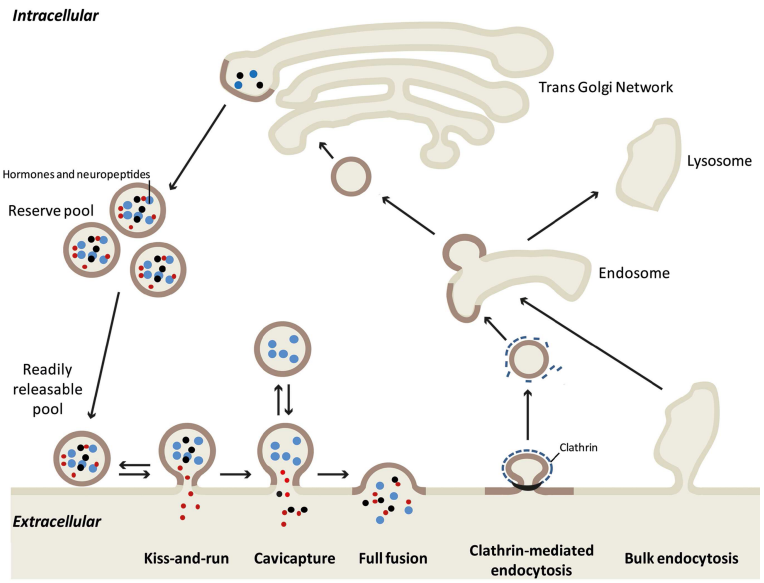

Figure 1.2.2: Different models of exo-endocytosis coupling in secretory cells. During "*Kiss-and-run*" only small molecules are released through a narrow fusion pore, while "*cavicapture*" allow partial release of the granule content. With "*full fusion*" the intra-granule content is all released [14].

By taking into account the experimental error, many different cell types share the Ca^{2+} dependency of Ca^{2+}-triggered granule exocytosis. As a consequence, a common high-affinity Ca^{2+} sensor or a member of closely

related family of Ca^{2+}-binding proteins with similar properties is conceivable. However, differences in certain cell types are still present, especially in synapses. In particular, synapses show a strong link between stimulus and secretion of transmitter, while in other cells such chromaffin cells, the timing of release is not strictly coupled to calcium current kinetics [15].

Despite the remarkable results in understanding the Ca^{2+}-regulated exocytosis machine in endocrine secretory cells, further investigation are still strictly necessary. This is the reason why in this work the role of Ca^{2+} coupled to hormone secretion is investigated, both from a global point of view, considering the whole cell calcium concentration, and from a more localized point of view, considering rise of local Ca^{2+} concentration.

1.3 Thesis Outline

In this section, an overview of the physiological background has been presented. Furthermore, the common steps of hormone-exocytosis in excitable cells have been analysed. The thesis will be focused on modeling different aspects involved in the stimulus-secretion mechanism in three cell types of the endocrine system, β-cell, L-cell and pituitary cell. Electrical activity plays a pivotal role in all these cell types by coupling stimuli to hormone secretion.

Chapter 2 will provide a description of some basic biological and mathematical knowledge with respect to the cell membrane components as well as ionic transportation across it. Furthermore, the first mathematical model of electrical activity in the squid giant axon will be illustrated. The Chapter will also give some basic concepts of diffusion and its mathematical description.

Chapter 3 will focus on the dual effect of reactive oxygen species (ROS) on Ca^{2+} oscillations directly coupled to insulin secretion in β-cells. Both experiments and a mathematical model will be exploited to investigate the disturbances of Ca^{2+} oscillations caused by nitrogen and oxidative species.

We further move our attention to study the stimulus-secretion mechanism in pituitary cell in Chapter 4. In this Chapter real voltage traces measured from gonadotrophs and lacto-somatotrophs are used as input to a stochastic mathematical model of single Ca^{2+} channel or cluster of channels dynamics. The resulting Ca^{2+} profiles obtained from the Ca^{2+} influx and diffusion are used to drive a mathematical exocytosis model.

Finally, a spatio-temporal model of L-cell that combines electrical activity, glucose transportation and metabolism as well as GLP-1 secretion will be presented in Chapter 5 in order to have a deeper insight into the glucose stimuli mechanism underlying GLP-1 secretion.

2

Modeling Basic Cellular Mechanisms

This Chapter has the objective to provide the basic knowledge needed to better understand the next Chapters, in which the modeling of electrical activity in intestinal L-cells and pancreatic β-cells, and the molecules' spatial diffusion inside the cell will be investigated. The first part of the Chapter will give an overview of the biological elements that constitute the cell membrane . Afterwards, a complete description of the structures and mechanisms of transport across the membrane will be presented. The chapter will include the first model of electrical activity in the squid giant axon by Hodgkin and Huxley. Finally, the basic mathematical concept of spatial diffusion will conclude the chapter.

2.1 Basic Biological Elements

Cell Membrane

The cell internal is separated from the external environment by the cell membrane. It is composed of a bilayer of glycerophospholipid molecules. Glycerophospholipids are insoluble in water and the whole membrane is selectively permeable, allowing the passage of some materials and blocking the passage of others (Fig. 2.1.1). Together with lipids, membranes are loaded with proteins. Many of these proteins are embedded into the membrane and protrude on both sides; these are called trans-membrane proteins. In the membrane are also present water-filled pores with diameter of 0.8 nm as well as the so-called channels, which are protein-lined pores that permit the passage of specific ions. Inside the cell and in the extracellular environment, among other substances, there is a dilute aqueous solution of dissolved salts, in $primis$ NaCl and KCl, which dissociate into Na^+, K^+, and Cl^- ions. The membrane task is to maintain homeostasis, that means acting as a barrier of the free flow of ions and keeping their concentration differences. Furthermore, the cell membrane blocks free flow of water. Typical values for intracellular and extracellular ion concentrations are given in Table 2.1.1 [16].

There are two mechanisms of molecules' transportation across the membrane: active and passive. Active transportation makes use of energy to occur, while the passive process is the consequence of the molecules intrinsic random movement. The water is transported across the cell membrane by the $osmosis$ process. Another passive mechanism for small molecules is the simple diffusion though pores and for lipid soluble molecules through the bilipid layer. When the molecules are larger, e.g., sugar molecules, transportation occurs thanks to *carrier-mediated diffusion*. There are also a variety of pumps, which use energy to pump ions against their concentration gradient and we refer to this as active transport. The main function of the active transport is to regulate the intracellular ionic concentration of the cell. As a result of the ionic transportation, the cell gen-

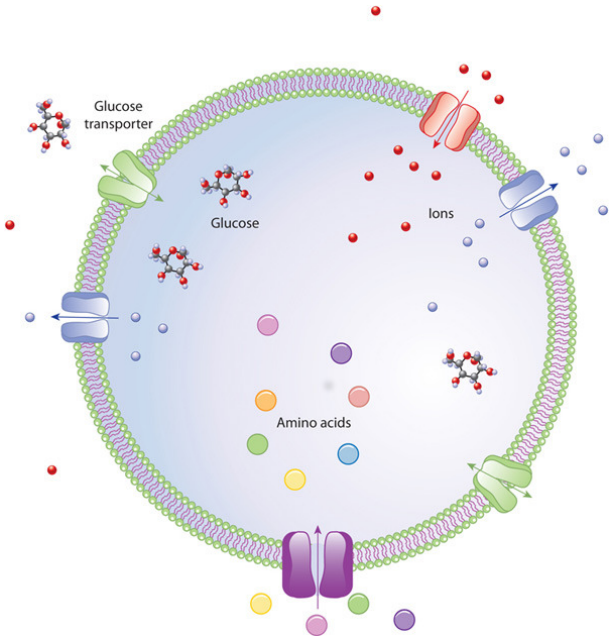

Figure 2.1.1: Cell membrane cartoon representation [17].

Ions	Intracellular Concentration (mM)	Extracellular Concentration (mM)
K^+	139	4
Na+	12	145
Cl^-	4	116
Ca^{2+}	<0.0002	1.8

Table 2.1.1: Typical values for intracellular and extracellular ionic concentration [18].

erates a difference of potential between the inside and the outside of the membrane: the membrane potential [16].

The Membrane Potential

The equation describing the difference potential that can develop across the membrane because of a difference in ionic concentrations is the Nernst equation. In presence of an ion-selective pore that allows only the passage of a specific ion, the specific ion passes through the membrane to

Definition	Abbreviation	Value
Avogadro's number	N	$6.02 \cdot 10^{23}$ 1/mol
Faraday's constant	F	$9.648 \cdot 10^{4}$ C/mol
Elementary charge	e	$1.602 \cdot 10^{-}19$ C
Gas constant	R	8.315 J/(mol · K)
Joule	J	$1\,V \cdot$ C
Volt	V	$1\,J \cdot$ C
Ampere	A	$1\,C \cdot$ s

Table 2.1.2: Important definitions in Electrophysiology.

equilibrate concentration, and at the same time accumulating a negative or positive charge depending on the other ion types. In this case, the membrane acts as a capacitor that is charged by the Nersts potential, given by:

$$\Delta V = V_{Nernst} = \frac{RT}{zF} \ln \frac{[ion]_{out}}{[ion]_{in}}, \tag{2.1}$$

where R and F are given in the Table 2.1.2, T is temperature (in kelvin), and z is the valence of the ion. The Nernst potential represents the equilibrium of the thermodynamic system. Indeed, when the initial starting potential is different from the Nernst potential, or so called reverse potential in electrophysiology, the system tends to move towards the equilibrium potential, resulting in a positive or negative flow of ions. When the ions flow across the membrane the generate a current, in particular from an electronic point of view the current can be described as:

$$I = \frac{V}{R} = gV. \tag{2.2}$$

By defining the $conductance$, $g = 1/R$ as the reciprocal of the resistance, the membrane potential of a cell can be calculate as:

$$V_m = \frac{\sum_i (V_i \cdot g_i)}{\sum_i g_i}, \tag{2.3}$$

where V_i is the Nersts-equation-derived reversal potential for ion i calculated using (2.1) and g_i is the conductance across the membrane for ion i. As we can notice from the (2.3) the resting membrane potential is the weighted average of Nernst potentials for the various ions.

Variations in the cell membrane's permeability to some ions in time result in voltage as well as current changes. The cell membrane can be represented as an electronic circuit. The basic element of the circuit are:

- capacitor: the phospholipid bilayer since it accumulates ionic charge in response to changes in the electrical potential across the membrane.
- resistors: ionic permeabilities of the membrane
- batteries: electromechanical driving force, which drives the ionic current.

Fig. 2.1.2 shows these ionic and capacitive currents arranged in a parallel circuit.

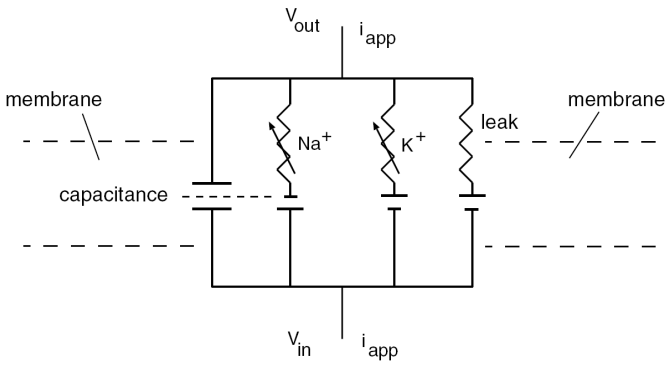

Figure 2.1.2: The equivalent electrical circuit of an electrically active membrane [16]

Since we are interested in how the membrane voltage evolves in time, we focus on the dynamics of the various currents that cross the membrane. The current flow through a single channel, e.g., K^+ channel, can be approximated as:

$$I_K = -g_K(V - V_K), \tag{2.4}$$

where g_K is the conductance of K^+ channels, V_K is the reversal potential determined by the Nernst equation, and $V - V_K$ stands for the driving force across the membrane. By considering also the other ion Na^+ in the cell, the total current is the sum of the individual ionic current:

$$I_{ion} = \sum I_i = \sum -g_i(V - V_i) = -g_K(V - V_k) - g_{Na}(V - V_{Na}). \quad (2.5)$$

The capacitative current across the membrane is:

$$I_{cap} = \frac{CdV}{dt}, \quad (2.6)$$

where V is the membrane potential, and C is the membrane capacitance. By applying the Kirchoff's law of charge conservation to the circuit Fig. 2.1.2:

$$I_{cap} = I_{ion} + I_{app}, \quad (2.7)$$

where I_{app} stands for any currents that could be applied also through experimental manipulation. This lead to:

$$\frac{CdV}{dt} = \sum_i -g_i(V - V_i) + I_{app}. \quad (2.8)$$

The aim now is to solve this differential equation for voltage, that means to find the time and voltage dependence of the various conductances [16].

2.2 Ionic Channels Activation and Voltage Membrane

We can imagine channels as ion selective pores with gates. These gates can be controlled by membrane potential, producing voltage-gated channels, or by chemical ligands producing ligand gated channels or by a combination of them (Fig. 2.2.1).

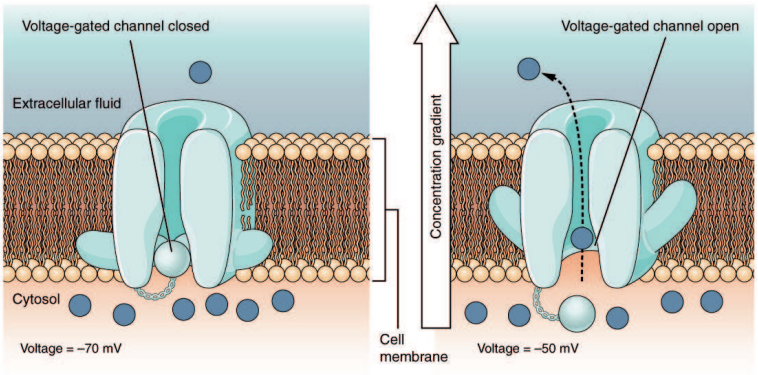

Figure 2.2.1: Voltage gated channel [19]

2.2.1 Voltage-Dependent Gating

The mathematical description of voltage-dependent activation or inactivation gates is based on the mechanism:

$$C \underset{k^-}{\overset{k^+}{\rightleftarrows}} O, \tag{2.9}$$

where C refers to the closed state and O refers to open state of the channel, and k^+ and k^- are the rate constants. The mechanism can be translated into an equation by applying the law of mass action. By defining the fraction of open channels as f_O, the total number of channel as N and the total number of open channels as N_O:

$$f_O = \frac{N_O}{N}, \tag{2.10}$$

in the same way, f_C and N_C refer to the closed state. The number of channels in the closed state is therefore $1 - f_O$. The differential equation associated to (2.9) is:

$$\frac{df_O}{dt} = -k^- f_O + k^+(1 - f_O) = -(k^- + k^+)\left(f_O - \frac{k^+}{(k^- + k^+)}\right). \tag{2.11}$$

By defining:

$$\tau = \frac{1}{k^- + k^+}, \tag{2.12}$$

$$f_\infty = \frac{k^+}{k^- + k^+}, \tag{2.13}$$

we get:

$$\frac{df_O}{dt} = \frac{-(f_O - f_\infty)}{\tau}. \tag{2.14}$$

The ionic channels consist of proteins with charged aminoacids. When the membrane potential changes, the charged aminoacids that drive the closing and the opening of the channel gate can be influenced by this voltage difference. As a result, transition rates between open and closed states, k^+ and k^-, are voltage dependent. In particular the relationship is:

$$k^+ = k_0^+ \exp(-\alpha V) \quad \text{and} \quad k^- = k_0^- \exp(-\beta V), \tag{2.15}$$

where k_0^+ and k_0^- are independent of V. Substituting the relationships in (2.15) into the expressions for f_∞ and τ, rearranging we have:

$$f_\infty = \frac{1}{1 + k_0^-/k_0^+ \exp((\alpha - \beta)V)}, \tag{2.16}$$

$$\tau = \frac{1}{k_0^+ \exp(-\alpha V)} \cdot \frac{1}{1 + k_0^-/k_0^+ \exp((\alpha - \beta)V)}. \tag{2.17}$$

We can define:

$$S_0 = \frac{1}{\beta - \alpha}, \tag{2.18}$$

and:

$$V_0 = \frac{\ln(k_0^-/k_0^+)}{\beta - \alpha}. \tag{2.19}$$

If we substitute S_0 and V_0 into (2.16) and (2.17) we have:

$$f_\infty = \frac{1}{1 + \exp(-(V - V_0)/S_0)}, \tag{2.20}$$

$$\tau = \frac{\exp(\alpha V)}{k_0^+} \cdot \frac{1}{1 + \exp(-(V - V_0)/S_0)}. \tag{2.21}$$

For a fixed value of V, f_∞ is the fraction of channels that open after transient changes and τ is the characteristic time of the transient changes.

During membrane depolarization, the activation gate tends to open and and the inactivation gate tends to close. These two channel gates are translated in the formulation by the sign of S_0: a positive sign determined activation while negative sign determined inactivation. Activation, inactivation and the two correlated characteristic relaxation times τ are shown in Fig. 2.2.2 [16].

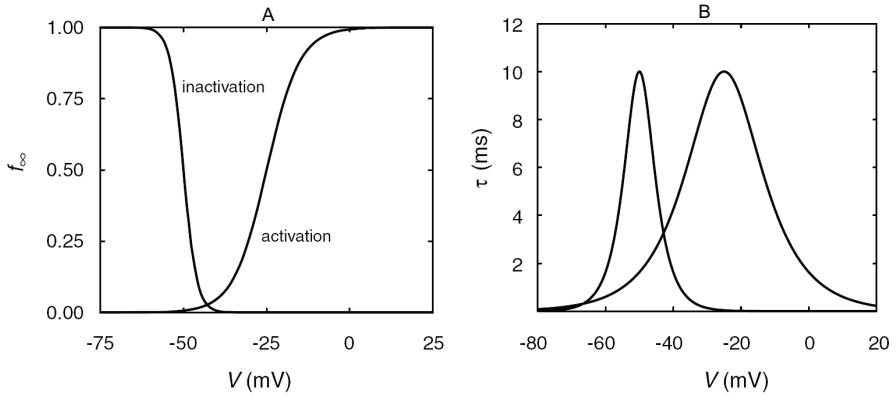

Figure 2.2.2: A) Equilibrium open fraction (f_∞ for an inactivation gate ($V_0 = 50$ mV and $S_0 = -2$ mV) and activation gate ($V_0 = -25$ mV and $S_0 = 5$ mV)) as function of voltage. B) The characteristic relaxation timed τ for the activation and inactivation gates in A) as function of voltage [16].

VOLTAGE CLAMP

The membrane voltage and the ionic currents flowing across the membrane cell can be measured by microelectrodes. In particular, there exists a technique called the $voltage\ clamp$, which permits to establish the activation and inactivation voltage dependence of the ionic conductances. The method consists in maintaining constant the membrane voltage by applying an external current I_{app} that matches the membrane currents. By assuming that the total conductance is the result of the activation of

many channels, g can be defined as the product of the conductance $\bar{g}$ and the fraction of open channel f_0:

$$g = f_0 \bar{g}. \tag{2.22}$$

This new relationship can be added to (2.8), getting:

$$\frac{CdV}{dt} = \sum_i -f_0 \bar{g}(V - V_i) + I_{app}. \tag{2.23}$$

When the external current is equal and opposite to that one flowing across the membrane, that is:

$$I_{app} = \bar{g}\xi(V - V_i), \tag{2.24}$$

the right-hand side of (2.23) becomes zero and the voltage is kept constant. Since V is constant, $\xi = f_0$ and the applied current time course depends only on the time course of f_0 determined by (2.14).

$$\frac{df_O}{dt} = \frac{-(f_O - f_\infty)}{\tau}. \tag{2.25}$$

Therefore, it is possible to have a direct measurement of the gated current by measuring the time dependence of the applied current at a fixed voltage. However, this measure would provide the whole cell gated current without making any difference between the channels. Thus, there is the need to block all but a single type of current and this can be done with specific toxins and pharmacological agents, when possible. Simulation of a voltage clamp experiment is obtained by solving (2.25) and plotting the resulting current in (2.24) with $\xi = f_0$. An example is shown in Fig. 2.2.3A where the membrane potential is clamped at a holding potential (-60 mV), then for a fixed interval, 40 ms, is changed to different potentials, and finally returned to the holding potential. Generally, the value of the holding potential is chosen such that the current through the channel is almost zero. Fig. 2.2.3A shows the current that develops during the protocol for 5 test voltages V_{test}. As mentioned before, the increase

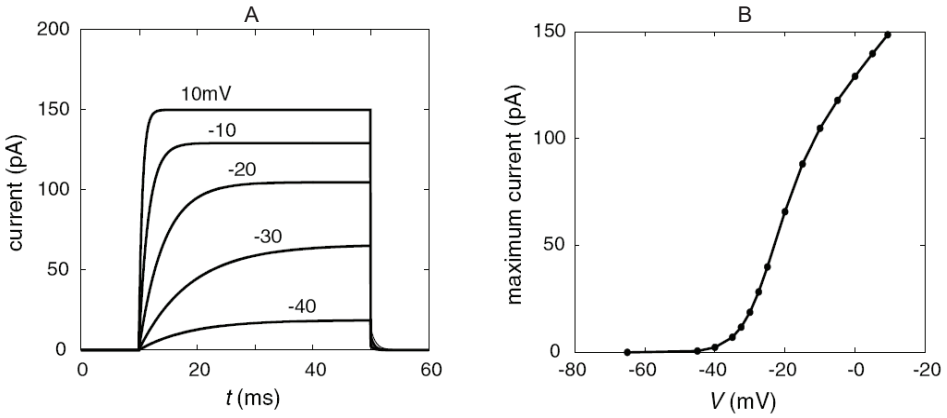

Figure 2.2.3: Simulation of voltage clamp experiment. A) Current records resulting from 40 ms depolarization from the holding potential of -60 mV to the indicated test potentials. B) steady state current as function of test potential. [16]

in current following the voltage clamp at the test value depends on the exponential increase in f_0 with characteristic time $\tau(V_{test})$. When the potential is clamped again at the holding potential the resulting current is called $tail\ current$. Fig. 2.2.3B provides a plot of the steady-state current as function of the test voltage, that is $I = gf_\infty(V_{test} - V_{rev})$ [16].

Current Clamp and Dynamic Current Clamp

Similarly to the voltage clamp, it is possible to inject a constant prescribed positive or negative current into the cell and simultaneously measure the membrane voltage. This technique is referred to as *current clamp*. The method allows the investigator to either depolarize or hyperpolarize the cell, but not to track the conductance changes induced by some stimuli or drug [20]. Recently, a novel technique has been developed "dynamic current clamp". This method allows one to functionally replace a biological ion channel with a virtual conductance, and to study its effect upon cellular electrical behavior. In contrast to the classical current clamp, the dynamic current clamp is a feedback loop: it uses computer simulation to control current injected through the intracellular electrode. The membrane voltage is measured and a current is calculated according to a com-

putational model that includes voltage dependence. The computed current is then injected back into the cell, which in turn changes the voltage and the whole process is repeated in real time. The main steps of the technique are [21]:

1. Record the normal action potential (spiking or bursting).
2. Pharmacologically block the current passing through the studied channel.
3. By using a voltage-dependent kinetic model calculate and inject a current into the cell, using dynamic clamp. Tune the parameter to recover the previous cell activity, even though with differences in frequency and action potential shape.
4. Calculate the difference between the reference and and the dynamic-clamp-generated action potentials.
5. In the case of a small error, the model and the parameters are accepted. In the case of a large error, a new set of parameters is chosen and step 3 is repeated. The optimal parameters research is based on prior knowledge from other experiments and can be automated.

The novel prospective of this method is the possibility of explain not only the biophysical properties of the channel but also the functional behavior of the specific cell [21].

2.3 The Hodgkin-Huxley Model

The first mathematical model describing the ionic basis of the action potential is the Hodgkin-Huxley (HH) model [22]. In order to develop the model, H & H carried out a series of voltage-clamp experiments on the squid giant axon, getting a coupled set of differential equations. The key point of their model is that numerical integration of this coupled set of differential equations leads to the reproduction of the action potential,

even though the model was developed without a molecular understanding of the mechanism. In the model, the ionic current I_{ion} is subdivided into three distinct components: a Na^+ current (I_{Na}), a K^+ current (I_K), and a small leakage current I_L. Their experiments suggest that g_{Na} and g_K are functions of time and membrane potential, while $\bar{g}_l$ can be taken as constant. The current equations are:

$$I_{Na} = g_{Na}(V - V_{Na}), \tag{2.26}$$

$$I_K = g_K(V - V_K), \tag{2.27}$$

$$I_l = \bar{g}_l(V - V_l). \tag{2.28}$$

From their voltage clamp results, Hodgkin and Huxley found that g_{Na} and g_K depend on membrane potential, Fig. 2.3.1 and Fig. 2.3.2. By considering g_K as a variable, they found that for a fixed depolarization value, the conductance evolves sigmoidally, suggesting that potassium conductance has a single activation"gate". A good fit to data in Fig.2.3.1 is achieved by supposing that g_K is proportional to the fourth power of a variable which obeys a first-order equation:

$$g_K = \bar{g_K} n^4, \tag{2.29}$$

$$\frac{dn}{dt} = \alpha_n(1 - n) - \beta_n n, \tag{2.30}$$

where $\bar{g}_K$ is constant, and α_n and β_n are rate constants, which are voltage dependent and not time dependent, n is a dimensionless variable that can vary between 0 and 1. The fourth power was chosen not for physiological reasons, but because it was the smallest exponent that gave acceptable agreement with the experimental data. The meaning of the variable n can be explained by supposing that the gate can be in two states, open/closed as mentioned above and four gates must be open. If we refer to (2.9), α_n and β_n correspond to the rate constants k^+ and k^-.

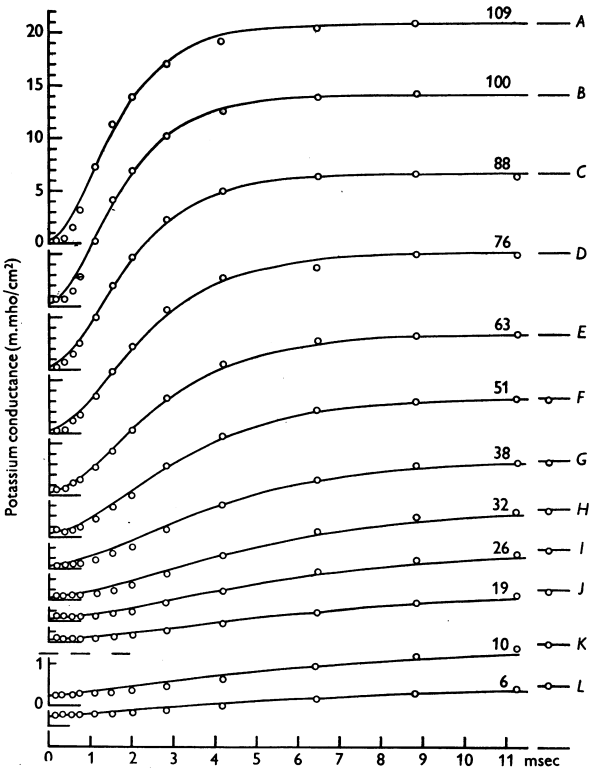

Figure 2.3.1: Conductances changes as function of time at different voltage clamps. The number on each curve gives the depolarization in mV. The circle are experimental points, while the smooth curves are calculated from (2.29)-(2.30) with g_K=0.24 mS/cm^2 [22].

(2.30) can be rewritten as:

$$\frac{dn}{dt} = \frac{n_\infty - n}{\tau_n}, \tag{2.31}$$

$$n_\infty = \frac{\alpha_n}{\alpha_n + \beta_n}, \tag{2.32}$$

$$\tau_n = \frac{1}{\alpha_n + \beta_n}. \tag{2.33}$$

With regards to the g_{Na} conductance, Hodgkin and Huxley deduced that there were two mechanisms: activation and inactivation of the current. Therefore, they represented the ionic conductance as:

$$g_{Na} = \bar{g}_{Na} m^3 h, \tag{2.34}$$

$$\frac{dm}{dt} = \alpha_m(1 - m) - \beta_m m, \tag{2.35}$$

$$\frac{dh}{dt} = \alpha_h(1 - h) - \beta_h h. \tag{2.36}$$

And as above, (2.35)-(2.36) can be rewritten as:

$$\frac{dm}{dt} = \frac{m_\infty - m}{\tau_m}, \tag{2.37}$$

$$m_\infty = \frac{\alpha_m}{\alpha_m + \beta_m}, \tag{2.38}$$

$$\tau_h = \frac{1}{\alpha_h + \beta_h}, \tag{2.39}$$

$$\frac{dh}{dt} = \frac{h_\infty - h}{\tau_h}, \tag{2.40}$$

$$h_\infty = \frac{\alpha_h}{\alpha_h + \beta_h}, \tag{2.41}$$

$$\tau_h = \frac{1}{\alpha_h + \beta_h}. \tag{2.42}$$

Since m is small at rest and first increases, it is referred to as the sodium activation, while h inactivates the sodium current, and therefore it is referred to as the sodium inactivation.

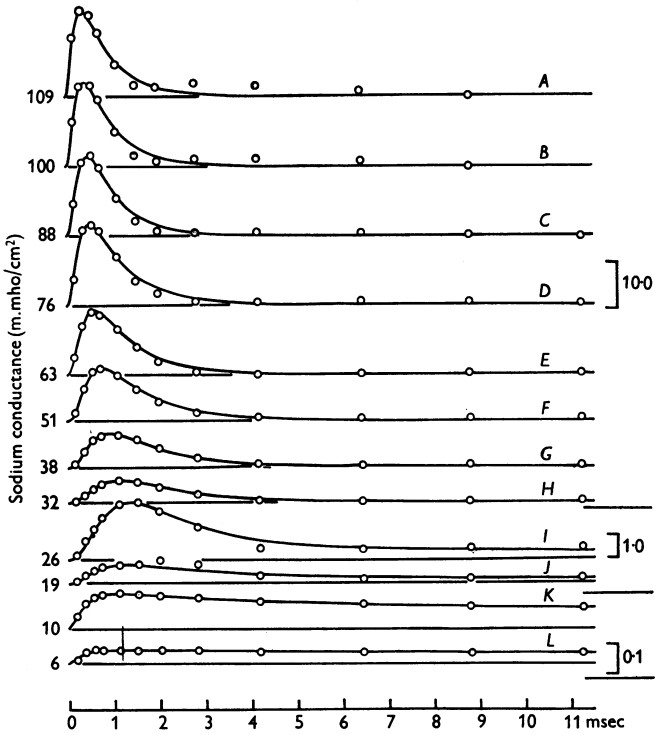

Figure 2.3.2: Changes of sodium conductances associated with different depolarization. The number on each curve gives the depolarization in mV and circles are experimental estimates of sodium conductances. The smooth curves are the model solutions. The vertical scales on the right are in units of mS/cm^2 [22]

In summery the Hodgkin-Huxley equations are:

$$C_m \frac{dV}{dt} = -\bar{g}_K n^4 (V - V_K) - \bar{g}_{Na} m^3 h (V - V_{Na}) - \bar{g}_l (V - V_l) + I_{app}, \tag{2.43}$$

$$\frac{dn}{dt} = \frac{n_\infty - n}{\tau_n}, \tag{2.44}$$

$$\frac{dm}{dt} = \frac{m_\infty - m}{\tau_m}, \tag{2.45}$$

$$\frac{dh}{dt} = \frac{h_\infty - h}{\tau_h}. \tag{2.46}$$

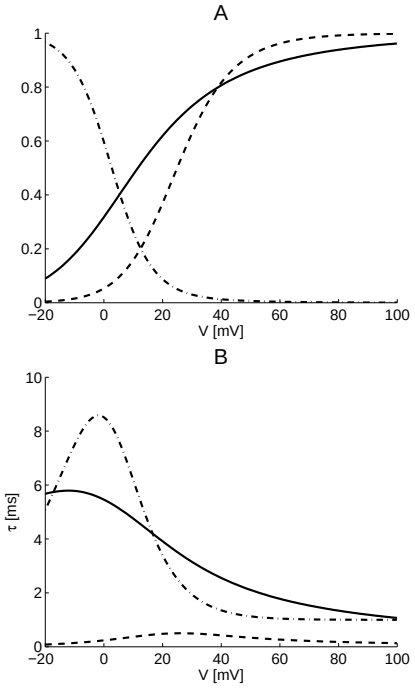

Figure 2.3.3: A) steady state functions: solid line n_∞, dashed line m_∞, dashed-dot line h_∞, B) time constants: solid line τ_n, dashed line τ_m, dashed-dot line τ_h

In Fig. 2.3.3 the steady-state functions and the time constants are shown. Of course it is interesting to understand the mechanisms that lead to the production of an action potential. Since g_{Na} and g_K are not constant, the

different currents influence the potential. In particular, we should focus on the dynamics of m, n, h. τ_m is much smaller than either τ_n or τ_h, meaning that $m(t)$ responds to voltage changes much faster than either n and h. When the applied current is large enough to raise the potential, and therefore to raise m_∞ to a high enough level, m will increase sufficiently to change the sign of the net current, leading to inward sodium current. At this point, the difference in time constants plays a pivotal role. When the potential is at rest, the inactivation h is positive. As the potential increases, h_∞ decreases towards zero and as h approaches zero, the sodium current is inactivated because g_{Na} approaches zero. However, because the time constant τ_h is much larger than τ_m, there is a considerable delay between turning on the sodium current when m increases and turning off the sodium current when h decreases. The two different time scales of m and h implicate that the sodium current is first turned on and later turned off, and this is seen as an initial increase of the potential, followed by a decrease toward rest. While the sodium current inactivates, the outward potassium current is activated, due to the similar time constants τ_h and τ_n. When the potassium current is activated, the potential is driven below the rest towards V_K. In Fig. 2.3.4 simulation of a series of action potential is shown.

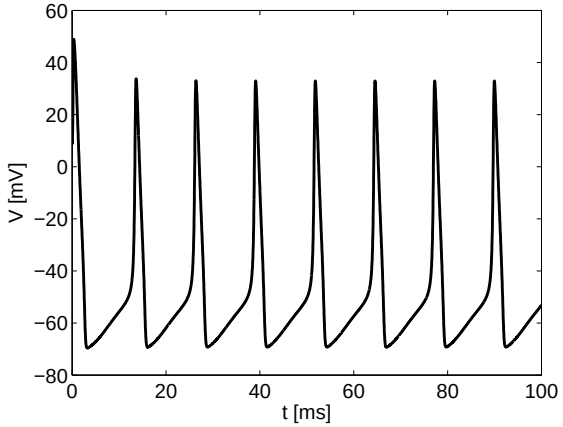

Figure 2.3.4: Simulation of repetitive firing of action potentials

2.4 TRANSPORTERS

Together with ionic channels, there are other cellular mechanisms to transport impermeant species across the membrane. Indeed, many membrane proteins play a role in moving both ions and molecules from inside and outside the cell and $vice\ versa$. Ionic pumps have the task to maintain the concentration imbalance of Na^+, K^+, and Ca^{2+}. In additions to pumps, co-transporters and exchangers are present and have the function to allow ions and small molecules to be transported selectively into internal or external compartments of the cell. In the case of ionic channels the driving force is a passive combination of electrical potential and ionic concentration differences. Furthermore, co-transporters use ionic gradient to transport other molecules, and in this case the carriage still happens without energy consumption and therefore results to be passive. In contrast, when transportation is mediated by pumps it requires expenditure of energy [16, 23].

PASSIVE TRANSPORT

An important example of passive transport is the GLUT transporter. It is responsible for carrying glucose inside and outside the cell. In this case the term passive is used because there is not the consumption of explicit energy such us ATP molecules, but instead background thermal energy is exploited. There exist at least 14 isotypes of GLUT [24], and the isotype GLUT2 transporter is found in glucose-sensing pancreatic beta-cells and intestinal L-cells. GLUT2 can be modeled as a 4-state model Fig. 2.4.1 [16]. In S_1 glucose binds at the exterior of the transporter and it changes state to S_2. In S_2 glucose molecules is bound to the transporter which is still facing thee exterior. In state S_3 the transporter faces the interior. Finally, in S_4 glucose dissociate and it is released inside the cell and the transporter is faced inside the cell. If S_4 translates to S_1 again the cycle can repeat. All of these processes are reversible. The rates of the elementary processes are determined by the *law of mass action*. The transition rate

from S_1 to S_2 is given by [16]:

$$J_{12} = k_{12}[G]_{out}x_1. \tag{2.47}$$

The factor k_{12} is the bi-molecular rate constant with practical unit s^{-1} mM^{-1}, $[G]_{out}$ is the external glucose concentration, and x_1 is the fraction of GLUT transporters $x_1 = N_1/N$ (N_1 number of transporters in state S_1 and N total number of transporters). In the same way, the reverse reaction is given by:

$$J_{21} = k_{21}[G]_{out}x_2. \tag{2.48}$$

The model equations are:

$$\frac{dx_1}{dt} = -k_{12}[G]_{out}x_1 + k_{21}x_2 + k_{41}x_4 - k_{14}x_1, \tag{2.49}$$
$$\frac{dx_2}{dt} = k_{12}[G]_{out}x_1 - k_{21}x_2 - k_{23}x_2 + k_32x_3, \tag{2.50}$$
$$\frac{dx_3}{dt} = k_{23}x_2 - k_{32}x_3 - k_{34}x_3 + k_{43}[G]_{in}x_4, \tag{2.51}$$
$$\frac{dx_4}{dt} = k_{34}x_3 - k_{43}[G]_{in}x_4 - k_{41}x_4 + k_{14}x1, \tag{2.52}$$

The total number of transporters should be preserved, that means that the total fraction of transporters should be equal to 1. In this way, transporters are neither created nor destroyed:

$$x_1 + x_2 + x_3 + x_4 = 1 \tag{2.53}$$

In this way (2.49)-(2.52) can be rewritten as:

$$\frac{dx_1}{dt} = -(k_{12}[G]_{out} + k_{14} + k_{41})x_1 + (k_{21} - k_{41})x_2 - k_{41}x_3 - k_{41}, \tag{2.54}$$
$$\frac{dx_2}{dt} = k_{12}[G]_{out}x_1 - (k_{21} + k_{23})x_2 + k_32x_3, \tag{2.55}$$
$$\frac{dx_3}{dt} = -k_{43}[G]_{in}x_1 + (k_{23} - k_{43}[G]_{in})x_2 - (k_{32} + k_{34} + k_{43}[G]_{in})x_3 - k_{43}[G]_{in}. \tag{2.56}$$

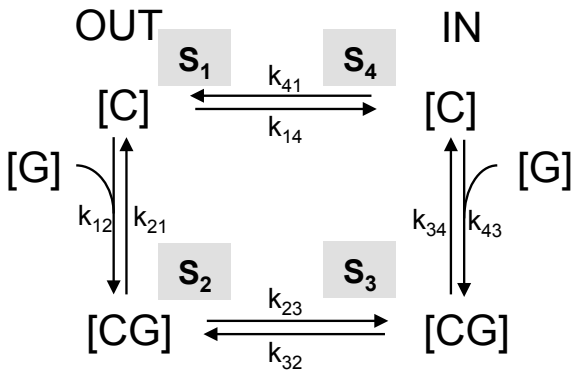

Figure 2.4.1: four-state model of GLUT2 transporter.

Another example of a passive transporter which shares features with the GLUT transporter, is the Na^+/glucose co-transporter (SGLT1). The SGLT1 transporter requires the presence of Na^+ to transport glucose molecules inside the cell. The stoichiometry of the transporter implies that 2 Na^+ molecules bring 1 glucose molecule inside the cell. Thus, when there are no Na^+ molecules outside, no glucose molecules are transported inside. Moreover, the SGLT1 transporter is *electrogenic*, since transport generates an electrical current due to transport of Na^+. The SGLT1 transporter can be modeled as a six-state model, Fig. 2.4.2 [16].
At the beginning, the empty carrier is outside the cell (S_1), then two Na^+ bind to the carrier (S_2) allowing the subsequent association of glucose (S_3). Afterwords, the carrier translocates inside the cell (S_4) and the same symmetrical steps take place inside the cell leading to the dissociation first of the glucose (S_5) and then of the sodium (S_6) [16, 25]. The differen-

tial equations of the process are:

$$\frac{dC_1}{dt} = (k_{21}C_2 + k_{61}C_6) - (k_{12} + k_{16})C_1, \tag{2.57}$$
$$\frac{dC_2}{dt} = (k_{12}C_1 + k_{32}C_3 + k_{52}C_5) - (k_{21} + k_{23} + k_{25})C_2, \tag{2.58}$$
$$\frac{dC_3}{dt} = (k_{23}C_2 + k_{43}C_4) - (k_{32} + k_{34})C_3, \tag{2.59}$$
$$\frac{dC_4}{dt} = (k_{34}C_3 + k_{54}C_5) - (k_{45} + k_{43}C_4), \tag{2.60}$$
$$\frac{dC_5}{dt} = (k_{45}C_4 + k_{65}C_6 + k_{25}C_2) - (k_{54} + k_{52} + k_{56})C_5, \tag{2.61}$$
$$\frac{dC_6}{dt} = (k_{16}C_1 + k_{56}C_5) - (k_{61} + k_{65})C_6, \tag{2.62}$$

where the rate constant k_{12} depends on the Na^+ concentration outside the cell ($[Na]^2_{out}$), k_{65} depends on the Na^+ concentration inside the cell ($[Na]^2_{in}$). While the rate constant k_{23} depends on the glucose concentration outside the cell ($[G]_{out}$), and k_{54} depends on the glucose concentration inside the cell ($[G]_{in}$). As above, C_1 is the fraction of SGLT transporters $C_1 = N_1/N$ (N_1 number of transporters in state S_1 and N total number of transporters) The total concentration of carrier in the membrane is constant.

$$C_T = C_1 + C_2 + C_3 + C_4 + C_5 + C_6. \tag{2.63}$$

ACTIVE TRANSPORT

An example of an active transporter is the Ca^{2+}-ATPase pump located in the endoplasmic reticulum (ER) and sarcoplasmic reticulum (SR) of muscle. This transporter exploits chemical energy of the ATP to pump Ca^{2+} ions against their gradient. The abbreviation name of this pump is SERCA "Sarco-Endoplasmic Reticulum Ca^{2+} ATPase". Either SR and ER compartments have the function to store Ca^{2+} for different intracellular signaling cascade. The SERCA transporter pumps Ca^{2+} ions from the

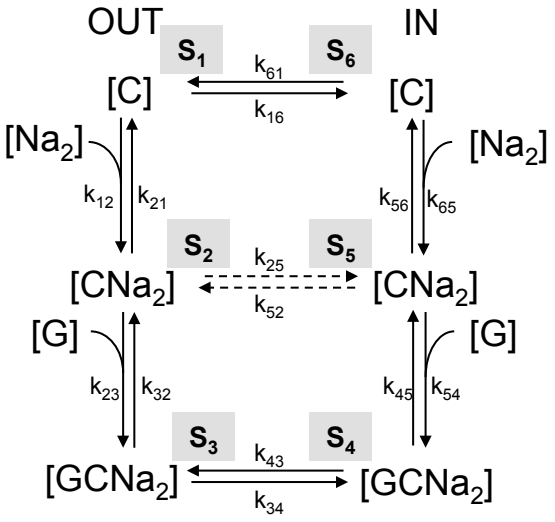

Figure 2.4.2: Six-state model of SGLT1 transporter.

cytoplasm into the SR and ER stores. Similarly, the Ca^{2+} pump PMCA, located in the plasma membrane, pumps Ca^{2+} out of the cell. There exists different isotypes of SERCA depending on the tissues, however their pumping rate is experimentally found to have a sigmoidal dependence on $[Ca^{2+}]_i$ with a Hill coefficient close to two [16]:

$$R = \frac{R_{max}[Ca^{2+}]_i^2}{K^2 + [Ca^{2+}]_i^2}. \tag{2.64}$$

In order to be consistent with the pump dependence on Ca^{2+} found experimentally, a two state simple model can be constructed: one state for activation and one state for inactivation. In particular, the rate expression in (2.63) can be obtained with the assumptions that the two states rapidly equilibrate and that only the active state transport Ca^{2+}. Rapid equilibrium leads to:

$$k^-/k^+ = k_{eq} = \frac{[Ca^2+]_i^2[I]}{[A]}, \tag{2.65}$$

where [I] and [A] are the per unit area concentrations of SERCA pumps in the two states, and the equilibrium constant K_{eq} is the ratio of the rate

constants. The active SERCAs can be obtained by using the conservation condition [I]+[A]=N and then solving for [A], getting:

$$[A] = \frac{N[Ca^{2+}]_i^2}{K^2 + [Ca^{2+}]_i^2}. \tag{2.66}$$

with $K = \sqrt{k_{eq}}$ in the units of concentration. A small value of K corresponds to a high affinity binding site, while a large value to a low affinity site. By assuming that the rate constant for the active state to transport Ca^{2+} is k, then we get:

$$R = k[A] = \frac{N[Ca^{2+}]_i^2}{K^2 + [Ca^{2+}]_i^2}, \tag{2.67}$$

with $R_{max} = kN$ [16].

2.5 Spatial Modeling

When cellular mechanisms are modeled, the general assumption is that chemical concentrations are uniform in space. This assumption is reasonable when the interest is the whole cell concentration dynamics. However, sometimes it is interesting to focus on some smaller region and to model the spatio-temporal dynamics of the non uniform concentrations. For instance, Ca^{2+} in the vicinity of Ca^{2+}-channels is high in a small region adjacent to the channel, creating the so-called domain Ca^{2+}. In order to understand the spatial nonuniformity, spatial modeling is exploited [16]. Let us consider a spatio-temporal variation along one dimension, x, of a chemical species C, $c(x,t)$, e.g along a thin tube with a constant section A. The total amount of C in an arbitrary interval $x_a < x < x_b$ can be obtained by [16]:

$$C(x_a, x_b) = \int_{x_a}^{x_b} c(x,t)Adx. \tag{2.68}$$

If c has units of μM, the total amount has units of μmol. By denoting $J(x,t)$ the rate of C across the interval boundaries x_a and x_b, with units amount/area/time, the flux of C into the interval is:

$$AJ(x_a,t) - AJ(x_b,t), \tag{2.69}$$

$J(x,t)$ is positive when C moves to the right and negative when C moves to the left. Furthermore, there could be either production or destruction of C within the interval. By denoting with $f(x,t,c)$, with units amount/time/volume, the net rate of production per unit volume at location x and time t, then the total amount of C produced in the interval at time t is:

$$\int_{x_a}^{x_b} f(x,t,c(x,t))Adx. \tag{2.70}$$

When f is positive the volume is a source, while when it is negative the volume acts as sink. The mathematical translation of the conservation law lead to the following formula:

$$\frac{d}{dt}\int_a^b c(x,t)dx = J(x_a,t) - J(x_b,t) + \int_{x_a}^{x_b} f(x,t,c(x,t))dx, \tag{2.71}$$

The flux terms can be rewrite as:

$$J(x_b,t) - J(x_a,t) = \int_{x_a}^{x_b} \frac{\partial}{\partial x} J(x,t)dx, \tag{2.72}$$

Therefore, all the terms in (2.72) can be written as integrals:

$$\frac{d}{dt}\int_{x_a}^{x_b} c(x,t)dx = \int_{x_a}^{x_b} \frac{\partial}{\partial x} J(x,t)dx + \int_{x_a}^{x_b} f(x,t,c(x,t))dx. \tag{2.73}$$

It can be rewritten as:

$$\int_{x_a}^{x_b} \left[\frac{d}{dt}c(x,t)dx - \frac{\partial}{\partial x}J(x,t)dx - f(x,t,c(x,t))\right]dx = 0. \tag{2.74}$$

The equality holds only if the integrand is zero, since the interval is arbitrary. Therefore, (2.74) can be replaced by the equivalent conservation

law in differential form:

$$\frac{\partial c}{\partial t} - \frac{\partial J}{\partial x} = f(x, t, c). \tag{2.75}$$

Since the equation contains partial derivatives with respect to two independent variables (x and t), it is referred to as a partial differential equations. In order to solve (2.75), we need an additional equation relating c and J. This secondary relation is usually called constitutive equation, specifically one such constitutive relation is called Fick's, which states that C moves from regions of high concentration to regions of low concentration at a rate proportional to the concentration gradient, that means:

$$J(x, t) = -D\frac{\partial}{\partial x}c(x, t), \tag{2.76}$$

where D is the diffusion constant and has units of length^2/time. (2.75) can be rewritten as:

$$\frac{\partial c}{\partial t} - D\frac{\partial^2}{\partial x^2}c(x, t) = f(x, t, c), \tag{2.77}$$

becoming a reaction-diffusion equation [16]. By generalizing Fick's law in the case of multiple dimensions, it becomes:

$$J(x, y, z, t) = -D\nabla c(x, y, z, t). \tag{2.78}$$

As above, it is possible to write the reaction-diffusion equation in the form:

$$\frac{\partial c}{\partial t} - D\nabla c(x, y, z, t) = f(x, y, z, t, c). \tag{2.79}$$

2.6 CalC Calcium Calculator

CalC ("Calcium Calculator" [**?**]) is a free (GNU copyleft) modeling tool for simulating intracellular calcium diffusion and buffering. CalC solves continuous reaction-diffusion PDEs describing the entry of calcium into a volume through point-like channels, and its diffusion, buffering and

binding to calcium receptors. The program allows the user to define different types of volumes as well as buffering specifications and simulation specifications. Some of the main simulation specifications are summarized hereafter.

GEOMETRY DEFINITIONS

It is possible to choose among various geometries of one, two, or three dimensions. One dimension geometries consisting of one dimension are cartesian 1D, disc and spherical; geometries consisting of two dimensions are cartesian 2D, cylindrical, polar and conical; finally, possible 3D geometries are cartesian 3D, spherical 3D and cylindrical 3D.

In the case of a spherically-symmetric geometry, which happens when the source is at the center of the sphere or when a current is uniformly distributed over the surface, the 3D problem reduces to a 1D problem in spherical coordinates. The volume can be defined by two variables, R_0 and R_1 which stand for the inner and outer radii respectively of the spherical shell that serves as the diffusion space. As a consequence, only two boundary conditions need to be defined, one for the inner and one for the outer faces of the shell.

With regard to cylindrical geometry, if the problem is symmetric, the 3D problem reduces to a 2D problem. The volume can be defined only by the inner and outer radii of the volume, R_0 and R_1, and the limiting z-values, Z_0 and Z_1. At the same way, only four boundary conditions need to be defined.

In the conical geometry, the 3D problem reduces to a 2D problem when the problem is symmetric in spherical coordinates. The volume is defined only by the inner and outer radii of the volume, R_0 and R_1, and the limiting angle values, θ_0 and θ_1. Only four boundary conditions need to be defined. Moreover, a composed geometry can be realized using an arbitrary number of boxes, consisting of spheres, cylinders etc, with an arbitrary number of obstacles.

GRID SPECIFICATION

The entire diffusion space is divided into a mesh of points, "grid", and for each point calcium and buffer concentrations are computed. It is also possible to build a grid that is non-uniform so that the accuracy can be improved in the vicinity of the calcium channel(s) by increasing the density of the grid points. However, using a non uniform grid leads to a systematic computational error.

BOUNDARY CONDITIONS

The default boundary condition specification for buffers and calcium is zero flux (reflective) at all surfaces of all geometry elements. Nevertheless, the user is allowed to set the boundary condition by choosing between three boundary condition forms:

$$AFlux + B([Ca] - [Ca]_0) + C(\frac{[Ca]^n}{[Ca]^n + K^n} - \frac{[Ca]_0^n}{[Ca]_0^n + K^n}) = 0, \quad (2.80)$$

$$AFlux + B([Ca] - [Ca]_0) = 0, \quad (2.81)$$

$$[Ca] - [Ca]_0 = R, \quad (2.82)$$

where $[Ca]$ is the Ca^{2+} concentration at the boundary, $[Ca]_0$ is the background concentration. $Flux$ is the flux per unit area at the boundary, with unit in 3D of μM μm/ms, the unit of B is μm/ms, and unit of C is the same as unit of flux. Default unit of pump affinity K is μM.

BUFFER DEFINITIONS

The program permits to define an arbitrary number of buffers with one-to-one Ca^{2+} binding stoichiometry. The buffer characteristics is defined by its total concentration, and the binding kinetic parameters (affinity,

binding rate and unbinding rate). The buffer can be either fixed or mobile, and for a mobile buffer the total concentration is assumed to be homogeneous throughout the diffusion space.

In order to generate a buffer with 1-to-2 calcium binding stoichiometry, the following calcium binding reaction can be implemented by defining the rates of the two reactions as properties of the buffer B for the first reaction and CaB for the second reaction:

$$B + 2Ca^{2+} \leftrightarrow CaB + Ca^{2+} \leftrightarrow Ca_2B. \tag{2.83}$$

The diffusion coefficient of cooperative buffers is allowed to change upon Ca^{2+} binding, therefore the user has to define three diffusion coefficients, one for B one for CaB and one for Ca_2B. if the user defines the total concentration only for the unbound buffer then the fully and partially bound states of the buffer are assumed to be in equilibrium with the background Ca^{2+}. Otherwise the total concentration of all buffers can be given.

CALCIUM CHANNELS

The user can defined an arbitrary number of channels and for each channel its position and width have to be specified. The default value for the width parameters is zero, which corresponds to a point-like source. Channels can be located anywhere either inside the volume or at the boundary.

SIMULATION SPECIFICATIONS

During the run of a simulation the integration time and the value of the calcium channel current have to be specified. Simulation can be performed with a variable time step (adaptive) or with a fixed time-step (non adaptive). The aim of the adaptive time step is to maintain a given level of accuracy, and this can be obtained by changing the size of integration time step. Briefly, each time step is increased by multiplicative factor, slightly grater than 1. Accuracy checks are performed every n steps, and

if it is successful, n is increased by 1, otherwise the time step is halved and n is reset depending on the number of steps since last time step reduction. If the error is greater than five times the accuracy tolerance the integrator takes a reverse step back to the previous successful accuracy check. In the case of a fixed time step instead a fixed time step is defined. In addiction to the run method selected, current though the channel(s) has to be defined, too.

A simulation can be defined as a set of shorter simulations and for each of them a current definition should be declared. This simulation method is recommended in presence of suddenly current changes, i.g simulation of channel opening and closing events.

3

Calcium Oscillations Disturbed by Reactive Oxygen and Nitrogen Species in Min6 β-cells

As explained in the Introduction, insulin is secreted from the pancreatic β-cells in distinct pulses [26, 27] and disturbed pulsatile insulin release has been suggested to be an early marker of diabetes [28]. These bursts of insulin are driven by underlying oscillations in electrical activity and cytosolic Ca^{2+} levels, which periodically trigger Ca^{2+}-regulated exocytosis [29]. Importantly, secretory pulses are more effective than constant insulin levels in lowering plasma glucose levels [28, 30, 31]. In particular, hepatic signaling is highly sensitive to whether insulin is released in pulses [32], leading to the suggestion that insulin resistance in the liver is secondary to disturbed pulsatile insulin release [33]. Thus, a deeper understanding of oscillatory β-cell activity and its disturbance has clinical

relevance.

Disturbed insulin secretion and diabetes have been associated with β-cell damage caused by reactive oxygen species (ROS)[34]. ROS are defined as molecules or ions formed by incomplete one-electron reduction of oxygen. The term ROS includes both a set of free radicals such as superoxide, hydroxyl radical, singlet oxygen and a set of non-radical species such as hydrogen peroxide [35]. The major source of ROS in the cell is mitochondria. During the mitochondrial oxidative phosphrylation, which is the main ATP synthetic pathway, the electron transport chain generates different ROS [36]. It is well established that ROS can demage cellular components [36]. However, ROS have also been shown to exert a stimulating short-term effect on insulin release [36]. Hence, ROS may act as a double-edged sword: moderate and short-term elevations play a positive signaling role augmenting insulin secretion, but prolonged exposure to elevated ROS levels, characteristic of oxidative stress, are detrimental for the β-cells [34, 37]. Similarly, reactive nitrogen species (RNS), such as nitric oxide (NO), have been shown to elevate Ca^{2+} levels and stimulate insulin secretion at low concentrations, whereas high NO concentrations exert an inhibitory effect on β-cell function and survival [38].

ROS/RNS target various cellular mechanisms underlying insulin secretion [34], and in particular components involved in Ca^{2+} handling [35, 39]. For example ROS/RNS activate voltage-gated Ca^{2+} channels and endoplasmic reticulum (ER) release channels, such as the inositol triphospate receptors (IP3Rs) and ryanodine receptors (RyRs). In addition, sarcoplasmic/endoplasmic reticulum Ca^{2+} ATPases (SERCAs) and plasma membrane Ca^{2+} ATPases (PMCAs) are inhibited by ROS/RNS. All these effects contribute to elevating the cytosolic Ca^{2+} concentration, which may trigger cell dysfunction [40]. Moreover, ROS/RNS effects on ER Ca^{2+} handling could lead to ER stress and consequent protein misfolding [41]. In addition, and of particular interest for this Chapter, ROS/RNS effects on the Ca^{2+} handling machinery might disturb Ca^{2+} oscillations and downstream pulsatile insulin release.

Induced ROS production inside the cell can be obtained by the sub-

stance aluminum phthalocyanine chloride (AlClPc) which is a photosensitizer commonly used in photodynamic therapy experiments and clinical protocols; photoactivation of AlClPc induces chemical changes into neighbouring molecules, which lead to ROS production [42], as well as NO/RNS release [43–45]. In this Chapter it will be shown that ROS/RNS production by AlClPc photoactivation accelerates or abolishes Ca^{2+} oscillations in the widely used insulin-secreting MIN6 β-cell line. To guide the interpretation of our experimental results, a mathematical model of Ca^{2+} handling will be adapted to MIN6 cells. The model will be useful to support experimental results.

3.1 Experiments and Mathematical Modeling

3.1.1 Experiments

MIN6 β-cells ([46]; passages 19-40; a gift from Prof. L. Eliasson, LUDC, Malm$\ddot{o}$, Sweden) were grown in Dulbecco's modified Eagle's medium (DMEM) High glucose (4 g/L - 23 mM) and L-glutamine (0.58 g/L - 4 mM), supplemented with 15% heat-inactivated Fetal Bovine Serum (FBS), 75 mg/L penicillin, 50 mg/L streptomycin and maintained in a humidified incubator with 95% air and 5% CO_2 at 37° C. Medium was changed every 2-3 days and cells were passed every 5-7 days when they were $\sim$60% confluent [46, 47].

Culture media, compounds and chemicals were all from Sigma Aldrich, except Fura-2 AM (Life Technologies, F-1221), MitoSOX (Life Technologies, M36008) and CuFl (see below). Experiments were conducted at room temperature under constant flow perfusion with extracellular medium (ECM) at pH 7.4 (adjusted with NaOH). The ECM was composed of (in mM): 150 NaCl, 5 KCl, 1 MgCl, 10 Hepes, 2 NaPyr, 2 CaCl2, and either 3 or 25 d-Glucose. In most experiments 15 mM Tetra Ethyl Ammonium (TEA, a K^+ channel blocker) Chloride was added to the ECM containing 25 mM d-Glucose. Where indicated, SERCA pumps were inhibited by the addition of 200 nM Thapsigargin.

Intracellular free Ca^{2+} concentration was tracked by fluorescence imaging using Fura-2 acetoxymethyl (AM) ester. MIN6 pseudoislets were placed on poly-L-lysine (0.1% for 2 hours) treated coverslips and incubated at 37°C in DMEM High Glucose (D5796) for a total time of 20 minutes with 5 μM Fura-2 AM, Pluronic F-127 (0.01% w/v) and Sulfinpyrazione (250 μM). Pluronic (P2443) and Sulfinpyrazone (S9509) were used to prevent the complexation and secretion of dye. ROS production was obtained by photoactivation at 660 nm of AlClPc (363530). MIN6 pseudoislets were incubated at 37°C in DMEM High Glucose for a total time of 1 hour with 10 μM AlClPc.

NO was monitored by fluorescence imaging using CuFL. The probe was prepared using the Nitric Oxide Sensor (Intracellular) Kit (Strem Chemicals, part No. 96-0293) by reacting the fluorescein-based ligand 2-2-Chloro-6-hydroxy-5-[2-methylquinolin-8-ylamino)methyl]-3-oxo-3H -xanthen-9-ylbenzoic acid (FL) with $CuCL_2$ in a 1:1 ratio in buffered aqueous solution. MIN6 pseudoislets were incubated in ECM solution for a total time of 15 minutes at room temperature with 20 μM CuFl and then washed for 15 minutes with ECM solution [48]. ROS signalling was monitored with fluorescence imaging using MitoSOX. MIN6 pseudoislets were incubated at 37°C in DMEM High glucose (D5796) without FBS for a total time of 15 minutes with 2.5 μM MitoSOX.

In experiments with Fura-2, specimens were excited alternately by 365 nm and 385 nm high power LEDs (Thorlabs, M365L2 - M385L2). In experiments with CuFl [48], specimens were excited with 460 nm high efficacy 5W Dental Blue LED (Led Engine, LZ1-00DB00). In experiments with MitoSOX, specimens were excited with 530 nm high power LED (Thorlabs, M530L3). Phthalocyanine was photoactivated by 660 nm high power LED (Thorlabs, M660L3) filtered through a pair of polarizers to modulate the LED intensity. The fluorescence emission was selected by an emission filter (HQ 520/40, Chroma, Rockingham, VT) and the emitted fluorescence images were collected by a complementary metal-oxide semiconductor (CMOS) cooled camera (Pco.Edge) using a water immersion objective (40×, Lumplan FL, N.A.= 0.80; Olympus). To generate each

frame, the 365 nm and 385 nm LEDs were activated in rapid sequence for 200 ms each and a fura-2 ratio image was generated every second. The 460 nm LED was activated for 100 ms and a CuFL intensity image was generated every second. The 530 nm LED was activated for 200 ms and a MitoSOX intensity image was generated every second. For pulsed-light experiments, the 660 nm LED was activated for 100 ms/pulse and 1 pulse/second.

Images were analyzed with software developed in the Mammano laboratory using the Matlab platform (Release 14, MathWorks, Inc., Natick, MA, USA). Ca^{2+} signals were measured as fura-2 emission ratio changes, $\Delta R = R(t) - R(0)$, where t is time, $R(t)$ is fura-2 emission intensity excited at 365 nm divided by the intensity excited at 385 nm, and $R(0)$ indicates pre-stimulus ratio.

Fura-2, CuFL and MitoSOX traces were generated by averaging pixel signals within regions of interest (ROIs) corresponding to individual cells. Traces were analyzed using an ad-hoc developed Matlab function that identifies local maxima. Function parameters were adjusted in order to discard noise fluctuations and retain only true Ca^{2+} oscillation peaks. The temporal occurrence of the peaks was used to calculate the time interval between two consecutive peaks (period). For each cell (ROI), peak period and amplitude values were averaged to obtain a single-cell value. Statistical comparisons were done with unpaired t tests for samples with unequal variance.

3.1.2 Mathematical Model

A mathematical model of oscillatory behavior in β-cells [49], which reproduces many observed patterns in mouse β-cells is build on and adapted to MIN6 cells. The model is used to investigate the effects of TEA and modifications in ER Ca^{2+} handling on Ca^{2+} oscillations.

The model includes four voltage gated currents: a Ca^{2+} current (I_{Ca}), a delayed rectifier K^+ current (I_K), a Ca^{2+}-dependent K^+ current ($I_{K(Ca)}$), and an ATP-sensitive K^+ current ($I_{K(ATP)}$). The membrane potential V

develops in time according to:

$$\frac{dV}{dt} = -\frac{I_{Ca} + I_K + I_{K(Ca)} + I_{K(ATP)}}{C_m}, \tag{3.1}$$

where C_m is the membrane capacitance. The currents are modeled as in [49]:

$$I_{Ca} = g_{Ca} m_\infty(V)(V - V_{Ca}), \tag{3.2}$$
$$I_K = g_K n(V - V_{Ca}), \tag{3.3}$$
$$I_K(Ca) = g_{K(Ca)} \omega(V - V_K), \tag{3.4}$$
$$I_{K(ATP)} = g_{K(ATP)} a(V - V_K), \tag{3.5}$$

where the delayed rectifier activation, n, and ATP oscillations, a, are given by:

$$\frac{dn}{dt} = \frac{n_\infty(V) - n}{\tau_n}, \tag{3.6}$$
$$\frac{da}{dt} = \frac{a_\infty(c) - a}{\tau_a}. \tag{3.7}$$

The ratio ADP/ATP is allowed to vary (3.7) according to evidence of ATP oscillations in MIN6 cells [49]. The equilibrium functions are described with Boltzmann functions:

$$m_\infty(V) = \frac{1}{1 + e^{\frac{v_m - V}{s_m}}}, \tag{3.8}$$
$$n_\infty(V) = \frac{1}{1 + e^{\frac{v_n - V}{s_n}}}, \tag{3.9}$$
$$a_\infty(V) = \frac{1}{1 + e^{\frac{r - c}{s_a}}}. \tag{3.10}$$

The variable ω is the fraction of K(Ca)-channels activated by cytosolic Ca^{2+}:

$$\omega = \frac{c^5}{c^5 + K_D^5}, \tag{3.11}$$

where K_D is the Ca^{2+} level giving half-maximal activation of K(Ca) cur-

rent. The model also includes Ca^{2+} dynamics in the cytosol and in the ER of MIN6 cells as described by:

$$\frac{dc}{dt} = f_{cyt}(J_{mem} + J_{ER}), \tag{3.12}$$

$$\frac{dc_{ER}}{dt} = f_{ER}(V_{cyt}/V_{ER})J_{ER}. \tag{3.13}$$

Here, J_{mem} is the Ca^{2+} flux through the plasma membrane, f_{cyt} is the fraction of free total Ca^{2+}, and f_{ER} is the fraction of free Ca^{2+} in the ER. J_{ER} is the total efflux from ER. J_{SERCA} is the influx into the ER, via SERCA pumps. These fluxes are given by:

$$J_{mem} = -(\alpha I_{Ca} + k_{PMCA}c), \tag{3.14}$$

$$J_{ER} = J_{leak} - J_{SERCA}, \tag{3.15}$$

$$J_{SERCA} = k_{SERCA}c, \tag{3.16}$$

$$J_{leak} = p_{ER}(c_{ER} - c), \tag{3.17}$$

where α converts units of current to unit of flux, k_{PMCA} and k_{SERCA} are the rate constants for the plasma membrane Ca^{2+} ATPase pump (PMCA) and the ER membrane Ca^{2+} ATPase pump (SERCA), respectively. The ER Ca^{2+} release rate p_{ER} can be either constant, or an increasing function of cytosolic Ca^{2+} to simulate calcium-induced calcium release (CICR), which is operating in MIN6 cells [50]:

$$p_{ER} = p_{min} + \frac{p_{max} - p_{min}}{1 + (\frac{K_{CICR}}{c})^2}, \tag{3.18}$$

where the parameter K_{cicr} determines the amount of calcium-induced calcium released (CICR), which is absent for $K_{cicr} = 0$ μM. All parameters are given in Table 3.1.1.

The main mechanism resulting in oscillatory behavior in the model is negative feedback of Ca^{2+} onto the ATP concentration, for example because of increased ATP consumption by Ca^{2+} pumps. Lower ATP levels

lead to K(ATP)-channel opening and, eventually, to cessation of electrical activity and Ca^{2+} influx. Calcium is then removed from the cytosol, allowing ATP levels to rise, resulting in reduced K(ATP)-current, reappearance of electrical activity and increasing cytosolic Ca^{2+} levels due to Ca^{2+} influx.

3.2 Experimental and Simulation Results

Tetraethylammoniumv(TEA)and glucose in min6 cells

The MIN6 beta-cell line [46] is widely used to investigate mechanisms underlying insulin secretion due to its good glucose responsiveness and relatively easy experimental handling [46, 47, 51, 52]. It is well known that MIN6 cells exhibit irregular, small-amplitude Ca^{2+} oscillations when exposed to glucose, and that the addition of the K^+ channel antagonist tetraethylammonium (TEA) changes these fluctuations into large-amplitude and more regular oscillations as shown in Fig. 3.2.1A) and in [47, 51]. The period of the induced oscillations was typically 20-30 seconds, similar to published results for MIN6 cells [46, 47, 51] and so-called fast Ca^{2+} oscillations observed in mouse islets [53, 54].

To obtain insight into this behavior, we use the mathematical model of oscillatory behavior in β-cells. We assume that, compared to pancreatic β-cells in islets of Langerhans, MIN6 cells have larger K^+ currents [51], which prevent large-amplitude oscillations. Our model suggests that this mechanism is plausible. Small-amplitude, high-frequency fluctuations were transformed into slower large-amplitude oscillations when the conductance of the K_v current was reduced by 80% (Fig. 3.2.1B); see also [51]).

Parameter	Value	Unit
g_{Ca}	1200	pS
V_{Ca}	25	mV
v_m	-20	mV
s_m	12	mV
g_K	8000	pS
V_K	-75	mV
v_n	-16	mV
s_n	5	mV
τ_n	16	ms
$g_{K(Ca)}$	100	pS
k_D	0.3	μM
$g_{K(ATP)}$	500	pS
r	0.14	μM
s_a	0.1	μM
τ_a	50000	ms
α	4.5×10^{-6}	fA^{-1} μM ms^{-1}
f_{cyt}	0.01	adim
f_{ER}	0.01	adim
k_{PMCA}	0.2	ms^{-1}
k_{SERCA}	0.4	ms^{-1}
V_{cyt}/V_{ER}	5	ms^{-1}
p_{min}	5×10^{-4}	ms^{-1}
p_{min}	5×10^{-3}	ms^{-1}
K_{cicr}	0	μM
C_m	5300	fF

Table 3.1.1: Default parameter values of the mathematical model used to simulate MIN6 cells in the presence of 25 mM glucose and 15 mM TEA.

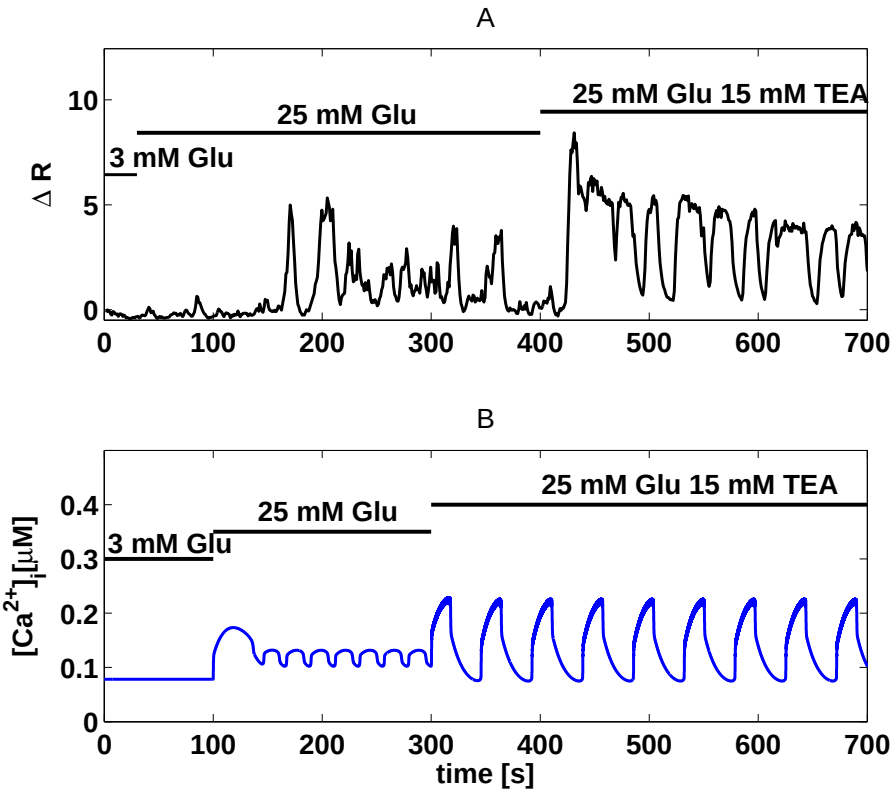

Figure 3.2.1: The K^+ channel antagonist TEA induces large amplitude Ca^{2+} oscillations. A) Recording of Fura-2 fluorescence reporting Ca^{2+} concentrations in a MIN6 cell stimulated by glucose and TEA, as indicated. B) Model simulation of the experiment in panel A). The increase in glucose from 3 mM to 25 mM was simulated by lowering $g_{K(ATP)}$ to 500 pS from 650 pS; TEA application was simulated by decreasing the K(V) conductance ($g_{K(V)}$) by $\sim 80\%$, from 41 nS to 8 nS.

ROS/RNS PRODUCTION AND OSCILLATORY Ca^{2+} DYNAMICS

To investigate the short-term effects of ROS/RNS on oscillatory Ca^{2+} dynamics in MIN6 cells, the cells were loaded with AlClPc. When photoexcited at 660 nm, AlClPc produces ROS in amounts depending on the intensity of the LED illumination as revealed by the ROS sensor MitoSOX (Fig. 3.2.2A). LED illumination *per se*, i.e., in the absence of AlClPc, does not produce ROS, nor results in any artifactual MitoSOX signal (Fig.3.2.2A). Control experiments with HyPer, another ROS sensor, confirm these results (Fig.3.2.2C). In addition, AlClPc photoactivation increases NO levels [45], as reported by the selective fluorescent probe CuFL [45](Fig. 3.2.2B; see also [43]). We find that ROS/RNS production by photoactivation of AlClPc at maximal (100%) LED intensity abolishes Ca^{2+} oscillations in MIN6 cells. The Ca^{2+} concentration shows a peak and then settles at an intermediate level (Fig. 3.2.3A). When SERCA pumps are inhibited by thapsigargin (Tg) to prevent ER Ca^{2+} filling (Fig. 3.2.3B), the Ca^{2+} peak is substantially reduced. Indeed, the mean ratio of peak to oscillation amplitude in the control case, ctrl, is: 0.98 ± 0.04 (n=38),while with Tg: 0.19 ± 0.02 (n=62), $p < 0.001$, Fig. 3.2.3D). Control experiments in the absence of AlClPc show that maximal LED illumination does not *per se* influence the Ca^{2+} oscillations (Fig. 3.2.3C). These observations suggest that the surge of cytosolic Ca^{2+} in response to ROS/RNS production is caused primarily by release of Ca^{2+} from the ER. Indeed, ROS/RNS are known to inhibit SERCA pumps and activate RyRs and IP3Rs [35, 39].

EFFECT OF MODERATE LEVEL OF ROS/RNS

Having established that massive ROS/RNS production by AlClPc photoactivation abolishes Ca^{2+} oscillations in MIN6 cells, we turn our atten-

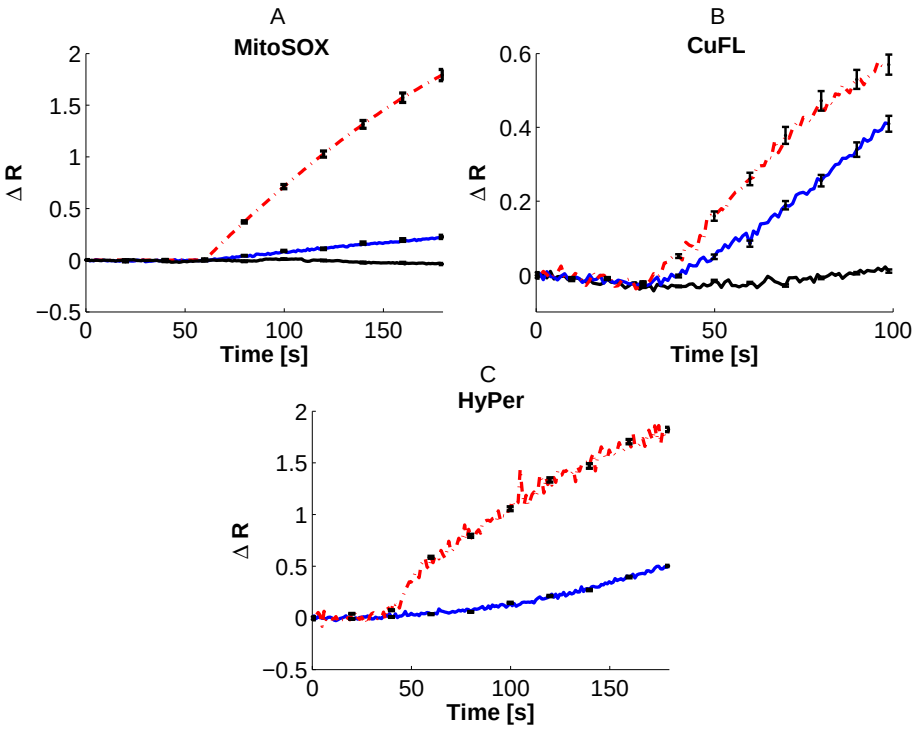

Figure 3.2.2: A) ROS production by AlClPc photoactivation measured with the superoxide sensor MitoSOX (illumination from t=60 s). The LED intensity is 100% (red curve) or 10% (blue curve). The full, black curve shows the ROS response to 100% LED illumination in the absence of AlClPc. B) NO levels monitored with the sensor CuFL (illumination from t=30 s) at 30%(full, black), 70%(blue) or 100% (red) LED intensity. C) ROS production by AlClPc photoactivation measured with the superoxide sensor Hyper (illumination from t=30 s). The LED intensity is 100% (red curve) or 10% (blue curve).

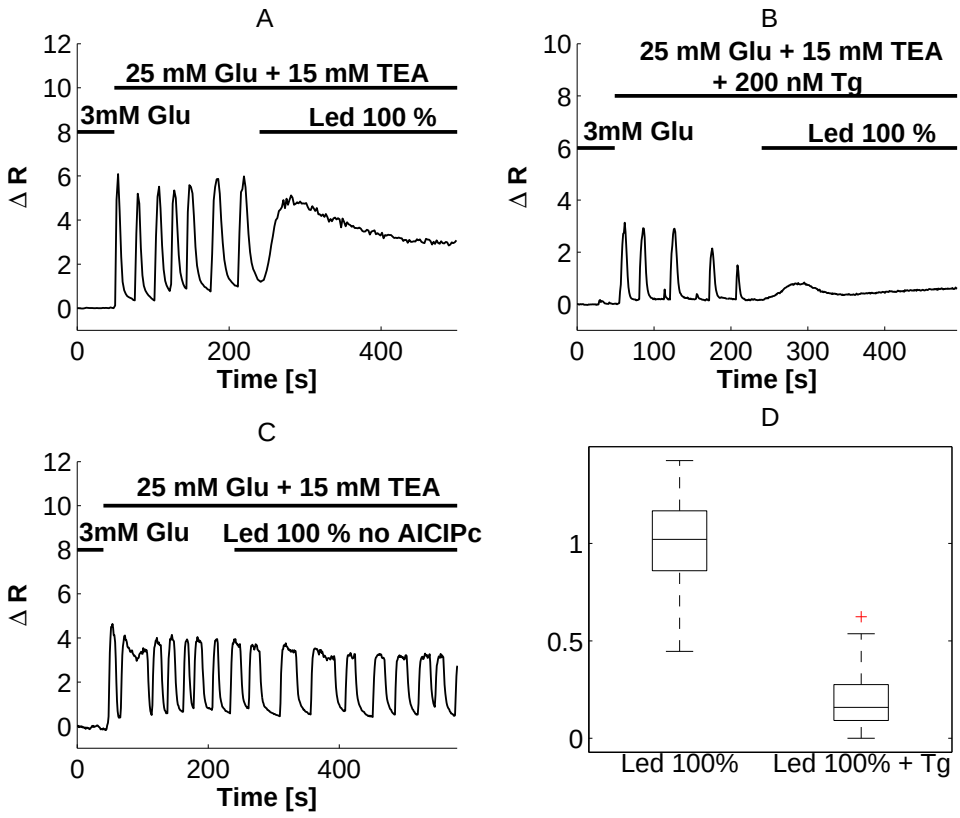

Figure 3.2.3: A) Photoactivation of AlClPc with 100% LED intensity abolishes Ca^{2+} oscillations and results in a peak of Ca^{2+} concentration. B) In the presence of 200 nM Tg, the Ca^{2+} peak in response to 100% LED photoactivation is reduced. C) In the absence of AlClPc, 100% LED illumination did not interfere with Ca^{2+} oscillations (representative of 37 cells in 4 experiments). D) Summary of the Fura-2 (Ca^{2+}) peak normalized to oscillation amplitude in cells in the absence (ctrl, n=38) and presence of Tg (n=62).

tion to the effects of moderate ROS/RNS levels. When photoactivating AlClPc with 10% LED intensity we observe that Ca^{2+} oscillations typically persist, but with a modified profile.

Under control conditions, a step from 3 mM glucose to 25 mM glucose plus 15 mM TEA elicites a biphasic response consisting of a 1^{st} phase lasting ∼4-5 minutes with rapid oscillations followed by a 2^{nd} phase typically with slower oscillations (Fig. 3.2.4A). In contrast, the oscillations typically do not slow down when the second phase is perturbed by application of Tg (Fig. 3.2.4B) or photoactivation of AlClPc at 10% LED intensity (Fig. 3.2.4C) at t=240 seconds. Compared to control conditions, Tg or AlClPc photoactivation at 10% LED intensity results in a heterogeneous population of Ca^{2+} amplitude responses, which in some cells decrease substantially but in other show behavior similar to the control patterns. This heterogeneity is observed when studying cells in different experiments (Fig. 3.2.4B) as well as for synchronized cells in the same experiment (Fig. 3.2.4C).

To handle cell heterogeneity, we normalize the single-cell 2^{nd} phase oscillations period and amplitude to the 1^{st} phase period and amplitude, respectively, of the same cell. This analysis reveals that the 2^{nd} phase period increases by ∼70% (ratio of 2^{nd} to 1^{st} phase periods 1.69±0.14) under control conditions (Fig. 3.2.4D). In contrast, the period is unchanged when Tg or 10% LED photoactivation of AlClPc are present during the second phase (ratio of periods: 0.93±0.05 and 0.99±0.12, respectively; in both cases $p<0.001$ vs. Control; p=0.22 Tg vs. 10% LED; Fig 3.2.4D). The amplitude of the Fura-2 ratio signal is lower in the 2^{nd} than in the 1^{st} phase under control conditions (ratio of amplitudes 0.76±0.12). The reduction in 2^{nd} phase amplitude is greater in the presence of Tg or with 10% LED AlClPc photoactivation (ratio of amplitudes: 0.5±0.02 and 0.49±0.03, respectively; in both cases $p<0.001$ vs. control; p=0.20 Tg vs. 10% LED; Fig. 3.2.4E). However, there is substantial cell-to-cell heterogeneity in the response to both Tg and to 10% LED AlClPc photoactivation, in particular with respect to the relative amplitude, which in many cases does not decrease more than in the control case (Fig.3.2.4B,C,E). Nonetheless, the fact

that Tg and 10% LED AlClPc photoactivation accelerate the Ca^{2+} oscillations and reduce their amplitude to a similar degree, suggest that their mechanism of action might be shared, i.e., inhibiting SERCA pumping, a well-known target of ROS/RNS [35, 39], and in accordance with our findings using 100% LED activation (Fig.3.2.3).

MATHEMATICAL MODEL INTERPRETATION

Altogether, the results described above indicate that ROS/RNS production by AlClPc and SERCA inhibition by Tg accelerate Ca^{2+} oscillations to a similar degree (Fig.3.2.4). Moreover, the presence of Tg results in a reduction in the Ca^{2+} peak seen in response to high ROS/RNS levels (Fig. 3.2.3). These observations suggest that ROS/RNS modify Ca^{2+} oscillations via a reduction of ER Ca^{2+} levels. To test whether this interpretation is compatible with known β-cell Ca^{2+} handling mechanisms, we perform simulations with the model used to obtain insight into TEA-induced large-amplitude oscillations (Fig. 3.2.1). Consistent with our working hypothesis, the oscillatory behavior of the mathematical model accelerates when SERCA activity is lowered (Fig. 3.2.5A; see also [49]). Similarly, increasing Ca^{2+} release from the ER in the model (mimicking ROS/RNS activation of e.g. RyRs and IP3Rs; [35, 39]) increases the frequency of the Ca^{2+} oscillations (Fig. 3.2.5B). However, the simulated amplitude is nearly unchanged by the presence of Tg or increases Ca^{2+} release. We note that some MIN6 cells show amplitude responses to Tg or 10% LED AlClPc photoactivation that are similar to the control case (Fig. 3.2.4). Hence, these model simulations are more similar to this subgroup of MIN6 cells with respect to the effect on oscillation amplitude.

Of interest, the simulated modifications of ER Ca^{2+} handling are insufficient to abolish Ca^{2+} oscillations in the model. This result suggests that high levels of ROS/RNS, as produced by 100% LED AlClPc photoactivation (Fig. 3.2.3), also act on other components involved in the generation of rhythmic Ca^{2+} concentrations. For example, ROS/RNS are known to inhibit not only SERCA pumps, but also plasma membrane

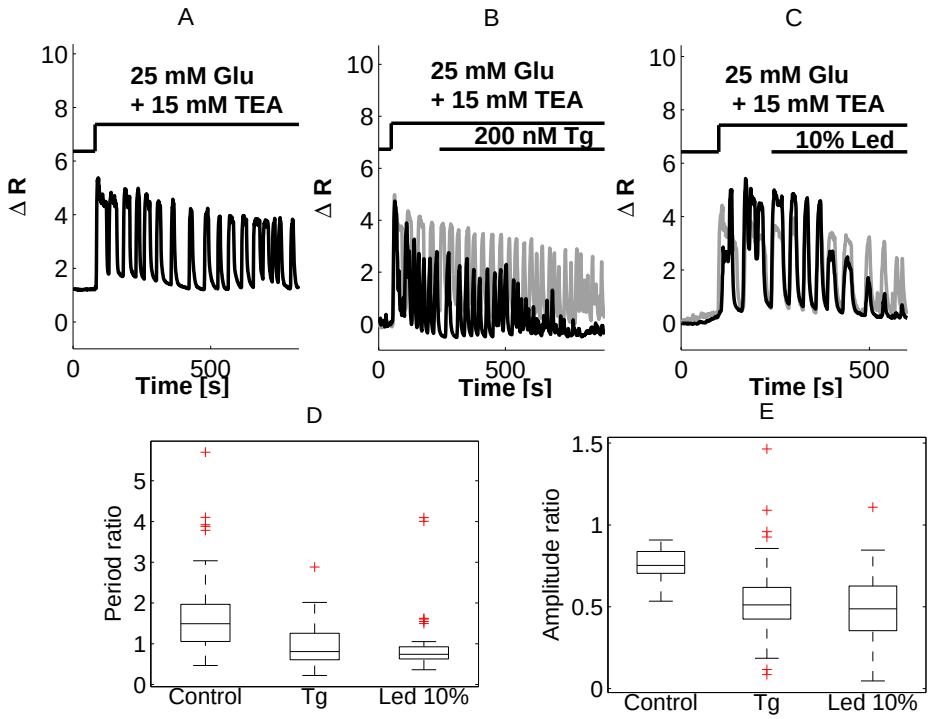

Figure 3.2.4: A) Example of Ca^{2+} trace in a MIN6 cell stimulated with 25 mM glucose and 15 mM TEA. B) SERCA inhibition by Tg accelerates Ca^{2+} oscillations, and often reduces their amplitude (black trace). Two cells from two independent experiments with different amplitude responses are shown. C) Moderate ROS/RNS production by 10% LED photoactivation of AlCIPc result in modifications in Ca^{2+} oscillations similar to Tg application. Two synchronized cell from a single experiments with different amplitude responses are shown. D) Summary of 2^{nd} phase (after 240 sec) Ca^{2+} oscillation periods normalized to 1st phase (before 240 sec) periods in control conditions (n=50), or in the presence of Tg (n=102) or moderate ROS/RNS levels (n=50) during the 2^{nd} phase. e) Summary of 2nd phase (after 240 sec) Ca^{2+} oscillation Fura-2 amplitudes normalized to 1^{st} phase (before 240 sec) amplitudes in control conditions (n=50), or in the presence of Tg (n=102) or moderate ROS/RNS levels (n=50) during the 2^{nd} phase.

Ca^{2+} ATPases (PMCAs) [35, 39]. Our simulations confirm that a reduction in the PMCA rate, together with reduced SERCA activity and increased ER Ca^{2+} leak, could abolish Ca^{2+} oscillations (Fig. 3.2.5C). In agreement with experiments (Fig. 3.2.3), the presence of Tg before increasing ROS/RNS levels reduces the Ca^{2+} peak in our simulations (Fig. 3.2.4D). Thus, the model suggests that moderate ROS/RNS levels mainly act on ER Ca^{2+} handling, while high ROS/RNS concentrations might also inhibit PMCAs and thus abolish Ca^{2+} oscillations.

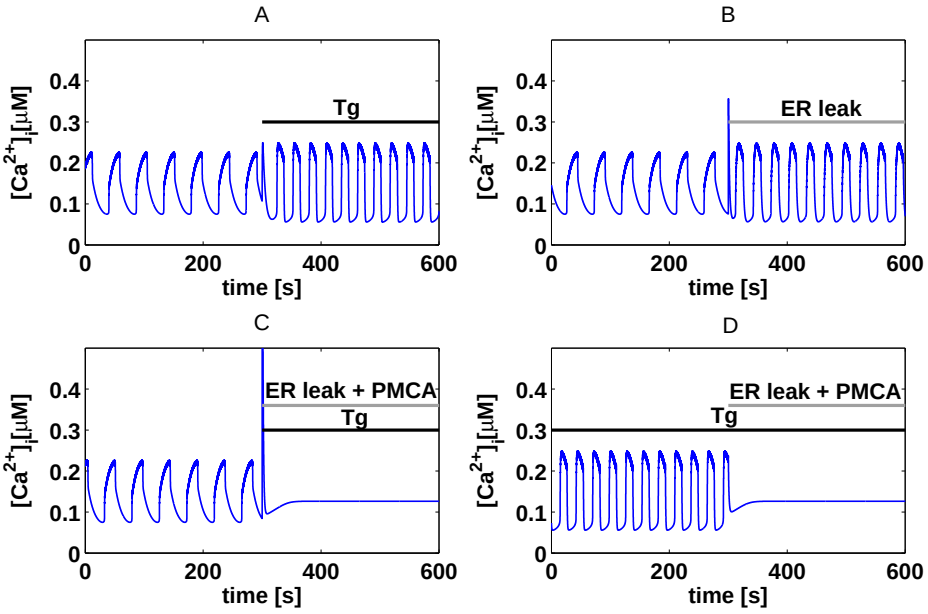

Figure 3.2.5: A) Model simulation showing acceleration of Ca^{2+} oscillations in response to Tg (k_{SERCA}=0 ms^{-1} as indicated by the bar "T"). B) As in panel A) but with increased ER Ca^{2+} release (p_{leak} multiplied by a factor 10, indicated by the bar). C) Simulation of the combined effect of inhibition of PMCAs (k_{PMCA} lowered from 0.20 to 0.12 ms^{-1}), Tg application (as in panel A) and increased ER leak (as in panel B), which abolish Ca^{2+} oscillations as seen experimentally (Fig. 3.2.3). D) As in panel C), but with Tg present throughout as in Fig. 3.2.3, which removes the Ca^{2+} peak when ER leak and PMCA inhibition is simulated.

3.3 DISCUSSION

It has been proposed that reactive oxygen species (ROS) act as a double-edged sword in β-cells [37]. Similarly, reactive nitrogen species (RNS) have beneficial or detrimental effects on β-cell function depending on their levels [38]. In agreement with this tenet we show here that massive ROS/RNS production by photoactivation of AlClPc at maximal (100%) LED intensity abolished Ca^{2+} oscillations in MIN6 β-cells (Fig. 3.2.3), while moderate ROS/RNS production (10% LED) accelerated the periodic Ca^{2+} excursions (Fig. 3.2.4). Since regular Ca^{2+} oscillations are a hallmark of healthy β-cell function [29], our results suggest that massive ROS/RNS production lead to immediate β-cell dysfunction, whereas moderate ROS/RNS levels might have a slightly positive effect on the Ca^{2+} behavior since oscillations are more frequent. An interesting possibility is that dynamic control of ROS/RNS levels contributes to shaping physiological Ca^{2+} oscillations in β-cells.

Based on our experimental results, we conclude that moderate ROS/RNS levels influence Ca^{2+} oscillations via inhibition of SERCA pumps and/or by increasing activity of ER release channels (IP3Rs/RyRs), all known targets of ROS/RNS [35, 39]. The molecular mechanisms involved in ROS/RNS action include amino acid redox modifications; the typical targets are thiol groups of cysteine residues, albeit other amino acids such as arginine, lysine and methionine residues can also react with ROS/RNS [35, 39]. Current hypotheses about the inactivation of PMCAs by ROS/RNS propose an alteration of PMCA Tyr589, Met622 and Met831 residues [39]. SERCA activity has been shown to be inhibited by ROS/RNS modification of cysteine (and tyrosine) residues [39].

Model simulations support this conclusion. In addition, the model suggests that high amounts of ROS/RNS also act on Ca^{2+} handling components at the plasma membrane, e.g. by inhibiting PMCAs, another ROS/RNS target [35, 39], which abolishes Ca^{2+} oscillations. Interestingly, it has been reported that SERCA is more sensitive to ROS than PMCA [55], in line with our findings.

The limited knowledge of MIN6 cell electrophysiology prevents the construction of a bottom-up, data-driven model, in contrast to what has been accomplished for example for human β-cells [56, 57]. We included calcium-induced calcium release (CICR) in the model, since MIN6 cells are known to have RyRs [58]. The reduced Ca^{2+} amplitude seen in experiments with Tg also indicates that CICR is playing a role in MIN6 cells. In contrast, in mouse islets Tg increases the amplitude of cytosolic Ca^{2+} oscillations [26] since the ER no longer takes up Ca^{2+}. In MIN6 cells, the ER likely functions both as a sink (due to SERCA) and a source (due to CICR) when cytosolic Ca^{2+} concentration increases. The varying strengths of these two mechanisms likely underlie the heterogeneity seen in the amplitude responses to Tg and moderate ROS/RNS levels (Fig. 3.2.4E). Indeed, augmenting the role of CICR in our model can lead to reduced Ca^{2+} amplitude in response to SERCA block (Fig. 3.3.1).

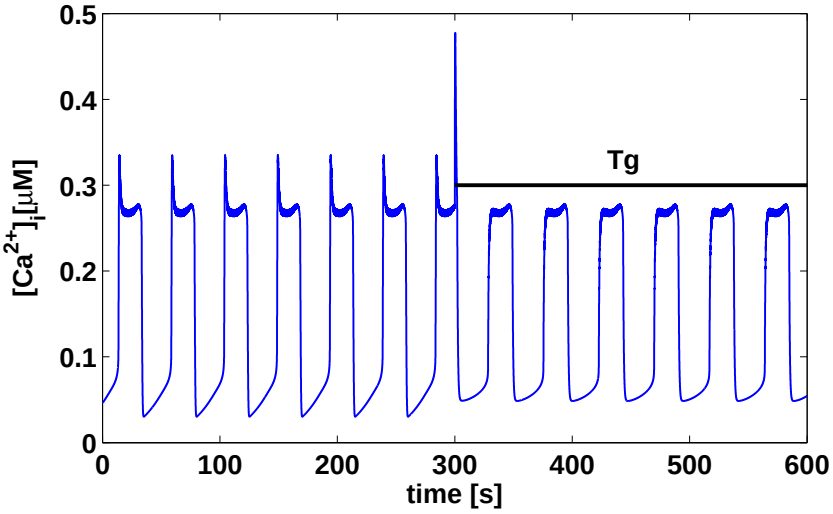

Figure 3.3.1: When CICR is playing a major role, causing a peak at the beginning of each Ca^{2+} rise, SERCA block (k_{SERCA}=0 ms^{-1} as indicated by the bar "Tg") reduces Ca^{2+} oscillation amplitude. Model simulation as in Fig. 3.2.5a, but with K_{cicr} =0.3 μM, p_{min}=0.001 ms^{-1}, pmax=0.1 ms^{-1}, $g_{k(Ca)}$=10 pS, and K_D=0.2 μM.

In summary, we show that ROS/RNS can abolish or accelerate Ca^{2+} oscillations in insulin secreting cells, which might have important con-

sequences for the disturbances of oscillatory β-cell function seen in early stages of diabetes. Our experiments and model simulations suggest that moderate ROS/RNS levels act of ER Ca^{2+} handling mechanisms, whereas higher levels of ROS/RNS also target other components involved in creating oscillatory behavior in insulin secreting cells.

2

4

Spatio-temporal simulation of calcium and granule dynamics in Pituitary cells

Endocrine cells of the pituitary gland (i.e., melanotrophs, lactotrophs, somatotrophs, thyrotrophs, corticotrophs, and gonadotrophs) secrete a number of hormones and are regulated by the hypothalamus [59]. These hormones act on other endocrine glands and other tissues including the brain to regulate physiological and behavioral aspects of growth, metabolism, water balance, and reproduction [60]. The endocrine pituitary cells contain a wide variety of ion channels and are electrically excitable, and hormone secretion occurs due to an elevation in the intracellular Ca^{2+} concentration that often accompanies electrical activity [10]. Common behaviors of the cells include continuous spiking typically observed in luteinizing hormone-secreting gonadotrophs under basal conditions and

a form of bursting known as pseudo-plateau bursting often observed in prolactin-secreting lactotrophs, growth hormone-releasing somatotrophs, and ACTH-secreting corticotrophs, where the burst duration is at most a few seconds and the spikes that ride on the elevated voltage plateau are very small [61, 62]. Each electrical event brings Ca^{2+} into the cell, and this Ca^{2+} is responsible for exocytosis of hormone-filled granules. Simultaneous measurements of both electrical activity and Ca^{2+} concentration have established that the amplitude of Ca^{2+} fluctuations is greater in a bursting cell than in a spiking cell [59] leading to the hypothesis that bursting cells release more hormone than spiking cells [61, 63]. Experimentally exploring this hypothesis will require simultaneous measurements of electrical activity and release from single cells. In this Chapter computer simulations will be used to explore the hypothesis that pseudo-plateau bursting evokes more secretion than continuous spiking.

The approach that we use is to directly measure electrical spiking and bursting patterns from pituitary cells and use these data as input to mathematical models of Ca^{2+} channel activity, Ca^{2+} diffusion and binding to buffer, and finally Ca^{2+}-driven exocytosis. The model parameters are set according to prior data and models, but one major unknown factor is the geometrical arrangement of Ca^{2+} channels and docked granules at the plasma membrane. We consider the secretion response to stochastic single channels as well as small clusters of stochastic channels, and vary the distance of the channels from the release sites. Our objective is to determine how these factors affect the differential secretion evoked by spiking electrical activity vs. bursting electrical activity.

We find that bursting is typically more effective at evoking secretion than is continuous spiking. When bursting is induced in a spiking gonadotroph by injecting a BK-type K^+ current with dynamic clamp, our model simulations suggest that the burst pattern is generally at least as effective as continuous spiking at evoking hormone release, and is often considerably more effective. We demonstrate that the degree of superiority of bursting over spiking depends on the channel configuration, which would likely vary from cell-to-cell. We also demonstrate that the

bursting reappearing in an endogenously bursting pituitary cell, after previously pharmacologically blocking the native BK current and subsequently adding a BK current using dynamic clamp, is superior at evoking secretion than the pharmacologically induced spiking behavior. Thus, we demonstrate with this hybrid experimental/modeling approach that adding a K^+ current, which is typically associated with decreased cell activity and reduced secretion, can actually produce an increase in hormone secretion, as suggested earlier [61].

4.1 Electrical Activity Recordings

Despite the similar origin of somatotrophs, lactotrophs and gonadotrophs, they show differences in terms of pattern of spontaneous electrical activity, intracellular Ca^{2+} signaling and basal hormone secretion [62]. In order to investigate the origin of such variety among these cell types, in [61] differences in the ionic conductances have been examined. The authors found that although a subset of same ion channels is expressed in each cell type, difference in BK channels expression plays a key role in the production of diverse voltage patters between gonadotrophs and somatotrophs/lactotrophs. For example, BK channels are expressed at higher levels in somatorophs and lactotrophs than in gonadotrophs. This correlation between BK channels density and pattern of electrical activity suggests that larger BK conductance favors the generation of bursting activity and global Ca^{2+} signals. As a result, blockade of BK channels in somatotrophs/lactotrophs lead to the switch from bursting to spiking, while the addiction of an artificial BK current can switch the spiking pattern of gonadotrophs into bursting.

We recorded from a rat gonadotroph or from a GH4C1 lactosomatotroph cell voltage time courses and we used these recordings as inputs to our mathematical models. We used traces consisting of continuous spiking patterns, and traces of fast pseudo-plateau bursting caused by adding a BK-type current to a spiking cell with the dynamic clamp technique. Each of these traces is fed into a mathematical model consist-

ing of stochastic Ca^{2+} channels coupled to reaction-diffusion equations that describe Ca^{2+} transport through the cell. Finally, the computed Ca^{2+} concentration is used to drive an exocytosis model based on Ca^{2+} binding to granules, granule fusion with the membrane, and resulting hormone release

EXPERIMENTAL

GH4C1 cells were maintained in culture conditions in supplemented F10 medium (Sigma-Aldrich, St-Louis, MO) according to established procedures [64]. Primary pituitary cells were obtained from diestrous female rats (Sprague Dawley, aged 3-6 months) using enzymatic dispersion of pituitary fragments [65]. Animal procedures were approved by the Florida State University Animal Care and Use Committee. Cells were cultured in supplemented M199 medium (Invitrogen, Carlsbad, CA) for one day before being used for patch clamp experiments. Gonadotrophs were identified by their larger size and by their typical rhythmic hyperpolarizations in response to 1 nM gonadotropin-releasing hormone (Bachem, Torrance, CA) applied at the end of the experiment [66].
During the patch-clamp experiments, cells were superfused with Hepes-buffered saline (138 mM NaCl, 5mM KCl, 10 mM D-glucose, 25 mM HEPES, 0.7 mM Na2HPO4, 1 mM MgCl2, 2 mM CaCl2) at room temperature. Patch pipettes (resistance 6-9 MOhm) were filled with solution containing 90 mM KAsp, 60 mM KCl, 10 mM HEPES, 1 mM MgCl2 with the addition of 120 g/ml amphotericin B. Usually, access resistance decreased below 50 MOhm within 10 minutes following seal ($>$ 5 GOhm) formation. BK channels were blocked by bath application of 100 nM iberiotoxin (Tocris).

DYNAMIC CLAMP

Membrane potential was recorded in current clamp (bridge mode) and output from the patch amplifier (Multiclamp 700B, Molecular Devices, Sunnyvale, CA) was read through an analog to digital acquisition card

(DAQ) on a PC running the software QuB with a dynamic clamp module [21]. Membrane potential (V) was used to compute the current going through the BK channels:

$$I_{BK} = g_{BK} f(V_K - V), \tag{4.1}$$

with f obtained by integrating in real time using the forward Euler method [21], with dt average = 54 μs, maximum = 100 μs, and the steady state BK channel activation given by:

$$f_\infty(V) = [1 + e^{v_f - V}/s_f]^{-1}. \tag{4.2}$$

The calculated BK current was injected back into the cell through the same DAQ. The parameter values were: g_{BK}=0.5-1 nS; τ_{BK} = 5-10 ms; v_f =-15 mV; s_f=1 mV.

4.2 Calcium Diffusion Simulations

Geometry

To model data from pituitary cells we represented a single cell by a sphere with a diameter of 13 μm [67]. Based on whole-cell calcium conductance of $\sim$1.5-2 nS [62], and single channel conductance $\sim$20 pS [68], we assumed that a cell possesses 75 functional L-type Ca^{2+} channels. In our simulations we considered two different configurations for the channel distribution over the sphere surface: channels were either uniformly distributed and each release site affected by a single channel, or there were clusters composed of 5 channels, and each release site affected by a single cluster. In the single channel case, Ca^{2+} diffusion was computed in a conical region with base radius of 1.5 μm (Fig. 4.2.1), a radius obtained by dividing the sphere surface into 75 circular areas, one for each channel. This radius corresponds to an inter-channel distance of $\sim$3 μm, in agreement with [69]. The single channel conductance was set to 20 pS [68]. In the case of channel clusters, Ca^{2+} diffusion was simulated in a conical re-

gion with a base radius of 3.3 μm, corresponding to dividing the sphere surface into 15 circular areas. In both cases, the Ca^{2+} current source was located at the base center of the conical region. We implemented no-flux boundary conditions for Ca^{2+} and buffers on the sides of the cone. This assumption means that Ca^{2+} flowing out of the conical region equals the flux into the cone from adjacent regions, or in other words, that the Ca^{2+} channels in adjacent cones contribute to Ca^{2+} levels in the cone of study exactly as the Ca^{2+} channel or cluster under study influences the adjacent regions. Because of the conical geometry, the full 3-dimensional problem was reduced to a 2-dimensional problem, using rotationally symmetric spherical (r, θ) coordinates, thus reducing the computational requirements. Since the granules participating in hormone secretion are located just below the membrane [70], we focused our attention on the submembrane Ca^{2+} profiles along the plasma membrane.

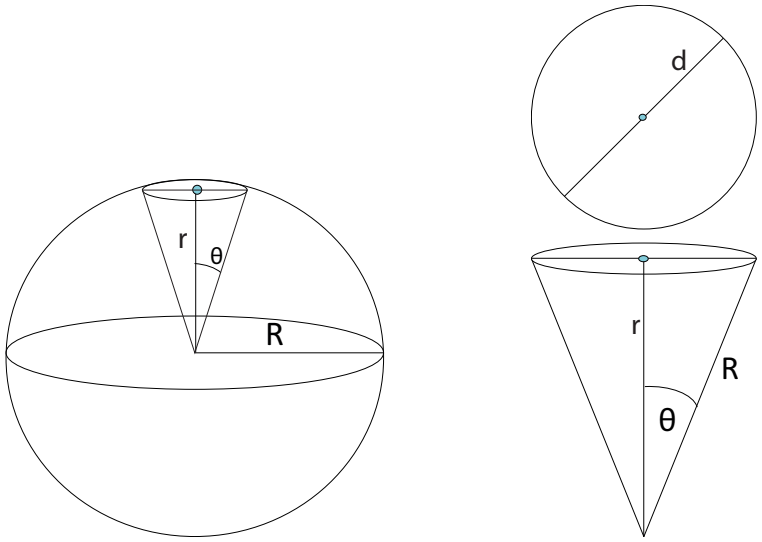

Figure 4.2.1: Spherical cell model used in simulations. The cell diameter is 13 μm. Ca^{2+} diffusion and buffering are simulated in a conical region of the sphere. The channel or channel cluster is located at the center of the cone base on the surface of the sphere. The base radius in the single channel case is 1.5 μm and in the cluster case 3.3 μm

Stochastic Channel Gating

For the single Ca^{2+} channel, we assumed three states with kinetic mechanism described by [71] where the states are closed (C), open (O), and blocked or inactivated (B).

$$C \underset{\beta(V)}{\overset{\alpha(V)}{\rightleftarrows}} O \underset{k_-}{\overset{k_+}{\rightleftarrows}} B. \tag{4.3}$$

By defining a random variable s, which can take values of the three states C, O, B the probability that $s(t) = i$ is written as $P_i(t)$. Since the channel must always be in one of the three states:

$$P_C(t) + P_O(t) + P_B(t) = 1. \tag{4.4}$$

When the channel is in the state C at time t, the probability that the channel can open in a short interval of time Δt is given by:

$$\alpha(V)\Delta t = Prob\{s = O, t + \Delta t | s = C, t\}, \tag{4.5}$$

where $\alpha(V)\Delta t$ is dimensionless. Multiplying by $P_C(t)$, that is the probability that the ion channel is indeed in state C, we find that $\alpha(V)P_C(t)\Delta t$ is the probability that the transition from C to O actually occurs. According to (4.3) the closed state can be left or be reached in two possible ways:

$$P_C(t + \Delta t) = P_C(t) - \alpha(V)P_C(t)\Delta t + \beta(V)P_O(t)\Delta t \tag{4.6}$$

Similarly, an equation relating $P_O(t + \Delta t)$ and $P_O(t)$ can be written. By taking the limit $\Delta t \to 0$ we get the continuous system:

$$\frac{dP_c}{dt} = -\alpha(V)P_C + \beta(V)P_O, \tag{4.7}$$

$$\frac{dP_B}{dt} = -k_- P_B + k_+ P_O, \tag{4.8}$$

$$P_O = 1 - P_B - P_C. \tag{4.9}$$

The rate constants $\alpha(V)$ and $\beta(V)$ are determined by $\alpha = m_\infty/\tau_m$, $\beta = 1/\tau_m - \alpha$ [22] using a steady-state activation function m_∞ and time constant τ_m obtained from experiments. Based on data from GH3 cells [67, 69], which have Ca^{2+} channel characteristics similar to GH4 cells [67], and in agreement with Sherman et al. [71], we set $\tau_m = 1.25$ ms. The steady-state activation function is

$$m_\infty = \frac{1}{1 + \exp[(V_m - V)/s_m]}, \tag{4.10}$$

with $V_m = -4$ mV and $s_m = 7$ mV [69]. With regards to channel inactivation, some types of Ca^{2+} channels are inactivated by Ca^{2+}, while others exhibit voltage-dependent inactivation. We found that fixed rate constants $k = 0.018$ ms^{-1} and $k_+ = 0.0324$ ms^{-1} are sufficient to match inactivation experimentally observed in [69]. The stochastic channel dynamics [72] is simulated as realizations of the discrete-state continuous-time Markov chain with transition probabilities for a small time step Δt described by:

$$\begin{bmatrix} O(t+\Delta t) \\ C(t+\Delta t) \\ B(t+\Delta t) \end{bmatrix} = \begin{bmatrix} 1-(\beta+k_+)\Delta t & \alpha\Delta t & k_-\Delta t \\ \beta\Delta t & 1-\alpha\Delta t & 0 \\ k_+\Delta t & 0 & 1-k_-\Delta t \end{bmatrix} \begin{bmatrix} O(t) \\ C(t) \\ B(t) \end{bmatrix}, \tag{4.11}$$

Monte Carlo simulations are performed and the single-channel open-state O(t) was used to compute the single-channel current as (Fig 4.2.2):

$$I_{SC}(t) = g_{SC} O(t)(V(t) - V_{Ca}), \tag{4.12}$$

where g_{sc} is the single channel conductance. In the cluster case, the total current is simulated by summing 5 independent realizations of a single channel current (I_{sc}). Both the current driving force and open probability are coupled to the time-varying membrane potential $V(t)$. Specifically, the driving force decreases as $V(t)$ increases towards the Ca^{2+} reversal potential V_{Ca} whereas the open probability increases with $V(t)$.

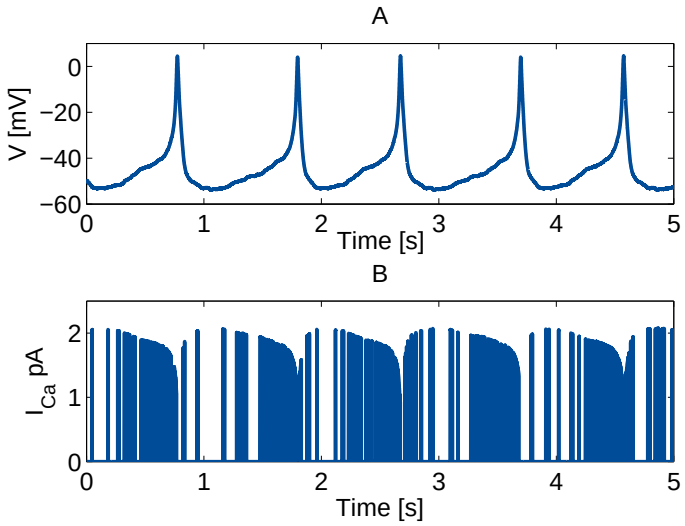

Figure 4.2.2: A) Actual spiking voltage traces recorded from a gonadotroph and B) stochastic current simulation of a single channel (I_{SC}) coupled to the spiking voltage pattern.

CALCIUM DIFFUSION

In all simulations we assume the presence of a single immobile endogenous Ca^{2+} buffer, in agreement with Kits et al. [70], and no mobile buffers are considered. Binding of Ca^{2+} to the buffer is described by simple mass action kinetics with one-to-one stoichiometry,

$$B + Ca^{2+} \underset{k_{off}}{\overset{k_{on}}{\rightleftarrows}} CaB, \tag{4.13}$$

where k_{on} and k_{off} are association and disassociation rates, respectively. The reaction-diffusion equations for the Ca^{2+} concentration and for the free unbound buffers are taken from [73]:

$$\begin{aligned}\frac{\partial[Ca^{2+}]}{\partial t} &= D_{Ca} \bigtriangledown^2 [Ca^{2+}] - k_{on}[Ca^{2+}][B] + k_{off}(B_{total} - [B]) \\ &\quad + \frac{1}{2F}\delta(r - R, \theta) - k_{uptake}([Ca^{2+}] - [Ca^{2+}]_0),\end{aligned} \tag{4.14}$$

$$\frac{\partial[B]}{\partial t} = -k_{on}[Ca^{2+}][B] + k_{off}(B_{total} - [B]), \tag{4.15}$$

where D_{Ca} is the diffusion coefficient for unbound Ca^{2+}. We choose D_{Ca}=0.2 μm^2 ms^{-1} [72] and assume that the distribution of the immobile buffer is spatially uniform. The second-to-last term in (4.14) represents Ca^{2+} influx, where F is Faraday's constant, I_{sc}(t) is the (inward) single-channel (or 5-channel-cluster) calcium current, and $\delta(r - R, \theta)$ is the Dirac delta function centered at $r = R$ and $\theta = 0$ (i.e., at the center of the base of the cone). The last term defines net Ca^{2+} uptake into internal stores such as the endoplasmic reticulum with constant rate $k_{uptake} = 0.3$ $\mu M/ms^{-1}$. $[Ca^{2+}]_0$ is the Ca^{2+} concentration in case of no Ca^{2+} influx and spatiotemporal equilibrium. In accordance with simulation studies performed by Kits et al. [70] in melanotroph cells, we set the endogenous buffer parameters $k_{on} = 0.1$ μM^{-1} ms^{-1}, $K_D = k_{off}/k_{on} = 10$ μM, and $B_{total} = 900 \mu M$. No-flux boundary conditions hold for Ca^{2+} at all boundaries. The reaction-diffusion equations are solved using the Calcium Calculator (CalC) software, section 2.6, (Example of a calcium diffusion simulation with one channel is shown in 4.2.3).

4.3 EXOCYTOSIS MODEL

We initially used a 6-pool exocytosis model [74], which describes the fraction of granules in various pools of granules described as docked, primed, domain bound, or in one of three pre-fusion states distinguished by the number of bound Ca^{2+} ions. Fusion states are distinguished by the number of bound Ca^{2+} ions. However, for the relatively short time courses used here (5 sec), our preliminary simulations showed no significant differences between this 6-pool model and a simpler 4-pool model in which the docked, primed, and domain bound pools were combined into a single pool that we call the "primed" pool. We use this simplified model (Fig. 4.3.1), which is similar to a model of exocytosis in melanotroph cells [75], in all simulations. Here, the granule can be in one of four different states: a primed state where the granule is adjacent to the

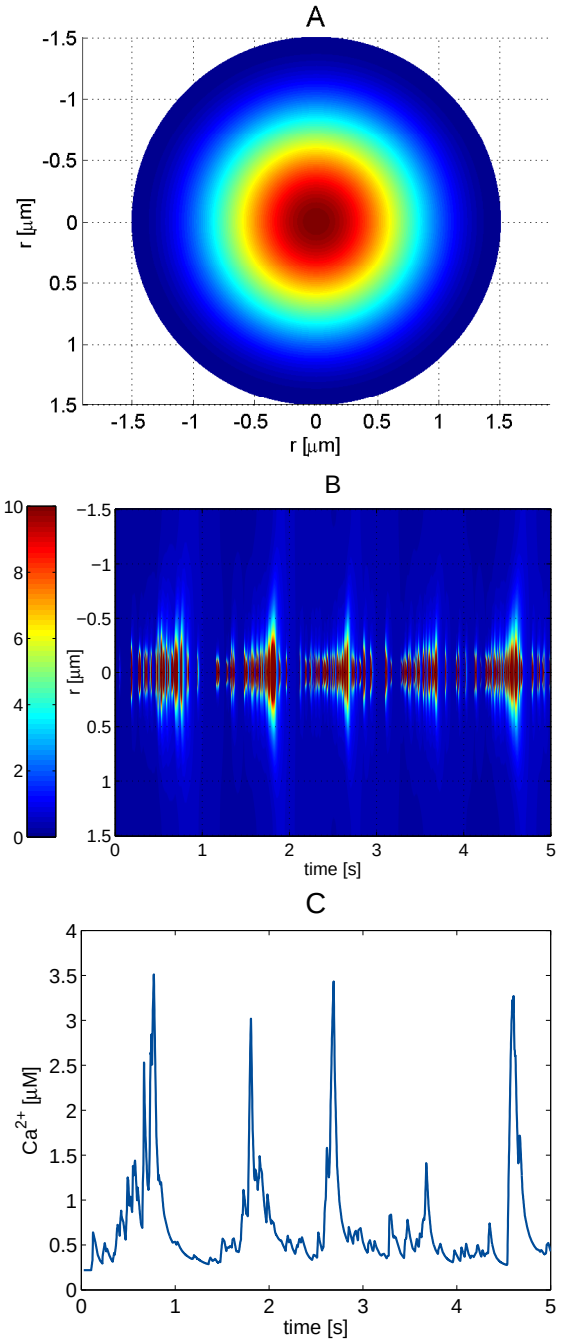

Figure 4.2.3: A) Submembrane Ca^{2+} concentrations diffusion at the base of the cone. B) Submembrane Ca^{2+} concentrations (color coded, in μM) as a function of time and the distance to the channel (d) during spiking electrical activity. C) Ca^{2+} concentration at 500 nm from the channel as function of time

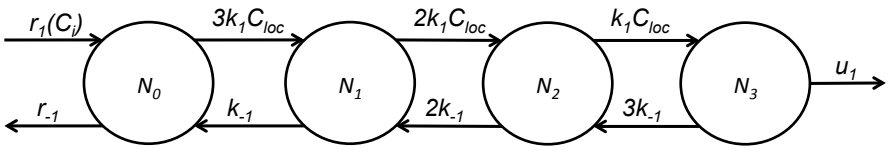

Figure 4.3.1: Kinetic scheme of the exocytosis model. The pool N_0 consists of granules primed for fusion and its resupply depends on the bulk cytosolic Ca^{2+} concentration C_i. Fusion occurs upon Ca^{2+} binding controlled by the local concentration of Ca^{2+}, C_{loc}. The pools N_1, N_2, N_3 correspond to the three Ca^{2+} bound states, and u_1 is the fusion rate.

plasma membrane (N_0), or states in which one (N_1), two (N_2), or three (N_3) Ca^{2+} ions are bound to the Ca^{2+} sensor, likely synaptotagmin [59]. Once in state N_3 the granule fuses with the membrane and releases its hormone content at rate u_1. Granule release is triggered by local Ca^{2+} levels (C_{loc}), as indicated in Fig.4.3.1, while resupply is dependent on the bulk calcium concentration C_i, which is computed as the submembrane Ca^{2+} concentration 1.5 μm from the channel. The rate of resupply per cell r_1 is

$$r_1 = \frac{C_i(t) r_0^1}{C_i(t) + K_p}, \tag{4.16}$$

with $K_p = 2.3$ μM [74, 76], and r_0^1 is the maximal resupply rate per cell.

All secretion model steps are assumed to be reversible, except for fusion. The local Ca^{2+} concentration is determined by solving the Ca^{2+} reaction-diffusion equations and using the Ca^{2+} value at the release site (4.14)(4.15). The exocytosis model describing release per cell is given by the following differential equations:

$$\frac{dN_0}{dt} = -(3k_1C_{loc}(t) + r_{-1})N_0 + r_1(C_i(t)) + k_{-1}N_1, \tag{4.17}$$
$$\frac{dN_1}{dt} = -(2k_1C_{loc}(t) + k_{-1})N_1 + 3k_1(C_{loc}(t))N_0 + 2k_{-1}N_2, \tag{4.18}$$
$$\frac{dN_2}{dt} = -(k_1C_{loc}(t) + 2k_{-1})N_2 + 2k_1(C_{loc}(t))N_1 + 3k_{-1}N_3, \tag{4.19}$$
$$\frac{dN_3}{dt} = -(u_1 + 3k_{-1})N_3 + k_1(C_{loc}(t))N_2, \tag{4.20}$$

where N_i is the number of granules in pool i. Experimental data [77] indicate a relatively low Ca^{2+} binding affinity; as a consequence, we use the Ca^{2+} affinity value $k_d = k_{-1}/k_1 = 27$ μM in Eqs. (4.17)-(4.20). We used two sets of initial conditions for the granule/exocytosis model. In the model of Chen et al. [74] the number of primed granules (pool N_0) is equal to 40 per cell. Hence, we set as initial condition N_0=40 primed granules, each a fixed distance from a single channel (so 35 channels are not associated with granules). Assuming that – in any one simulation – all Ca^{2+} channels in the cell behave identically according to the Markov simulation, the granules will be exposed to the same Ca^{2+} profile. To calculate average cellular exocytosis, we performed 10 (single channel) or 5 (cluster) simulations and computed average values of N_i at each time point. This initial condition ($N_0 = 40$) reflects experiments such as single-cell capacitance measurements of triggered exocytosis, where no exocytosis is occurring before the experiment [77, 78]. For interpreting hormone secretion experiments, where secretion is ongoing, the steady state of the model is more relevant. We found that the pools empty within seconds (see Results), and therefore considered initial conditions where all pools are empty to reflect secretion experiments. The exocytosis rate per cell is

$$J_F(t) = u_1N_3(t), \tag{4.21}$$

where N_3 is the average of granules in state 3 of 10 or 5 simulations (ex-

plained above). The cumulative number of fused granules per cell is

$$M_F(t) = \int_0^t u_1 N_3(t')dt'. \tag{4.22}$$

To show how much of the simulated secretion is due to increased Ca^{2+} influx during bursting compared to spiking electrical activity, that is, to investigate whether bursting increases the Ca^{2+}-current sensitivity of exocytosis [79], we relate exocytosis to the total charge entering via the Ca^{2+} channel or channel cluster [79]:

$$Q(t) = \int_0^t I_{SC} ds. \tag{4.23}$$

All the default parameters are reported in Table 4.3.1.

4.4 Simulation Results

Single channel

Gonadotrophs release little luteinizing under basal conditions, which has been suggested to be associated to their typical spiking electrical behavior [62]. The addiction of a BK-type K^+ current to a spiking gonadotroph can change its behavior into bursting [64]. Figure 4.4.1 shows an example of such a cell where the injected BK-type current induces bursting in an otherwise spiking gonadotroph. We also show the average of 10 independent simulations, each with a stochastic Ca^{2+} channel providing Ca^{2+} to the interior of the cell and subsequent Ca^{2+} diffusion. The Ca^{2+} model is driven by either the spiking voltage pattern (left) or the bursting pattern (right) obtained by injecting a BK-type K^+ current via dynamic clamp. Average Ca^{2+} profiles are reported at distances of 30, 200, and 1500 nm from the Ca^{2+} channel. As expected, close to the channel, i.e., 30 nm, Ca^{2+} reaches high concentrations of some tens of micromolar on average with peaks up to $\sim$70 μM during spiking activity and $\sim$110 μM

Parameter	Value	Unit
	Current Simulation	
s_m	7	mV
v_m	-4	mV
k_+	0.0234	ms^{-1}
k_-	0.018	ms^{-1}
g_{Ca}	20	pS
	Diffusion Simulation	
D_{Ca}	0.22	$\mu\text{m}^2/\text{ms}$
B_{total}	900	μM
K_D	10	μM
k_{on}	0.1	$\mu\text{M}^{-1}\ \text{ms}^{-1}$
k_{off}	1	ms^{-1}
$[Ca^{2+}]_0$	0.22	μM
	Secretion Model	
k_1	3.7	$\mu\text{M}^{-1}\text{s}^{-1}$
k_{-1}	100	s^{-1}
r_1^0	3.6	s^{-1}
K_p	2.3	μM
r_{-1}	0.001	s^{-1}
u_1	1000	s^{-1}

Table 4.3.1: Default parameters of the Ca^{2+} channel, Ca^{2+} diffusion simulations and exocytosis model.

during bursting. The traces are very noisy due to the stochastic openings of the Ca^{2+} channel. The average Ca^{2+} concentration decreases with distance from the channel, reaching less than 1 μM at a distance of 1500 nm. In addition, the noise is attenuated due to the effects of diffusion, which acts as a low-pass filter. Ca^{2+} measurements using a fluorescent dye such as fura-2 report on the Ca^{2+} concentration averaged over the cell, and have time courses similar to those shown in the bottom row of Fig. 4.4.1 [59, 80].

We now locate the exocytosis machinery at different distances from the Ca^{2+} channel and use the Ca^{2+} concentration at that location to drive the exocytosis model (Fig. 4.3.1 and (4.17)-(4.20)). Figure 4.4.2 shows the average number of fused granules over time at different distances. If the release site is 30 nm from the channel, it is exposed to very high Ca^{2+} concentrations, whether the cell is spiking or bursting, and exocytosis occurs at its maximum rate that releases all the granules in the primed pool N_0 (40 granules) very soon after the start of the input train. A similar result occurs if the release site is located 100 nm from the channel. Thus, if the release site and channel are within 100 nm of each other it does not matter whether the cell is spiking or bursting, the secretion level will be the same, since the Ca^{2+} concentrations at the exocytotic machinery are in both cases saturating. At a distance of 200 nm there is a difference between exocytosis evoked by spiking and that evoked by bursting; the bursting pattern (solid) evokes release at a higher rate than the spiking pattern (dashed), though both release almost all available granules by the end of the 5 second input train. The advantage of bursting over spiking is amplified when the release site is situated further from the channel, at 300 nm or 500 nm. Even though the absolute number of fused granules is lower when the channel and the release site are more distant, the bursting voltage trace releases more granules than the spiking trace at all time points. Thus, our simulations support the notion that adding an outward K^+ current can, by changing spiking to bursting activity, counterintuitive increase secretion [10, 81].

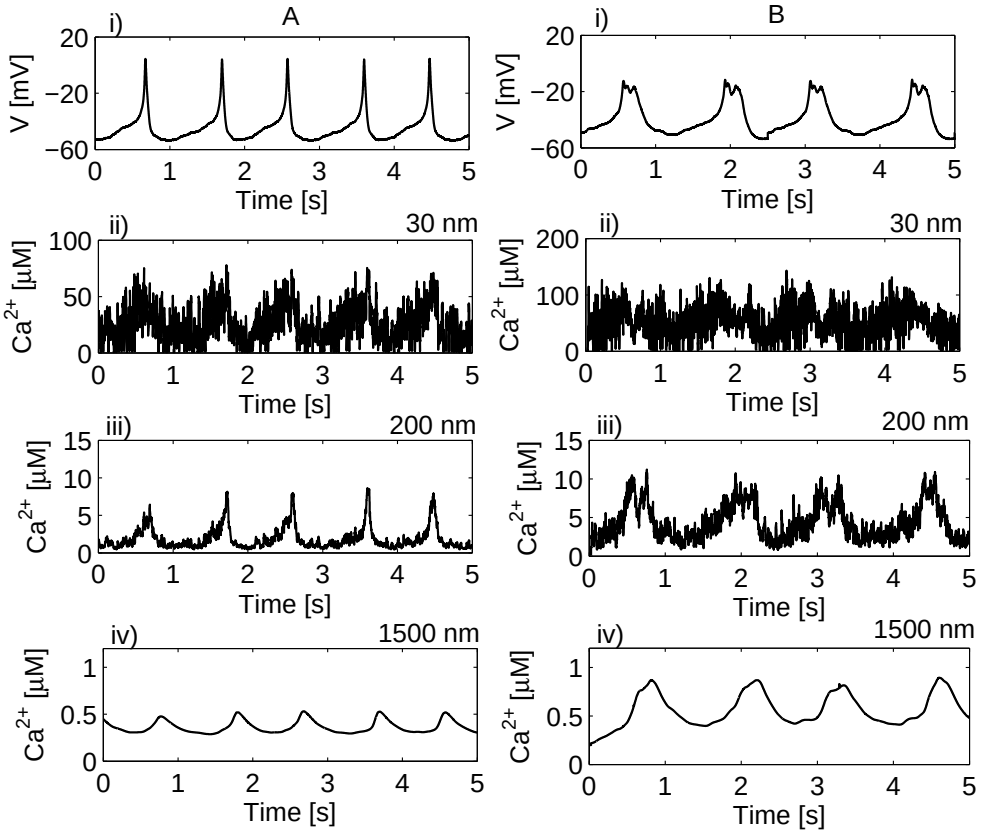

Figure 4.4.1: Ca^{2+} concentration at different distances from a single stochastic Ca^{2+} channel on the surface of a conical region (average of 10 independent trials). The Ca^{2+} channel is placed at the center of the cone base with radius 1.5 μm. The Ca^{2+} concentration is determined using a mathematical model, in response to actual spiking (A) and bursting (B) voltage traces from a gonadotroph. The switch to bursting was obtained by injecting a model BK-current into a spiking cell using the dynamic clamp technique.

These observations imply that the primed pool of granules can be emptied very quickly, and this fusion process is likely monitored with capacitance measurements of exocytosis that take place over a short period of time [70]. In our data, the spiking voltage trace shows 5 spikes in 5 seconds, each spike lasting ∼40 ms (Fig. 4.4.1Ai). On average, each 40 ms depolarization of a pulse train was found to evoke ∼10 fF of exocytosis [15]. Thus, based on these experiments we expect ∼50 fF exocytosis during the 5 seconds in Fig. 4.4.2. In our simulations, exocytosis at a distance of 200 nm from the channel is ∼30 granules. If we assume that a single granule corresponds to ∼2 fF [82, 83], we get a capacitance measurement of ∼60 fF, close to the ∼50 fF calculated from [15].

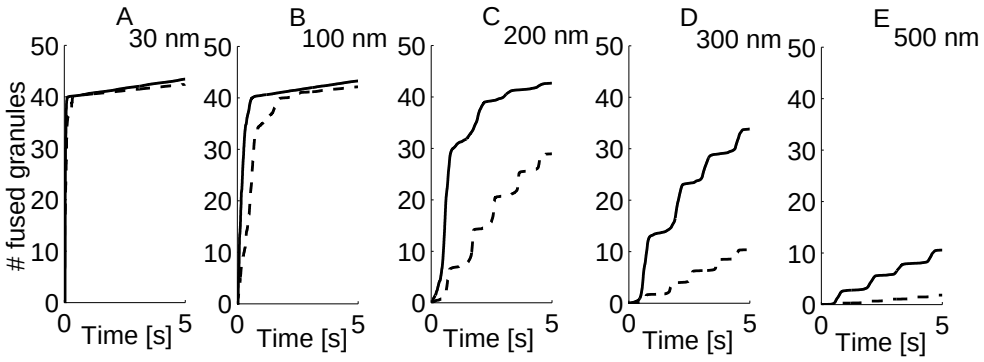

Figure 4.4.2: Single channel exocytosis simulation results with N_0=40 primed granules as initial condition. Number of fused granules (average of 10 simulations) during spiking (dashed curve) and bursting (solid curve) electrical activity for different distances between the single Ca^{2+} channel and a release site as a function of time.

However, most secretion measurements are made from a cell population over a period of minutes or tens of minutes. In such measurements the resupply of the primed pool by the reserve granule pool is rate limiting. We next look at the effects of resupply by emptying the primed pool N_0 at the beginning of the simulation and from this initial condition evaluate the differential exocytosis evoked by spiking and bursting.

The cumulative number of fused granules as a function of time is shown in Fig 4.4.3 (top panel). Bursting evokes more release regardless of the distance between the channel and the granule. This is in spite of the

fact that at short distances the local Ca^{2+} concentration saturates the release site, and highlights the importance of the dependence of resupply on the global, rather than local, Ca^{2+} concentration. That is, the simulated global Ca^{2+} concentration is higher during bursting than during spiking, as measured by fluorescent dyes [21], and this results in a greater rate of resupply in response to bursting. When the channel is close to the release site all granules becoming available due to the resupply are fused almost immediately, so resupply is rate limiting. Farther than 200 nm from the channel, local Ca^{2+} concentrations start to play a predominant role since the exocytosis machinery is no longer saturated, and therefore differences in local Ca^{2+} levels as well as global levels are responsible for differences in the exocytosis rates.

There are two factors that could contribute to the greater effectiveness of bursting at evoking secretion in the model. One is that bursting brings in more Ca^{2+} over the 5 seconds of simulation time, increasing resupply rate relative to spiking, as mentioned above. The other is that the dynamics of Ca^{2+} diffusion and the exocytotic machinery favor the bursting signal over the spiking signal. That is, bursting is more efficient than spiking at evoking release. To test the latter, we plot the number of fused granules versus the total Ca^{2+} entry Q (Fig. 4.4.3, bottom panels). For release sites closer than 200 nm from the channel the efficiency of the spiking and bursting patterns are virtually the same. It is only at distances of 200 nm or greater that bursting becomes more efficient than spiking, since at these distances the number of fused granules per total Ca^{2+} entry is larger when the cell is bursting. This is due to the longer duration of the bursting events, which produce longer-duration Ca^{2+} signals that are advantageous for the exocytosis machinery that requires the binding of three Ca^{2+} ions to evoke granule fusion. In fact, in simulations in which only two Ca^{2+} ions are needed to evoke fusion the efficiency of spiking and bursting are the same at a 200 nm distance, and bursting is only slightly more efficient at 300 and 500 nm distances (not shown).

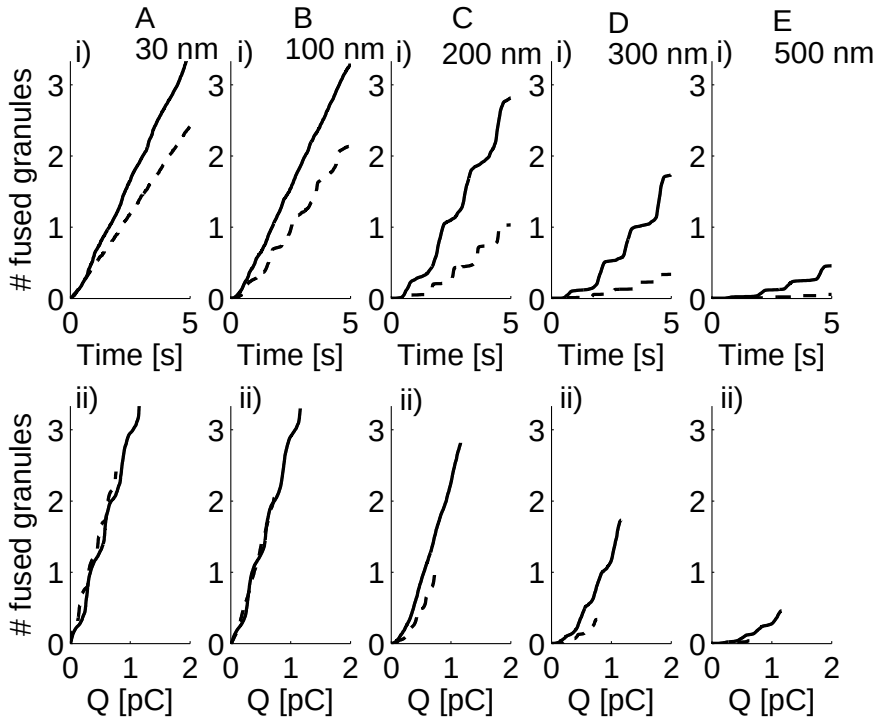

Figure 4.4.3: Single channel exocytosis simulation results with all the pools initially empty. Top panels (i) show the number of fused granules as a function of time, as in Fig. 4.4.2. Bottom panels (ii) show the cumulative number of fused granules during 5 seconds of simulation as function of the cumulative calcium entry Q. (A) granules located at 30 nm, (B) 100 nm, (C) 200 nm, (D) 300 nm, or (E) 500 nm from the channel.

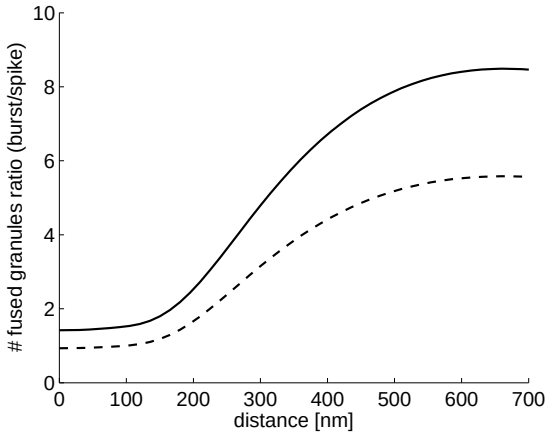

Figure 4.4.4: Summary of single channel exocytosis results with all the pools initially empty. The bursting-to-spiking ratio of the total number of fused granules during 5 seconds of electrical activity (solid line) shows that bursting evokes more secretion at all distances. In contrast, the bursting-to-spiking ratio of the total number of granules normalized to change entry Q (dashed line) shows that the efficiency of spiking and bursting are comparable for release sites located close to the channel, but that bursting has superior efficiency farther from the channel.

As a final quantification of the effectiveness of bursting vs. spiking at evoking secretion we show the ratio between bursting-evoked secretion and spiking-evoked secretion in Fig. 4.4.4 (solid line). This ratio is calculated from the total number of fused granules at the end of the 5-sec input voltage train as a function of distance between the channel and the release site. Up until a distance of 100 nm the ratio is $\sim$1.5; the burst pattern evokes a slightly higher amount of secretion than spiking. Past this distance the ratio increases continuously, reaching a value of $\sim$8.5 at a distance of 700 nm. Thus, there is between 1.5 and 8.5 times more secretion by the end of the 5-sec stimulation with bursting versus spiking. Plotting the ratio of exocytosis during spiking and bursting but normalized to the charge Q (Fig. 4.4.4, dashed line) shows that spiking and bursting have almost the same Ca^{2+} current sensitivity close to the channel (i.e., they are equally efficient at evoking release), but farther away bursting becomes more efficient than spiking, reaching a 5.5-fold higher Ca^{2+} current sensitivity at a distance of 700 nm from the channel.

In summary, our simulations suggest that LH secretion from a gonadotroph could increase substantially if the electrical pattern switched from spiking to bursting, for example because of the addition of a BK-type current.

CLUSTER OF CHANNELS

The previous simulations assumed that each release site is acted upon by Ca^{2+} from single channels, and indeed there is evidence supporting this, in both endocrine cells and in neuronal synapses [69, 84]. However, it is likely that hormone release sites receive Ca^{2+} from several channels, and there is also evidence for this [85, 86]. In the next set of simulations we consider such a situation, where a release site is affected by Ca^{2+} from a cluster of 5 stochastic Ca^{2+} channels. For simplicity we assume that these are equidistant from the release site.

Figure 4.4.5 shows the Ca^{2+} concentration at different distances from the channel cluster in response to the spiking or bursting voltage trace. Close to the cluster (30 nm), Ca^{2+} rises to a level of several hundreds of micromolar, about five times larger than in the single-channel case. At greater distances, the increase over the single-channel level is less, since now the different clusters are 6600 nm apart so that a release site located 1500 nm from a cluster is $>$5000 nm from the next nearest cluster. In contrast, with uniform distribution of the same number of channels (the single channel case), a release site located 1500 nm from one channel was located the same distance from a second channel, so it received an equal amount of Ca^{2+} from both. Hence, whereas a cluster of 5 channels provides $\sim$5 times higher Ca^{2+} levels to granules located close to the channels, a granule located 1500 nm from channels will be exposed to just $\sim$5/2=2.5 times higher Ca^{2+} concentrations in the case of channel clusters compared to the single-channel configuration.

Figure 4.4.6 (upper panels) shows that bursting is always superior to

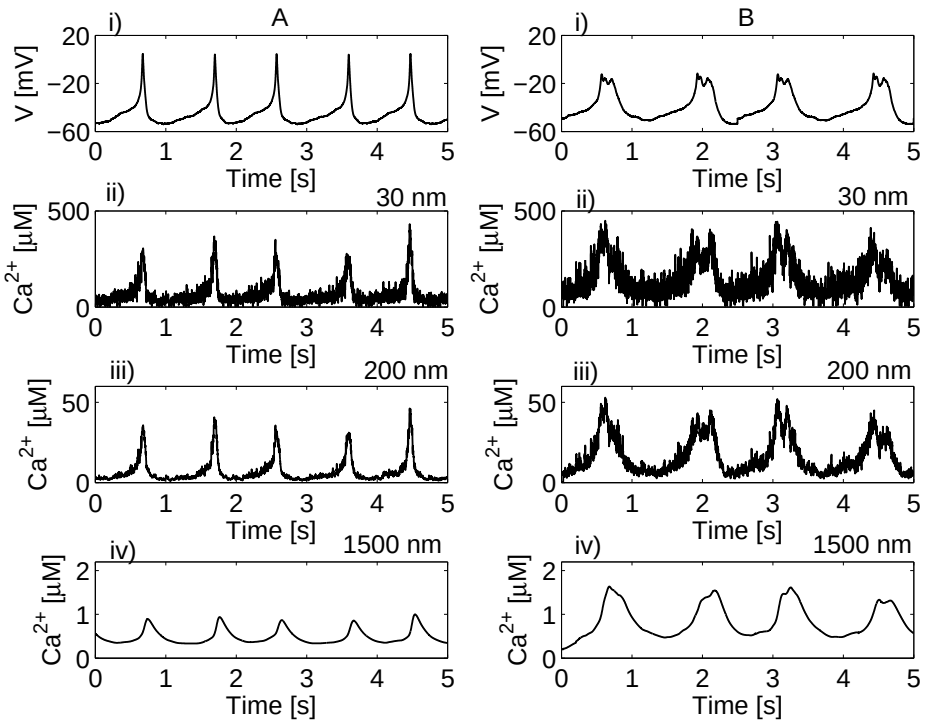

Figure 4.4.5: concentrations for a cluster of 5 channels (average of 5 independent trials). The Ca^{2+} channel is placed at the center of the cone base with radius 3.3 μm. The Ca^{2+} concentration is determined using the mathematical model, in response to actual spiking (A) and dynamic-clamp induced bursting (B) voltage traces from a gonadotroph (same traces as in Fig. 4.4.1).

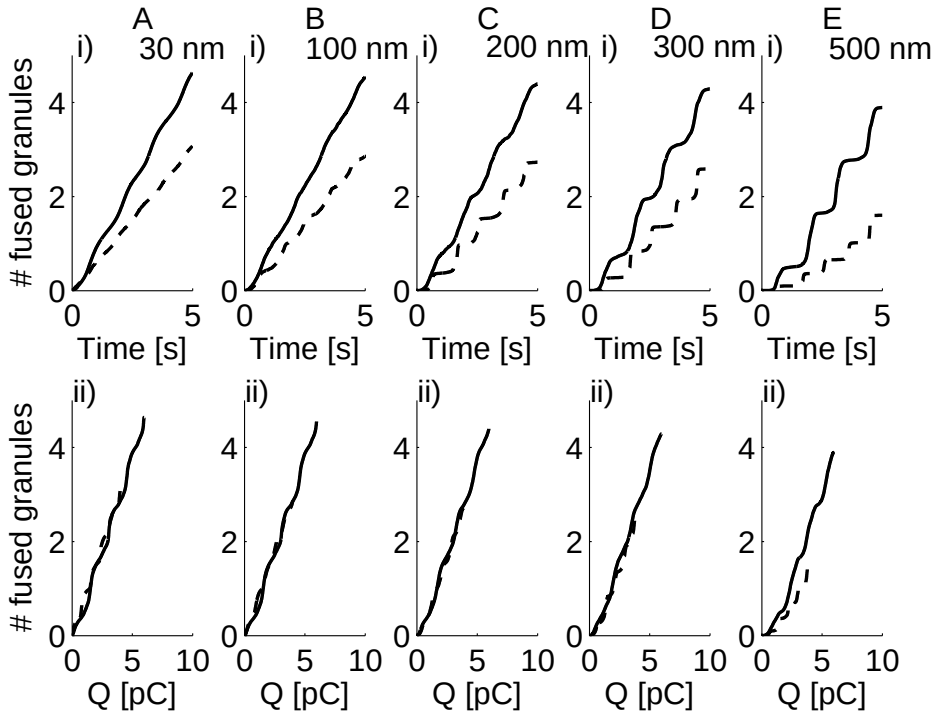

Figure 4.4.6: Channel cluster exocytosis simulation results with all the pools initially empty. Top panels (i) show the number of fused granules as a function of time, evoked by spiking (dashed curve) or bursting (solid curve). Bottom panels (ii) show the cumulative number of fused granules during 5 seconds of simulation as a function of the cumulative Ca^{2+} entry Q. (A) granules located at 30 nm, (B) 100 nm, (C) 200 nm, (D) 300 nm, or (E) 500 nm from the channel.

spiking in evoking exocytosis when channels are in clusters and the primed pool is initially empty. In contrast, the difference in Ca^{2+} current sensitivity is hardly observable when the release site is less than 300 nm from the channel cluster (Fig. 4.4.6, lower panels). It is therefore mostly the larger amount of Ca^{2+} entering during bursting that determines the difference in secretion. Figure 4.4.7 summarizes the results for channel clusters. Even at the closest release site/cluster distances the bursting-to-spiking ratio of the total number of fused granules is $\sim$1.5, and increases to $\sim$4.5 at 700 nm (solid line). The relative efficiency, i.e., the bursting-to-spiking ratio of the total number of granules normalized to Ca^{2+} entry, is $\sim$1 up to 300 nm, and increases then to $\sim$2.5 at 700 nm. Thus, just as with single-channel-evoked release, bursting provides more secretion than does spiking when exocytosis is triggered by channel clusters. However, the advantage of bursting over spiking is less, becomes manifest at greater distances for clusters than for single channels, 100 nm in Fig.4.4.3 vs. 300 nm in Fig. 4.4.6. Because the trends are qualitatively similar with single-channel and cluster-evoked secretion, we focus on only one type (single-channel secretion) in the remaining simulations.

SINGLE CHANNEL LACTO-SOMATROPH

As a second example, we now use recordings from a GH4 cell line. It has previously been shown that pseudo-plateau bursting in some pituitary cells converts to spiking when BK-type K^+ channels are pharmacologically blocked, reducing the bulk Ca^{2+} concentration [63]. Does this manipulation also result in a decrease of the domain Ca^{2+} and therefore in decreased secretion? It has been shown that bursting can be rescued by adding BK current back to the cell using the dynamic clamp technique [87]). In Fig. 4.4.8 we use both procedures. We begin with a bursting lacto-somatroph GH4C1 cell (left column), then convert it to a spiking cell by the addition of the BK channel blocker iberiotoxin (middle column), and finally convert the spiking cell back to a bursting cell using dynamic clamp to inject a model BK current (right column). For each case

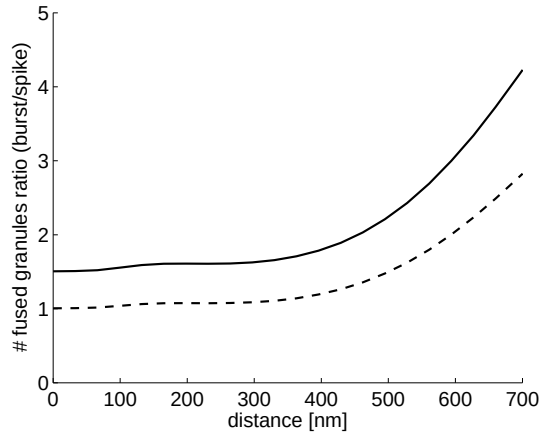

Figure 4.4.7: Summary of channel cluster exocytosis results with all the pools initially empty. The bursting-to-spiking ratio of the total number of fused granules during 5 seconds of electrical activity (solid line) shows that bursting evokes more secretion at all distances. In contrast, the bursting-to-spiking ratio of the total number of granules normalized to change entry Q (dashed line) shows that the efficiency of spiking and bursting are comparable for release sites located close to the channel cluster, but that bursting has superior efficiency farther away.

we calculate the Ca^{2+} concentration at varying distances from the single stochastic channel, as in prior simulations. Close to the channel, the Ca^{2+} concentration is about the same for all three voltage traces. However, at the greater distances, 1500 nm, the Ca^{2+} levels corresponding to the bursting voltage traces are higher than those corresponding to the spiking voltage trace, as has been observed in experiments [88].

We next use these Ca^{2+} time courses to simulate exocytosis for release sites located at different distances from the Ca^{2+} channel (Fig. 4.4.9). The results are summarized in Fig. 4.4.10, where we show the number of fused granules evoked by the dynamic clamp-induced bursting vs. that evoked by the spiking trace (solid black curve). In both cases, the ratio is near 1 up until a separation distance of $\sim$150-200 nm. At greater separations the ratio increases, indicating that at these greater distances the bursting trace is more effective at evoking exocytosis than the spiking trace. Normalizing to Ca^{2+} influx reveals that the ratio of Ca^{2+} current sensitivity is higher for spiking close to the channel (ratio < 1) whereas

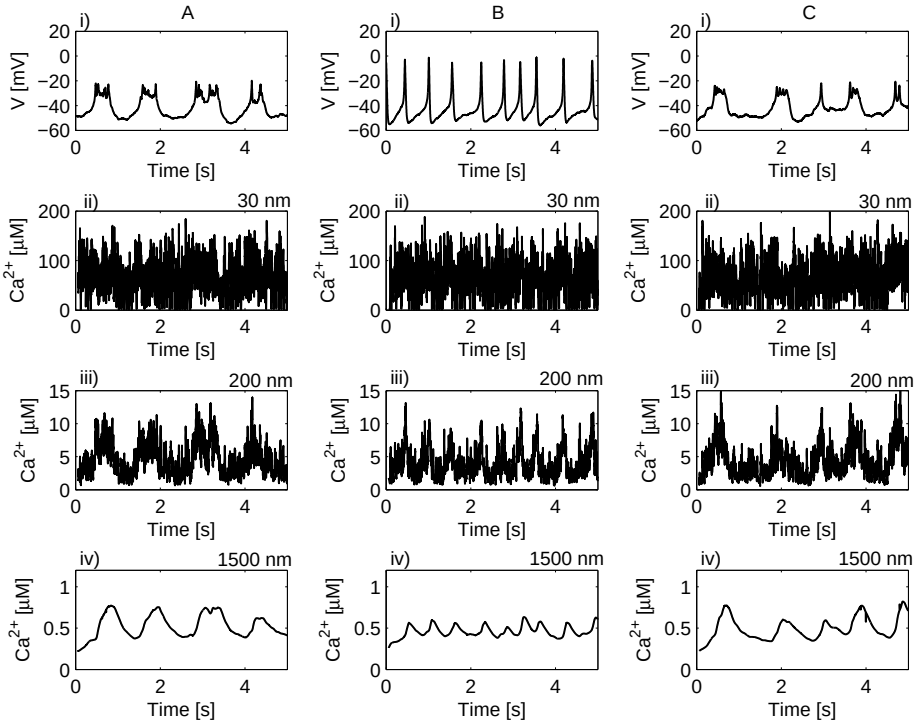

Figure 4.4.8: Ca^{2+} concentration at different distances from a stochastic Ca^{2+} channel on the surface of a conical region (average of 10 independent trials). The Ca^{2+} channel is placed at the center of the cone base with radius 1.5 μm. (A) Bursting profile in control condition. (B) Spiking profile in the presence of the BK channel blocker iberiotoxin. (C) Bursting profile in the presence of iberiotoxin and when BK current is injected back using the dynamic clamp. Sub panels show the experimentally recorded voltage profile (i), and simulated Ca^{2+} concentrations at 30 nm (ii), 200 nm (iii), or 1500 nm (iv) from the channel.

bursting is more efficient farther from the channel (Fig.4.4.10). The fact that bursting is less superior to spiking after normalizing to Ca^{2+} influx compared to the previous simulations of exocytosis using the traces from a gonadotroph (Figs. 4.4.1 and [81] can be explained by noticing that, for this example, iberiotoxin-induced spiking (Fig. 4.4.8B) occurs at a much higher rate than bursting (Fig. 4.4.8A, C). Thus, the dynamics of Ca^{2+} entry is important for the control of exocytosis in addition to the number of Ca^{2+} ions entering the cell.

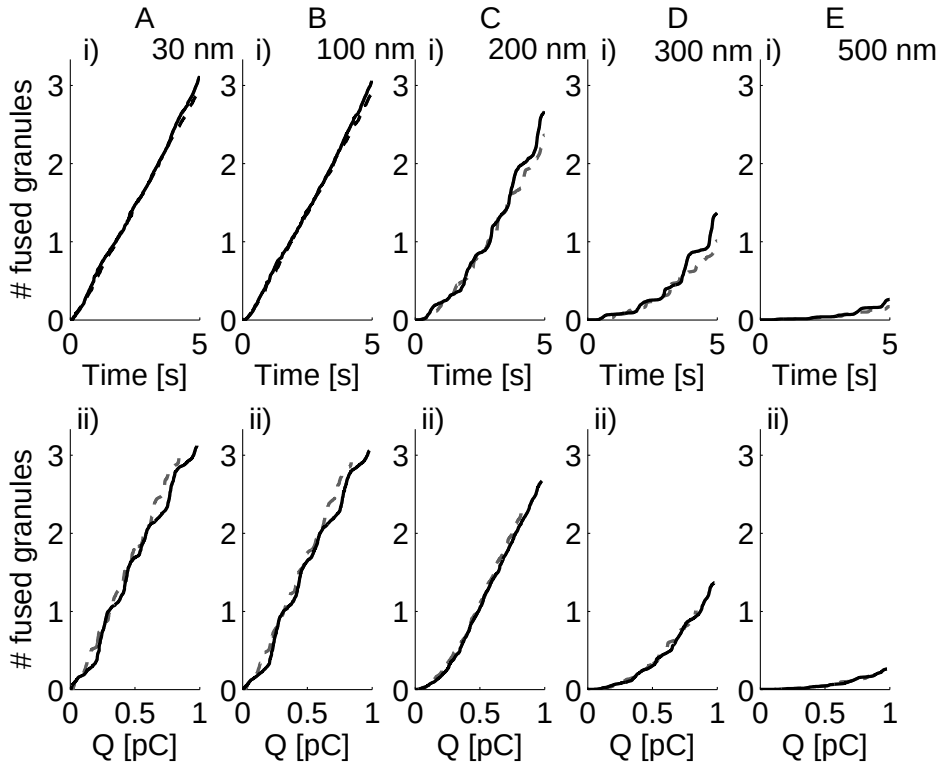

Figure 4.4.9: Single channel exocytosis simulation results with all the pools initially empty for dynamic clamp-induced bursting. Top panels (i) show the number of fused granules as a function of time, evoked by a spiking voltage trace (gray dashed curves) and bursting induced by dynamic clamp in the presence of iberiotoxin (black solid curves). Bottom panels (ii) show the cumulative number of fused granules during 5 seconds of simulation as a function of the cumulative Ca^{2+} entry Q. (A) granules located at 30 nm, (B) 100 nm, (C) 200 nm, (D) 300 nm, or (E) 500 nm from the channel.

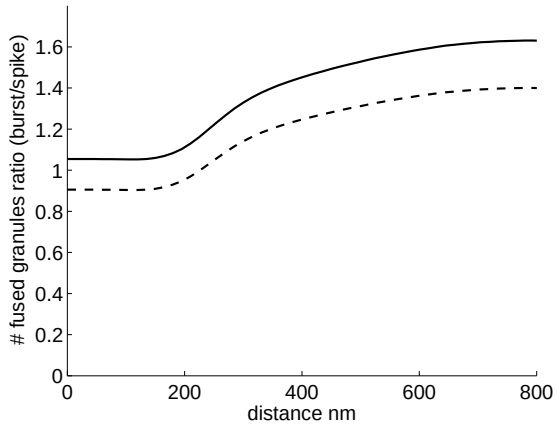

Figure 4.4.10: Summary of exocytosis simulation results with all the pools initially empty during BK-current block and dynamic clamp. The ratios of the total number of fused granules between bursting that results from dynamic clamp application with iberiotoxin vs. spiking that results from iberiotoxin alone (solid black curve). The ratios of the total number of fused granules normalized to the charge entry Q are given by the dashed curves.

4.5 Discussion

In the absence of hypothalamic stimulation or inhibition, pituitary lactotrophs and somatotrophs release prolactin and growth hormone, while gonadotrophs comparatively secrete a negligible amount of luteinizing hormone. This difference in basal hormone release was matched by differences in spontaneous electrical activity between these cell types: lactotrophs and somatotrophs often exhibit "pseudo-plateau" bursts of activity, causing periodic Ca^{2+} influx, while gonadotrophs usually produce spikes that are too brief to perturb the bulk Ca^{2+} level substantially [61]. Such differences in the bulk Ca^{2+} profiles lead to the the hypothesis that different patterns of spontaneous electrical activity result in different rates of hormone release: bursting causes hormone release from lactotrophs and somatotrophs, while spiking causes no hormone release from gonadotrophs.

We tested this hypothesis in this paper. While Ca^{2+} triggers hormone release and bursting creates larger amplitude oscillations of average in-

tracellular Ca^{2+} than spiking, this does not necessarily mean that bursting is more effective at triggering hormone release. The Ca^{2+} concentration that matters is that seen by the hormone-containing granules at their release sites, and if the release sites are close to Ca^{2+} channels, the high Ca^{2+} concentration in the microdomains around the channels created by a single spike may be just as effective as that due to a burst in triggering fusion of granules. Indeed, we found that spiking is as effective as bursting in releasing a full pool of primed granules, as long as the release site is within 100 nm from the channel (Fig. 4.4.2). However, if the primed pool of granules is initially empty, or if the release site is located more than 100 nm from the channel, we found that bursting was always more effective than spiking in triggering granule fusion.

There are two mechanisms for this difference between bursting and spiking. The first results from the larger entry of Ca^{2+} caused by bursting over spiking. Because the fraction of open Ca^{2+} channels is increased for a longer period of time during a burst than during a spike, a burst causes a larger increase in bulk Ca^{2+}. Since the replenishment of the primed pool of granules depends on bulk Ca^{2+}, bursting causes a higher rate of granules priming, which in turn results in a higher rate of granule fusion. This effect is independent of the microdomain Ca^{2+} concentration, so bursting causes a higher rate of granule fusions even if the release site is 100 nm or less from the channel (Fig. 4.4.3 top panels). However, this mechanism relies on the fact that, at similar event frequency, bursting means that the electric potential across the cell membrane stays high (i.e., at levels where the cell Ca^{2+} current is high) for a larger fraction of time than spiking. If spiking frequency is increased relative to bursting frequency so that the total amount of active time is the same, then bulk Ca^{2+} will be similar and so will the priming rate. In that sense, the bursting pattern is not more effective than the spiking pattern if the amount of activity (and therefore Ca^{2+} entry) is normalized.

Nevertheless, there is a second mechanism that makes bursting more effective than spiking at triggering granule fusion, even if we normalize by the total amount of Ca^{2+} entry. Because three free Ca^{2+} ions must bind

to the release machinery to trigger fusion, fusion is facilitated by a stable high local Ca^{2+} level. This is more likely to happen during bursting than spiking, since Ca^{2+} influx can be maintained longer during a burst than during a spike. This advantage of bursting can be observed when the release site is more than 100 nm away from the channel (Fig. 4.4.3 bottom panels). Cells must quickly restore intracellular Ca^{2+} to low levels using ATP-driven pumps, so there is an energetic cost associated with the entry of each Ca^{2+} ion. For release sites far from the Ca^{2+} channels, the bursting pattern of activity results in a more efficient use of Ca^{2+} ions than the spiking pattern.

This may not be true at higher spike frequencies. If we increase spike frequency the interval between each increase in local Ca^{2+} goes down, so the higher effectiveness of bursting might only be observed for release sites further away from the channels. We see that for the BK (endogenous or injected by dynamic clamp) vs. no BK (i.e., in the presense of iberiotoxin) case, where the maximum Ca^{2+} concentration reached at 200 nm (Fig. 4.4.8) is similar to what we saw in Fig. 4.4.1, but the interspike interval is lower so Ca^{2+} does not go back down for long – in that case spiking is at least as efficient as bursting in evoking release, for release sites up to 500 nm away from the channels (Fig. 4.4.9). Nevertheless, the bursting pattern caused by the presence of a BK current evoked more granule fusion because of the high average bulk Ca^{2+} during bursting, which results in higher rate of replenishment of the primed granules.

There are many examples in endocrinology where the pattern of a signal plays an important role. A well-known example is that the frequency of hypothalamic gonadotropin-releasing hormone pulses determines the differential release of luteinizing and follicle-stimulating hormone by gonadotrophs [89]. Here we used a hybrid experimental/modeling approach to show that the actual pattern of electrical activity can trigger different rates of hormone release. Since the discovery that pituitary cells are electrically active 40 years ago, researchers have wondered how pituitary cells tune electrical activity to regulate hormone release [90]. It has been argued that since hypothalamic factors act on a number of ion

channels on pituitary cell membranes, electrical activity provides numerous ways for the hypothalamus to modulate pituitary hormone release. Some of these factors may even modulate the time constant of BK channels to switch the electrical activity pattern from spiking to bursting [81]. The present work shows that this switch to bursting may improve the effect of hypothalamic stimulating neurohormones in increasing pituitary hormone secretion. In summary, our modeling results show that bursting is superior to spiking in evoking pituitary hormone release, since it brings more Ca^{2+} into the cell, thus augmenting both local and global Ca^{2+} levels, which in turn increases resupply of secretory granules and exocytosis. We found further that channel clustering is advantageous to isolated channels in controlling secretion. Our results have implications beyond pituitary secretion. For example, human pancreatic beta-cells show rapid bursting resembling pituitary plateau bursting [57, 91], which has been suggested to be advantageous for insulin secretion [79]. Further, Ca^{2+} channel clustering in beta-cells has been suggested to be important for insulin exocytosis [85].

5

Spatio-temporal model of L-cell and GLP-1 secretion

A variety of specialized cells are involved in the control of body weight and blood glucose levels because of their role in glucose sensing. The impairment of the glucose-sensing machinery may lead to the development of obesity and diabetes. Pancreatic α-cells and β-cells are the main glucose-sensing specialized cells and they are responsible for the secretion of glucagon and insulin, respectively. Furthermore, the gut plays a pivotal role in nutrient absorption and glucose sensing following a meal [8]. Indeed, peptides secreted by specialized gut cells have profound and sustained physiological effects on appetite and insulin release. Intestinal L-cells are a subset of such specialized cells located along the ingestive tract with the capability of sensing the presence of nutrients in the lumen and of transforming this information into a stimulation of GLP-1 secretion.

In light of the close connection between metabolic disease and the glucose-sensing pathways, in this Chapter we address the aim to investigate glucose-sensing mechanisms coupled to GLP-1 secretion in such enteroendocrine L-cells. One of the intestinal L-cells' role, as already introduced in Chapter 1, is to secrete GLP-1 incretin hormone in response to food intake. This hormone amplifies insulin secretion when glucose is orally administrated. Moreover, it inhibits glucagon secretion, slows gastric emptying, regulates appetite and food intake, stimulates β-cells neogenesis and proliferation, and inhibits apoptosis of β-cells [4].

GLP-1 secretion has clinical relevance in the development and treatment of type 2 diabetes. Reduction or even completely loss of GLP-1 secretion induce a drop in incretin effect [4]. The development of new therapeutic strategies to increase the endogenous GLP-1 secretion makes the study of the GLP-1 secretion pathways of growing interest [92, 93].

The molecular pathways of the glucose-sensing cells underlying secretion are different. In β-cells glucose is transported inside the cell by the GLUT2 transporter inducing glucose metabolism and subsequent closure of the ATP-sensitive potassium (K(ATP)) channels. Closure of the channels leads to cell depolarization and insulin release [94]. In enteroendocrine L-cells, preliminary studies with the GLP-1 secretory GLUTag cell line [95] suggested that glucose-sensing mechanism could involve the classical glucose-sensing machinery found in pancreatic β-cells. However, recent studies [93] revealed that, in addition to GLUT2 transporter, another glucose-sensing mechanism can be found in this type of cells: SGLT1 transporters link glucose stimulus to electrical activity and hormone secretion. In the same way, SGLTs are involved in hypothalamic glucose sensing [96]. SGLT1 transporters generate a small depolarizing current sufficient to trigger electrical activity promoting Ca^{2+} influx and release of GLP-1 [97]. There is evidence that GLUTag and primary L-cells show differences in the electrophysiological properties [98, 99] resulting in differences in the secretory responses. Indeed, while GLUTag cells seem to use both GLUT2 and SGLT to transduce glucose sensing to GLP-1 secretion, primary L-cells exploit SGLT1 [97, 100–102].

Another key point to take into account when the role of SGLT1 and GLUT2 in glucose sensing is evaluated is the spatially location of the two transporters. GLUT2 is predominantly located on the basolateral side of L-cells, while SGLT1 is located in the apical side [101]. With the aim of evaluating the SGLT1 role in the apical membrane in contrast to GLUT2 transport at the basolateral membrane in evoking GLP-1 secretion, experiments in a physiological setting should be performed, but this is still technically challenging. This kind of experiments would require simultaneous measurements of electrical activity, calcium dynamics and release from single L-cells without altering/changing the cell polarity. Recent studies on isolated primary L-cells stimulated with glucose [97, 102] have demonstrated that in presence of phloretin, a GLUT2 transporter blocker, GLP-1 secretion is only slightly reduced, suggesting that a reduction of glucose metabolism is not fundamental to evoke GLP-1 secretion. On the other hand, in presence of phloridzin, a SGLT1 transporter blocker, and subject to the same glucose conditions, GLP1 secretion is substantially reduced, supporting the idea that this electrogenic transporter has a main role in GLP-1 secretion. In contrast, glucose concentration detected inside the cells with phloridzin is hardly reduced while it is drastically diminished [97] with phloretin. Nevertheless, these experiments were done on isolated cell with lost depolarization.

In the absence of experimental data obtained from L-cells *in situ*, a deeper insight into the stimulus-secretion pathways could be achieved by means of a mathematical model. A spatio-temporal model that combines electrical activity, glucose transportation and metabolism as well as GLP-1 secretion and take into account the spatial configuration of the cell has not yet been developed. Therefore, in this Chapter we develop a spatio-temporal mathematical model of a single L-cell, starting from a model of the electrical activity of primary L-cells [103], and computer simulations are used to better understand the glucose-sensing mechanisms and the relative roles of SGLT1 and GLUT2 transport underlying GLP-1 secretion. We model glucose transportation through SGLT1 in the apical side as well as GLUT2 in the basolateral, and glucose diffusion

inside the cell. Furthermore, the subsequent depolarization in response to glucose transportation and metabolism, and the Ca^{2+} influx due to voltage-dependent Ca^{2+} channel opening, is simulated and coupled to a simple model of GLP-1 secretion. We validate the model by simulating the setting of the experiments conducted in [97, 102] and we find, in compliance with their results, that glucose transportation inside the cell through SGLT1 transporter induces Ca^{2+} influx and release of GLP-1 thanks to depolarization, while glucose metabolism alone is not sufficient to evoke depolarization, resulting in lower GLP-1 secretion, and suggesting a marginal role of GLUT2 for GLP-1 secretion. The spatio-temporal model is further exploited to investigate the glucose-dependent contribution on GLP-1 secretion. In general, this first spatial-temporal model allows us to simulate relevant physiological settings that are still not experimentally feasible without alteration of the cell polarization.

5.1 Electrical Activity Model

The electrical activity of primary L-cells is modeled as in [103] with a Hodgking-Huxley-type model based on patch clamp data from primary colonic L-cells. The model consists of ATP-sensitive K(ATP)-channels, voltage-gated Na^+-, K^+- and Ca^{2+}-channels, and the electrogenic sodium glucose co-transporter SGLT1. The membrane potential evolves in time according to:

$$\frac{dV}{dt} = -(I_{Na} + I_{CaT} + I_{CaHVA} + I_{K(ATP)} + I_K + I_{SGLT}). \tag{5.1}$$

Voltage-gated membrane currents are modeled as

$$I_X = g_X m_X h_X (V - V_X), \tag{5.2}$$

where X stands for the channel type, V_X is the associated reversal potential and g_X is the maximal whole-cell channel conductance, while m_X stands for channel activation and h_X stands for inactivation. Activation,

and similarly inactivation, is described by:

$$\frac{dm}{dt} = \frac{m_{X,\infty}(V) - m_X}{\tau_{mX}}, \tag{5.3}$$

where $m_{X,\infty}$ is the steady-state voltage-dependent activation function, and τ_{mX} is the time-constant of activation which in some cases depends on the membrane voltage. The steady-state voltage-dependent activation or inactivation functions were described by the Boltzmann equation:

$$m_{X,\infty} = \frac{1}{1 + e^{(V - V_{mX}/k_{mX})}}. \tag{5.4}$$

As modeled in [103], Na^+ currents are supposed to activate instantaneously and to have a fast inactivation kinetic estimated by simulating voltage clamp experiments [99].

Ca^{2+}- currents are divided into low-(T-type, I_{CaT}) and high-(L-and Q-type, I_{CaHVA}) voltage-activated Ca^{2+} currents. An instantaneous activation of the Ca^{2+}-currents is assumed. The T-type Ca^{2+}-channels are assumed to inactivate completely. L-and Q-type inactivation function is modeled as [103]

$$h_{CaHVA,\infty} = (1 - A) + A h^*_{CaHVA,\infty} \tag{5.5}$$

K^+-channels [103] are assumed not to inactivate and to activate with kinetics modeled as

$$\tau_{mKv} = \tau_0 + \frac{\tau_1}{1 + e^{(V + V_\tau)/k_\tau}}, \tag{5.6}$$

with all the parameters taken from [103] and reported in Table 5.1.2.

The ATP-sensitive potassium (K(ATP))-current is modeled as:

$$I_{K(ATP)} = g_{K(ATP)}(V - V_K), \tag{5.7}$$

where $g_{K(ATP)}$ is whole cell conductance of the ATP-sensitive potassium

Parameter	Value [mM]
$[MgADP^-]_i$	$0.55 \cdot 0.3\,[ADP]_i$
$[ADP^{3-}]_i$	$0.45 \cdot 0.3\,[ADP]_i$
$[ATP^{4-}]_i$	$0.05 \cdot [ATP]_i$
K_{dd}	17
K_{td}	26
K_{tt}	1

Table 5.1.1: Parameters of the adenine nucleotide concentration and dissociation constants.

channels and depends on the fraction of open channels:

$$g_{K(ATP)} = \bar{g}_{K(ATP)} O_{K(ATP)}, \tag{5.8}$$

with $\bar{g}_{K(ATP)}$ denoting the maximal value of the conductance. The fraction of open channels $O_{K(ATP)}$ depends on the nucleotide concentration according to [104]:

$$O_{K(ATP)} = \frac{0.08\big(1 + \frac{2[MgADP^-]_i}{K_{dd}}\big) + 0.89\big(1 + \frac{[MgADP^-]_i}{K_{dd}}\big)^2}{\big(1 + \frac{[MgADP^-]_i}{K_{dd}}\big)^2\big(1 + \frac{[ADP^{3-}]_i}{K_{td}} + \frac{[ATP^{4-}]_i}{K_t t}\big)}. \tag{5.9}$$

K_{dd}, K_{td}, K_{tt}, are the dissociation constants that describe the binding equilibrium of the various nucleotide forms, $[MgADP^-]_i$, $[ADP^{3-}]_i$, $[ATP^{4-}]_i$ are cytosolic nucleotide concentrations that depend on fixed fractional values of the total $[ADP]_i$ and $[ATP]_i$ concentrations. Table 5.1.1 summarizes the values used as in [104]. Since we included in the model the $[ATP]_i$ production obtained by glycolysis and in order to eliminate $[ADP]_i$ as a variable, we use the assumption that $[ATP]_i + [ADP]_i$=5 mM.

SODIUM/GLUCOSE CO-TRANSPORTER MODEL

As said in Chapter 2, the sodium/glucose co-transporter (SGLT1) transport the glucose from the intestine into the L-cells by means of concentration gradient of Na^+. In particular two Na^+ ions are required to transport

one molecule of glucose into the cell and in absence of Na^+ there is no glucose transportation. The model [25] of the transporter consists of six-states (Fig. 5.1.1). In the first state the carrier is empty, then two sodium ions bind to the carrier (state 2) and consequentially one molecule of glucose associates to the carrier, as well (state 3). The carrier then translocates from outside to inside the cell. The same steps take place symmetrically inside the cell leading to sodium and glucose dissociation. Finally, the empty carrier is brought back to the initial state outside the cell.

$$\frac{dC_1}{dt} = (k_{21}C_2 + k_{61}C_6) - (k_{12} + k_{16})C_1, \tag{5.10}$$

$$\frac{dC_2}{dt} = (k_{12}C_1 + k_{32}C_3 + k_{52}C_5) - (k_{21} + k_{23} + k_{25})C_2, \tag{5.11}$$

$$\frac{dC_3}{dt} = (k_{23}C_2 + k_{43}C_4) - (k_{32} + k_{34})C_3, \tag{5.12}$$

$$\frac{dC_4}{dt} = (k_{34}C_3 + k_{54}C_5) - (k_{45} + k_{43}C_4), \tag{5.13}$$

$$\frac{dC_5}{dt} = (k_{45}C_4 + k_{65}C_6 + k_{25}C_2) - (k_{54} + k_{52} + k_{56})C_5, \tag{5.14}$$

$$\frac{dC_6}{dt} = (k_{16}C_1 + k_{56}C_5) - (k_{61} + k_{65})C_6, \tag{5.15}$$

The values of the rate constants are set as in [25] and given in Table 5.1.3.

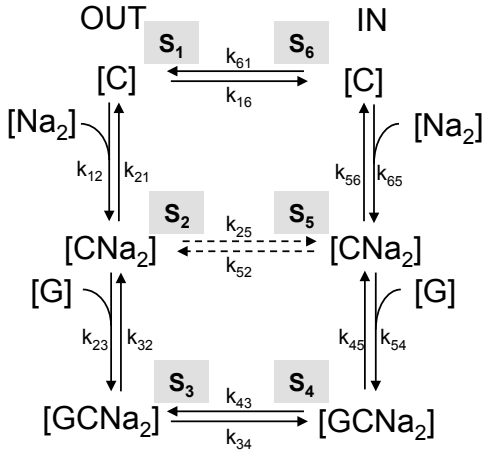

Figure 5.1.1: Six-state model of SGLT1 transporter.

By defining:

$$k_{12} = k_{12}^0 [Na]_{out}^2 e^{-\alpha\mu}, \tag{5.16}$$

$$k_{21} = k_{21}^0 e^{\alpha\mu}, \tag{5.17}$$

$$k_{16} = k_{16}^0 e^{\delta\mu}, \tag{5.18}$$

$$k_{61} = k_{61}^0 e^{-\delta\mu}, \tag{5.19}$$

$$k_{23} = k_{23}^0 [G]_{out}, \tag{5.20}$$

$$k_{45} = k_{45}^0 [G]_{in}, \tag{5.21}$$

$$k_{56} = k_{56}^0 [Na]_{in}^2, \tag{5.22}$$

where $[Na]_{out}$ and $[G]_{out}$ are the external Na^+ and glucose concentration (at the lumen), respectively, while $[Na]_{in}$ and $[G]_{in}$ are the Na^+ and glucose concentration inside the cell at the inside of the apical membrane, respectively. Furthermore, μ is the reduced potential FV/RT, where R is the gas constant and T is the temperature. The carriers are negatively charged and during the sodium/glucose co-transportation, they generates a current that is given by:

$$I_{SGLT} = -\frac{2F}{C}\frac{n}{N_A}[\alpha(k_{12}C_1 - k_{21}C_2) + \delta(k_{61}C_6 - k_{16}C_1)], \tag{5.23}$$

where F is the Faraday constant, C the cell capacitance, n the number of transporters, N_A the Avogadro's number, k_{xy} is the rate constant describing the transition between state x and y, C_z is the fraction of carriers in state z, and α and δ are phenomenological coefficients representing fractional dielectric distances.

The SGLT current (5.23) depends both on the membrane voltage V, due to the rate constants dependence on it, and on glucose and sodium concentrations inside and outside the cell. The magnitude of SGLT currents increases proportionally to the number of transporters n in the cell. For the primary murine L-cells, which have cell capacitance $C \sim 8$ pF [99], n is set to 4×10^6 [103].

Parameter	Value	Unit
	Sodium channels	
V_{Na}	69	mV
g_{Na}	2.1	nS/pF
V_{mNa}	-19	mV
k_{mNa}	-5	mV
V_{hNa}	-46	mV
k_{hNa}	6	mV
τ_{hNa}	3	ms
	Calcium channels	
V_{Ca}	65	mV
g_{CaHVA}	0.29	nS/pF
V_{mCaHVA}	-5	mV
k_{mCaHVA}	-6	mV
V_{hCaHVA}	-23	mV
k_{hCaHVA}	13	mV
τ_{hCaHVA}	100	ms
A	0.38	ms
g_{CaT}	0.075	nS/pF
V_{mCaT}	-40	mV
k_{mCaT}	-7	mV
V_{hCaT}	62	mV
k_{hCaT}	20	mV
τ_{hCaT}	20	ms
	Potassium channels	
V_K	-70	mV
g_K	2.5	nS/pF
V_{mK}	5.2	mV
k_{mK}	-15	mV
τ_0	30	ms
τ_1	40	ms
V_τ	20	mV
k_τ	5	mV
$g_{K(ATP)}$	0.001	nS/pF

Table 5.1.2: Default parameters of the different ion channels.

Parameter	Value	Unit
n	4e6	adim
C	8	pF
k_{12}^0	8e-5	$\mathrm{ms}^{-1}\mathrm{mM}^{-2}$
k_{21}^0	0.5	ms^{-1}
α	0.3	adim
k_{23}^0	0.1	$\mathrm{ms}^{-1}\mathrm{mM}^{-1}$
k_{32}	0.02	ms^{-1}
k_{25}	3e-4	ms^{-1}
k_{52}	3e-4	ms^{-1}
k_{34}	0.05	ms^{-1}
k_{43}	0.05	ms^{-1}
k_{45}^0	0.8	ms^{-1}
k_{54}	1.2e-03	$\mathrm{ms}^{-1}\mathrm{mM}^{-1}$
k_{56}^0	0.01	ms^{-1}
k_{65}	5e-8	$\mathrm{ms}^{-1}\mathrm{mM}^{-2}$
k_{16}^0	0.035	ms^{-1}
k_{61}^0	5e-3	ms^{-1}
k_{61}^0	5e-3	ms^{-1}
δ	0.7	adim

Table 5.1.3: Default parameters of the SGLT1 model

5.2 Mathematical Spatial Modeling

The spatial organization of L-cells is modeled by a series of partial differential equations. The cell is represented by a cylinder with length 28 μm and base radius of 2.8 μm [105–107] (Fig. 5.2.1 and Fig. 5.2.2). Because of this cylindrical geometry, the full 3-dimensional problem is reduced to a 1-dimensional problem by considering the concentration uniform in tubular cross-sections:

$$\frac{\partial c}{\partial t} = D\frac{\partial^2 c}{\partial x^2} + f(x,t,z), \tag{5.24}$$

where c is a general species, D is the diffusion coefficient of the species, x is the spatial variable along which the diffusion is considered and $f(x,t,z)$ is the production-destruction rate per unit of volume for each location x and time t and $z = (c_1, c_2, ...c_k)$. The numerical solution to the one dimensional reaction-diffusion partial differential equation is achieved by the method of lines. The spatial domain ($0 < x < 28$ μm) is subdivided into $N = 28$ equal intervals, with $\Delta x = 28/N = 1$ μm as the length of each interval. By recalling the definition of partial derivative of c,

$$\frac{\partial c}{\partial x} = \lim_{\Delta x \to 0} \frac{c(x+\Delta x, t) - c(x,t)}{\Delta x}, \tag{5.25}$$

if Δx is small, but not zero, we have an approximation to the partial derivative:

$$\frac{\partial c(x,t)}{\partial x} \approx \frac{c(x+\Delta x, t) - c(x,t)}{\Delta x}. \tag{5.26}$$

Similarly, the second partial derivative can be found with Δx small but not zero:

$$\frac{\partial^2 c(x,t)}{\partial^2 x} \approx \frac{c(x+\Delta x, t) - 2c(x,t) + c(x-\Delta x, t)}{\Delta x^2}. \tag{5.27}$$

Using this approximation at each spatial interior grid point, it is possible to obtained a set of ordinary differential equations:

$$\frac{\partial c(x,t)}{\partial t} = \frac{D}{\Delta x^2}(c(x+\Delta x,t) - 2c(x,t) + c(x-\Delta x,t)) + f(x,t,z). \quad (5.28)$$

The initial conditions are the same of the partial differential equation. Regarding the boundary conditions, for $x = 0$ and $x = N$, we invoke the no-flux boundary conditions at the sides of the cell unless the presence of a source or a sink, obtaining:

$$\frac{\partial c(0,t)}{\partial t} = \frac{D}{\Delta x^2}(c(\Delta x,t) - c(0,t)) + f(0,t,z), \quad (5.29)$$

$$\frac{\partial c(N,t)}{\partial t} = \frac{D}{\Delta x^2}(c(N-\Delta x,t) - c(N,t)) + f(N,t,z). \quad (5.30)$$

Parameters for spatial modeling are given in Table 5.2.1. All fluxes are given in unit mM/ms, currents in pA and diffusion coefficients in μm^2/ms.

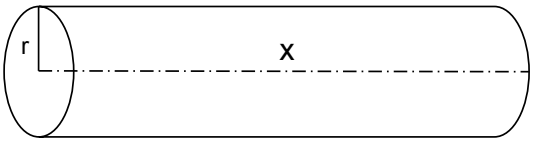

Figure 5.2.1: Geometrical representation of L-cell.

GLUCOSE

The reaction-diffusion equation for the glucose concentration is:

$$\frac{\partial [G](x,t)}{\partial t} = D_G \frac{\partial^2 [G](x,t)}{\partial x^2} + J_{G_{SGLT}}\delta(x,t) + J_{G_{GLUT2}}\delta(x-L,t) - J_{G_{util}}(x,t), \quad (5.31)$$

We choose D_G=0.6 μm^2/ms [108], and $\delta(x-L,t)$ is the Dirac delta function centered in $x = L$ and $\delta(x,t)$ is the Dirac delta function centered in $x = 0$. The first term of all the reaction-diffusion equation is implemented

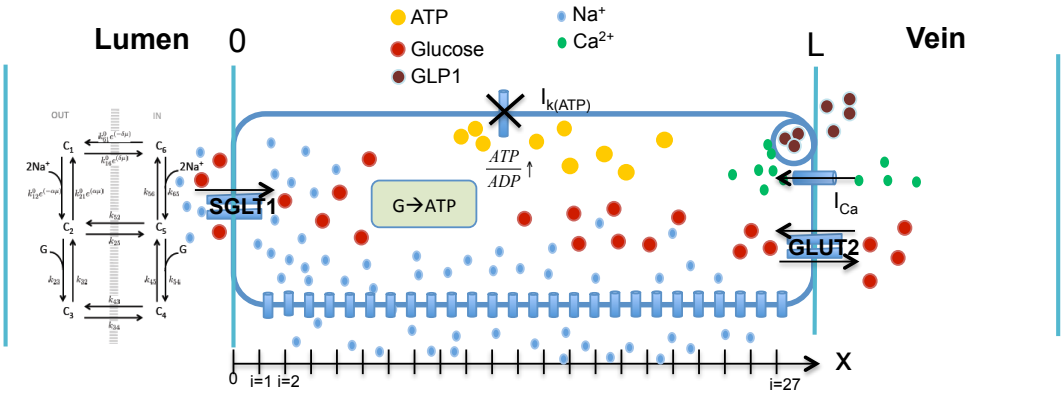

Figure 5.2.2: Schematic representation of the spatial model. Glucose in the lumen is transported into or out of the cell by SGLT transporter, while at the vein side glucose can be transported into the cell by the facilitated diffusion transporter GLUT2. Voltage-gated Ca^{2+} channels are located at the basolateral side of the cell along with GLP-1-containing granules ready for fusion. Na^{+} channels are arranged along the cell length.

by the method of lines, using (5.27).

$$\frac{dG_0}{dt} = \frac{D_G}{\Delta x^2}(G_1 - G_0) + f(z, 0, t), \tag{5.32}$$

$$\frac{dG_i}{dt} = \frac{D_G}{\Delta x^2}(G_{i+1} - 2G_i + G_{i-1}) + f(z, i, t), \qquad i = 1, .., 27 \tag{5.33}$$

$$\frac{dG_{28}}{dt} = \frac{D_G}{\Delta x^2}(G_{27} - G_{28}) + f(z, 28, t). \tag{5.34}$$

The sodium/glucose co-transporter is placed at the apical side [101] of the cell and it transports glucose from the lumen into the cell according to:

$$J_{G_{SGLT}} = \frac{n}{N_A V_i}(k_{45}C_4 - k_{54}^0 C_5 G_0), \tag{5.35}$$

where G_0 is the glucose concentration inside the cell in the volume unit close to the transporter (Fig 5.1), V_i is the volume unit, and $J_{G_{SGLT}}$ is the glucose flux. The GLUT2 transporter is located at the basolateral side of the cell and it is modeled as a facilitated diffusion transporter. Glucose influx and efflux from/into the vein takes place according to the concen-

tration gradient:

$$J_{G_{GLUT2}} = K_{G_{GLUT2}}([G]_{ext} - G_{28}), \tag{5.36}$$

where $K_{G_{GLUT2}}$ is the uptake rate. We chose $K_{G_{GLUT2}}$=1.1e-3 ms^{-1} in order to maintain a ratio between glucose utilization and rate transportation of $\sim$ 20, as found in [109]. $[G]_{ext}$ is the glucose concentration in the vein and G_{28} denotes the glucose concentration inside the cell in the volume in proximity of the GLUT2 transporter (i=28 in Fig 5.2.2). Glucose phosphorylation inside the cell is mainly performed by glucokinase (GK) [106, 110, 111]. The flux-concentration curve of GK is slightly sigmoidal, and glucose utilization $J_{G_{util}}$ is modeled with a Hill equation [112]:

$$J_{G_{util}} = \frac{V_{GK}([G]/S_{0.5}^{GK})^{h_{GK}}}{1 + ([G]/S_{0.5}^{GK})^{h_{GK}}} \tag{5.37}$$

where $S_{0.5}^{GK}$ is the half-activation point of GK with respect to glucose, and h_{GK} is the Hill coefficient. V_{GK} is equal to 5.56e-5 mM/ms, h_{GK} equal to 1.7 and $S_{0.5}^{GK}$ equal to 8 mM [57] (Table 5.2.1). Indeed,

ATP

The time-spatial ATP model is given by:

$$\frac{\partial [ATP](x,t)}{\partial t} = D_{ATP}\frac{\partial^2 [ATP](x,t)}{\partial x^2} + J_{ATP_{prod}}(x,t) - J_{ATP_{util}}(x,t), \tag{5.38}$$

where D_{ATP}=0.5 μm^2/ms [113]. When a glucose molecule proceeds through glycolysis and the Krebs cycle, the free energy that is created is used to generate ATP. It is known that for each single glucose molecule consumed, 31 ATP molecules are produced [113]. As a consequence, the ATP flux production (mM/ms) is modeled as

$$J_{ATP_{prod}} = 31 J_{G_{util}}, \tag{5.39}$$

while ATP utilization is modeled as Hill equation similarly to glucose utilization,

$$J_{ATP_{util}} = \frac{V_{ATP}([ATP]/S_{0.5}^{ATP})}{1 + ([ATP]/S_{0.5}^{ATP})}, \tag{5.40}$$

where V_{ATP} is the maximal rate of utilization, $S_{0.5}^{ATP}$ is the half activation point and it is hypothesized equal to 2 mM.

CALCIUM

Voltage-dependent Ca^{2+} channels are supposed to be placed on the basolateral side of the cell, where GLP-1 exocytosis occurs [114]. Ca^{2+} enters through the channels and diffuses inside the cell according to:

$$\begin{aligned}\frac{\partial[Ca^{2+}](x,t)}{\partial t} = D_{Ca}\frac{\partial^2[Ca^{2+}](x,t)}{\partial x^2} + f_i\big(J_{Ca}\delta(x-L,t) \\ - J_{SERCA}(x,t) - J_{PMCA}\delta(x-L,t) + J_{leak}(x,t)\big),\end{aligned} \tag{5.41}$$

where D_{Ca} is the effective diffusion coefficient for Ca^{2+} and f_i is ratio of free-to-total Ca^{2+}. We choose D_{Ca}=0.2 μm^2 ms^{-1} according to [72]. The second term in (5.41) represents Ca^{2+} influx, and is in its discretized form

$$J_{Ca} = \frac{1}{2FV_i}I_{Ca}(t), \tag{5.42}$$

where F is Faraday's constant, $I_{Ca}(t)$ is the (inward) calcium current and V_i is the volume unit. J_{SERCA} is the SERCA pump Ca^{2+} uptake. The SERCA activity is modeled with a Hill equation [57]

$$J_{SERCA} = J_{SERCA,max}\frac{[Ca^{2+}]^2}{(K_{SERCA}^2 + [Ca^{2+}]^2)}. \tag{5.43}$$

The pump is assumed to act in each spatial point. Similarly, the flux across the membrane through the PMCA pump, J_{PMCA}, is in its discretized form modeled as [57]:

$$J_{PMCA} = (V_{cyt}/V_i)J_{PMCA,max}\frac{[Ca^{2+}]}{(K_{PMCA} + [Ca^{2+}])}. \tag{5.44}$$

The pump operates at the plasma membrane on the basolateral side [115], in proximity of the Ca^{2+} channels in the volume unit V_i. J_{leak} represents the ER Ca^{2+} release flux.

SODIUM

Sodium influx occurs through both the SGLT1 transporter and the Na^+ channels. We located the channels along the cell as shown in Fig. 5.2.2. The Na^+ reaction-diffusion equation is given by:

$$\begin{aligned}\frac{\partial [Na^+](x,t)}{\partial t} = D_{Na}\frac{\partial^2 [Na^{2+}](x,t)}{\partial x^2} + J_{Na}(x,t) \\ - J_{Na_{SGLT}}\delta(x,t) - J_{Na_{pump}}(x,t),\end{aligned} \tag{5.45}$$

where D_{Na} is the diffusion coefficient for Na^+. It is set equal to 0.8 μm^2 ms^{-1} according to [116]. Similarly to Ca^{2+} influx, the second term J_{Na} represents Na^+ influx from the Na^+ channels,

$$J_{Na} = \frac{1}{FV_{cyt}} I_{Na}(t), \tag{5.46}$$

with F denoting Faraday's constant, and I_{Na}(t) denoting the (inward) Na^+ current. Na^+ channels are supposed to be spatially located along the length of the cell, and therefore the Na^+ flux in each point is divided by the cell volume, V_{cyt}. $J_{Na_{SGLT}}$ is the Na^+ flux from the lumen associated to the sodium/glucose co-transporter and it is, for the methods of line, given by:

$$J_{Na_{SGLT}} = \frac{n}{N_A V_i}(k_{56}C_5 - k^0_{65}C_6 Na_0^2) \tag{5.47}$$

where Na_0 is the Na^+ concentration inside the cell in the volume unit close to the transporter (i=1 in Fig. 5.1.1), and V_i is the volume of the unit. $J_{Na_{pump}}$ represents the mathematical model of all the mechanisms that are involved in Na^+ efflux, e.g. Na^+/Ca^{2+} and Na^+/K^+ exchangers,

$$J_{Na_{pump}} = k_{Na_{pump}}[Na]. \tag{5.48}$$

Parameter	Value	Unit
L	28	μm
r	2.8	μm
V_i	25e-15	L
V_{cyt}	e-15	mMms^{-1}
f_i	0.05	adim
V_{GK}	5.56e-5	mMms^{-1}
$S_{0.5}^{GK}$	8	mM
h_{GK}	1.7	adim
D_G	0.6	μm^2/ms
$[G]_0$	1	mM
V_{ATP}	4e-4	mMms^{-1}
$S_{0.5}^{ATP}$	2	mM
D_{ATP}	0.5	μm^2/ms
$[ATP]_0$	1	mM
$J_{SERCA,max}$	0.06	μMms^{-1}
$J_{PMCA,max}$	0.04	μMms^{-1}
K_{SERCA}	0.27	μM
K_{PMCA}	0.5	μM
D_{Ca}	0.2	μm^2/ms
$[Ca]_0$	0.5	μM
$k_{Na_{pump}}$	3.8e-04	ms^{-1}
D_{Na}	0.04	μm^2/ms
$[Na]_0$	1	mM

Table 5.2.1: Default parameters of the spatial model.

with $k_{Na_{pump}}$=3.8e-04 ms^{-1} chosen to maintain intracellular Na^+ at steady state.

5.3 GLP-1 Exocytosis Model

A simple basic exocytosis model is coupled to the computed Ca^{2+} and ATP profiles, assuming that that the process involves both an ATP- and Ca^{2+}-dependent fusion rate, according to [97] where glucose-dependent amplification of secretion is seen when GLUTag cell are depolarised by KCl and stimulated with glucose. We use a one-pool model, Fig. 5.3.1,

combining together all the different exocytosis steps and thus focusing only on the resulting fusion rate. The granules are in a single pool representing the ready releasable pool (R_0=100). Granules fuse with the membrane at rate K, which depends both on local Ca^{2+} levels and ATP levels. The local Ca^{2+} and local ATP are determined by solving the reaction diffusion equations (5.38) (5.41) with the method of lines Ca^{2+} and ATP are evaluated in the volume close to the basolateral side, i.e., for i=28. The exocytosis model is described by:

$$\frac{dR}{dt} = R_0 - K(Ca^{2+}_{28}, ATP_{28})R, \tag{5.49}$$

where $K(Ca^{2+}, ATP)$ is given by:

$$K = \left(\frac{k_{max(Ca)}[Ca^{2+}]}{k_{m(Ca)} + [Ca^{2+}]}\right)\left(1 + \frac{k_{max(ATP)}[ATP]}{k_{m(ATP)} + [ATP]}\right) \tag{5.50}$$

where $k_{max(Ca)}$ is the maximal exocytosis rate due to the local Ca^{2+} binding to the granules, $k_{m(Ca)}$ is the Ca^{2+} boundary affinity, $k_{max(ATP)}$ is the maximal amplification of the exocytosis rate due to local ATP, and $k_{m(ATP)}$ is the ATP affinity. All values are given in table 5.3.1.

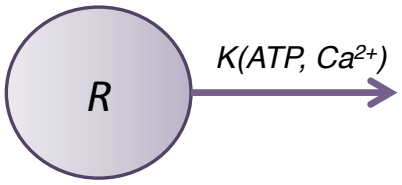

Figure 5.3.1: Kinetic scheme of the exocytosis model. The pool R consists of granules ready for fusion and granules fusion rate (K) depends both on Ca^{2+} concentration and on metabolism (ATP levels).

Parameter	values	Unit
R_0	100	adim
$k_{max(Ca)}$	0.05	μMs$^-1$
$k_{m(Ca)}$	2.7	μM
$k_{max(ATP)}$	5	mMs$^-1$
$k_{m(ATP)}$	2	mM

Table 5.3.1: Default parameters for the exocytosis model.

5.4 Simulation Results

Glucose sensing mechanism

Experiments on primary single L-cells in culture have been conducted in [97]. In these experiments the cells were stimulated with glucose, and the effect of SGLT1/GLUT2 transporter inhibition was studied by measuring glucose concentrations inside the cell as well as GLP-1 secretion. Such experiments were conducted with single cells, where the cell polarization is lost. Therefore, we first use the spatial model to reproduce those experiments but taking into account the cell polarization and trying to understand the cellular mechanisms underlying GLP-1 secretion. In order to mimic the experimental conditions where glucose stimulus is equally given to the whole cell, we stimulate the cell at the apical side in the lumen, where the SGLT1 transporter is located, and at the basolateral side in the vein where the GLUT2 transporter is placed, with 10 mM of glucose. In the first 5 seconds of simulation the cell is in a silent state, therefore lumen glucose concentration ($[G]_{out}$) is 0 mM, and vein blood concentration ($[G]_{ext}$) is at the same concentration of the intracellular glucose concentration (1 mM). The glucose stimulus is given after 5 seconds ($[G]_{out}$=10 mM and $[G]_{ext}$=10 mM). Thus, glucose enters the cell from both sides and it triggers electrical activity and depolarization of the cell (Fig. 5.4.1 black bar indicates glucose stimulus). Spatio-temporal simulation results of intracellular glucose concentration dynamics and mean intracellular glucose concentration are shown in Fig. 5.4.2. After exposure to the stimulus glucose enters the cell from both sides, and the glucose

reaches 4 mM after 10 seconds. Fig. 5.4.2A shows that the glucose uptake rate is higher for the GLUT2 transporter compared to SGLT1 transporter rate since G increases faster at the basolateral (right) end. Cell depolarization induced by the glucose stimulus leads to the voltage-gated Ca^{2+} channels opening and as a consequence to elevation of the intracellular Ca^{2+} concentration. The Ca^{2+} profiles at distances $x = 28, 27, 26$ μm are reported in Fig. 5.4.3. Ca^{2+} concentration reaches 4 μM close to the channel ($x = 28$ μm) with mean values of ~ 1 μM, in agreement with simulation results in pituitary cells in Chapter 4 at the distance of 1 μm. Such Ca^{2+} concentration elevations stimulate release of GLP-1-containing secretory granules.

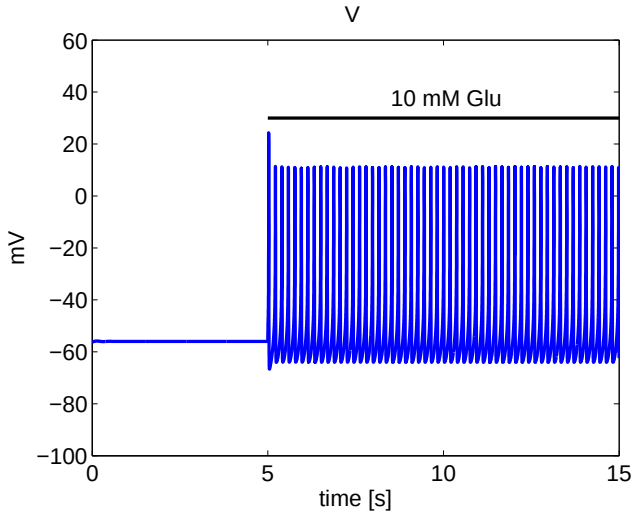

Figure 5.4.1: Simulation of membrane potential with default parameters. SGLT1-substrate concentration $[G]_{out}$ changing from 0 mM (no glucose stimulus) to 10 mM and blood glucose concentration $[G]_{ext}$ changing from 1 mM (in equilibrium with intracellular glucose concentration) to 10 mM.

Role of SGLT1 transporter

In order to investigate the role of SGLT1 in glucose entry and GLP-1 secretion, we reproduce with the model GLUT2 transporter inhibition

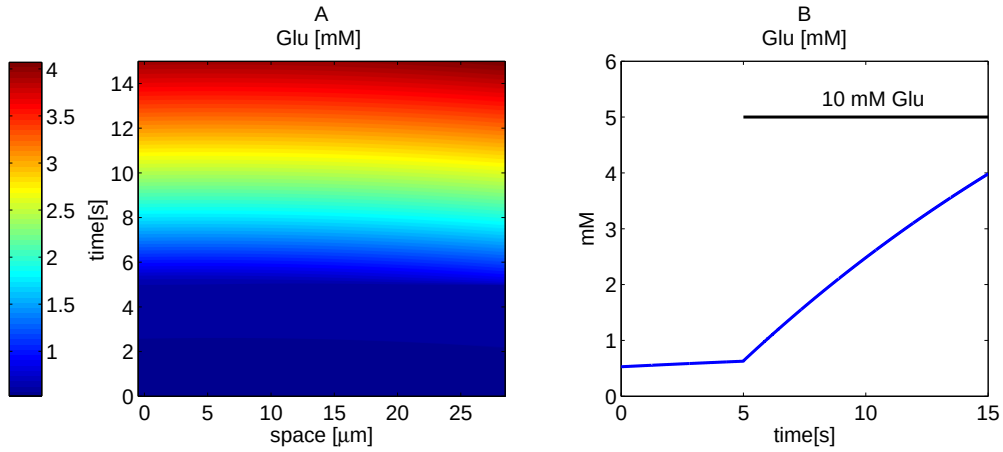

Figure 5.4.2: Simulation of intracellular glucose concentration with default parameters. SGLT1-substrate concentration $[G]_{out}$ changing from 0 mM to 10 mM and blood glucose concentration $[G]_{ext}$ changing from 1 mM to 10 mM. A) intracellular glucose concentration as a function of time and space (color coded in mM). B) Intracellular glucose mean value (black bar indicates 10 mM glucose stimulus)

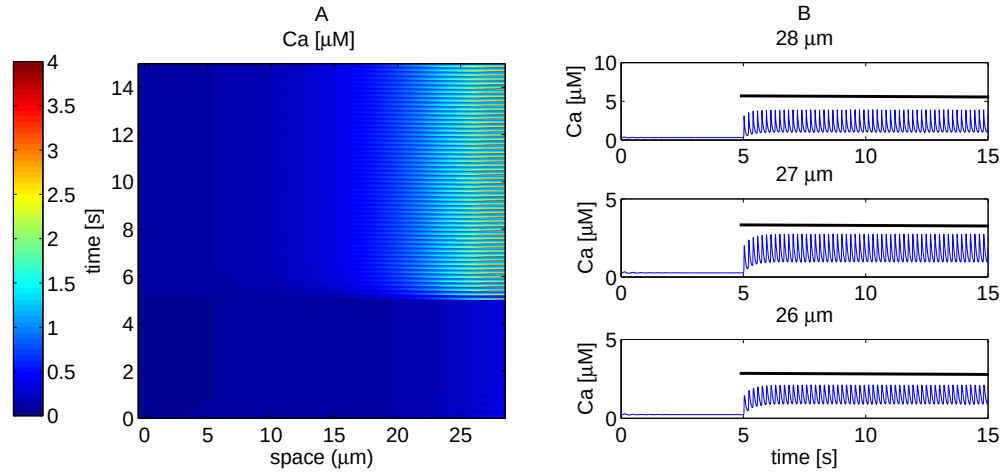

Figure 5.4.3: Simulation of intracellular Ca^{2+} concentration with default parameters. SGLT1-substrate concentration $[G]_{out}$ changing from 0 mM to 10 mM and blood glucose concentration $[G]_{ext}$ changing from 1 mM to 10 mM. A) intracellular Ca^{2+} concentration as a function of time and space (color coded in μM). B) Intracellular Ca^{2+} concentration at different space location $x = 28, 27, 26$ μm (black bar indicates 10 mM glucose stimulus).

with phloretin as performed in experiments [97, 102]. Simulation results show that the cell depolarizes when stimulated with glucose, Fig. 5.4.4, with no evident differences compared to the previous simulations (Fig. 5.1.1). Contrary, when we focus on the intracellular glucose concentration, Fig. 5.4.5, a conspicuous reduction of glucose elevation is observed (∼4-fold). This result, in compliance with experimental results [97], suggests that the major responsible for the glucose transportation inside the cell is GLUT2 transporter, however, depolarization is not affected by its inhibition implying a marginal role of K(ATP)-channels in triggering electrical activity. Cell membrane depolarization opens the Ca^{2+} channels as shown in Fig. 5.4.6 and Ca^{2+} enters inside the cell in the same amount as when GLUT2 is not inhibited.

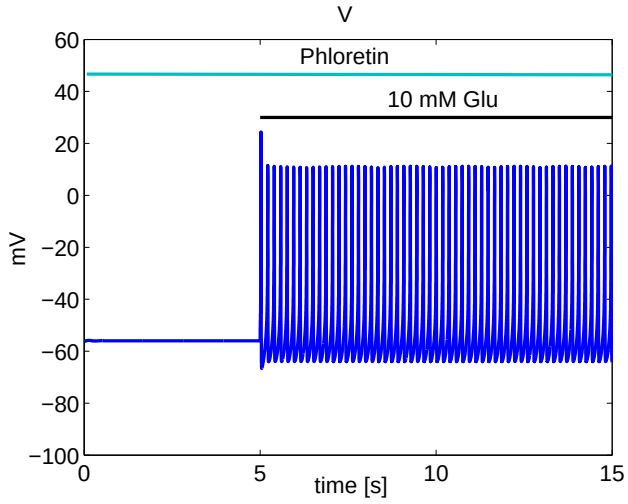

Figure 5.4.4: Simulation of membrane potential with default parameters and GLUT2 inhibition ($D_{G_{glut2}}$=0. SGLT1-substrate concentration $[G]_{out}$ changing from 0 mM to 10 mM and blood glucose concentration $[G]_{ext}$ changing from 1 mM to 10 mM.

Role of GLUT2 transporter

Finally, we analyze the contribution of the glucose-sensing mechanism mediated by the GLUT2 by simulating inhibition of SGLT1 transporter

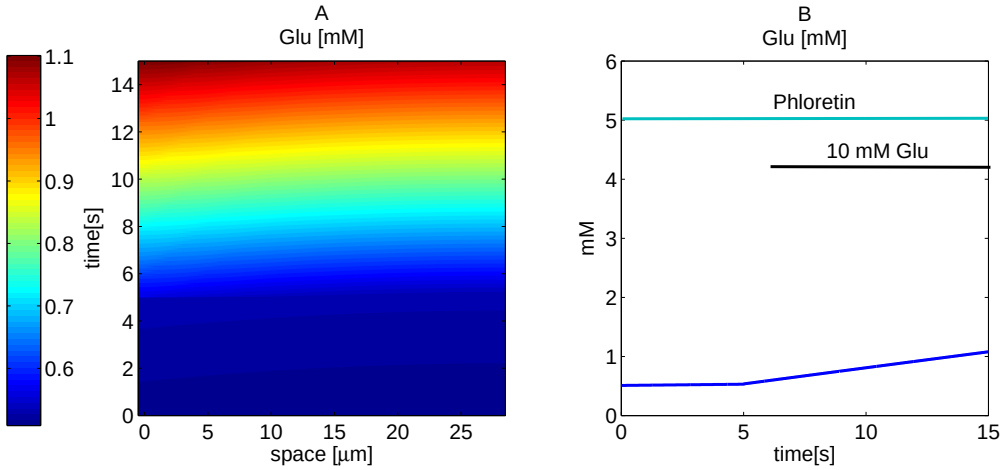

Figure 5.4.5: Simulation of intracellular glucose concentration with default parameters and GLUT2 inhibition ($D_{G_{glut2}}$=0). SGLT1-substrate concentration $[G]_{out}$ changing from 0 mM to 10 mM and blood glucose concentration $[G]_{ext}$ changing from 1 mM to 10 mM. A) intracellular glucose concentration as a function of time and space (color coded in mM). B) Intracellular glucose mean value (black bar indicates 10 mM glucose stimulus and light blue bar indicates SGLT1 blockage with phloridzin)

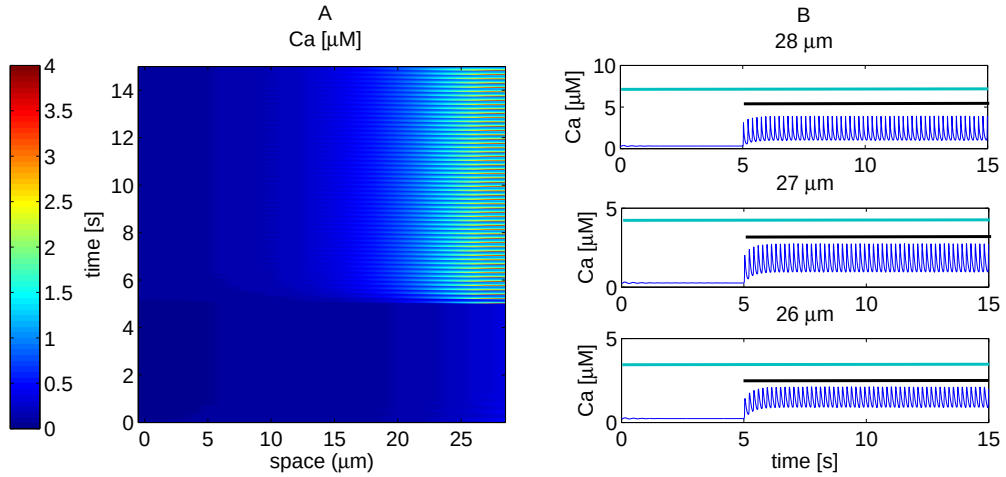

Figure 5.4.6: Simulation of intracellular Ca^{2+} concentration with default parameters and and GLUT2 inhibition ($D_{G_{glut2}}$=0. SGLT1-substrate concentration $[G]_{out}$ changing from 0 mM to 10 mM and blood glucose concentration $[G]_{ext}$ changing from 1 mM to 10 mM. A) intracellular Ca^{2+} concentration as a function of time and space (color coded in μM). B) Intracellular Ca^{2+} concentration at different space location $x = 28, 27, 26$ μm (black bar indicates 10 mM glucose stimulus).

with phloridzin. Experimentally, the presence of phloridzin does not substantially affect the glucose entrance into the cell and elevation in the intracellular glucose concentration is still observed in primary L-cells [97]. In agreement with this finding, our simulation shows a slightly reduction in the intracellular glucose elevation, Fig. 5.4.8. On the other hand, with blockage of SGLT1, the associated inward current is no longer generated and the cell is not able to depolarize (Fig. 5.4.7). Since the intracellular glucose rise is not considerably altered, the model would suggest that glucose metabolism alone is not sufficient to trigger electrical activity. In support of this hypothesis, Fig 5.4.10 and Fig. 5.4.11 show that even though higher glucose levels are reached (4 mM as without SGLT1 inhibition) by stimulating with glucose for prolonged time (20 s of simulations), no cell depolarization occurs. As a consequence of no depolarization, no Ca^{2+} enters from the voltage-gated Ca^{2+} channels as shown in Fig. 5.4.9. Therefore, the model predicts the effect of phloridzin on cytosolic Ca^{2+} in a polarized L-cell, and simulation results are consistent with observations in mice *sglt1* knockout where glucose stimulus with 10 mM does not trigger a rise in cytosolic Ca^{2+}[97].

GLP-1 SECRETION

We now use the Ca^{2+} and ATP concentrations at the basolateral side of the cell, where granules ready for exocytosis are likely to be located, to drive the exocytosis model in order to understand the roles of both transporters coupled to GLP-1 secretion. Hence, we first simulate exocytosis in normal conditions, where both mechanisms, electrogenic sodium/glucose transporter and electroneutral GLUT2-mediated glucose transport, are acting. We next investigate the effect on GLP-1 exocytosis when one of the two mechanisms is impaired. Summery of GLP-1 exocytosis results are shown in Fig. 5.4.12. The aim is to compare GLP-1 secretion in the

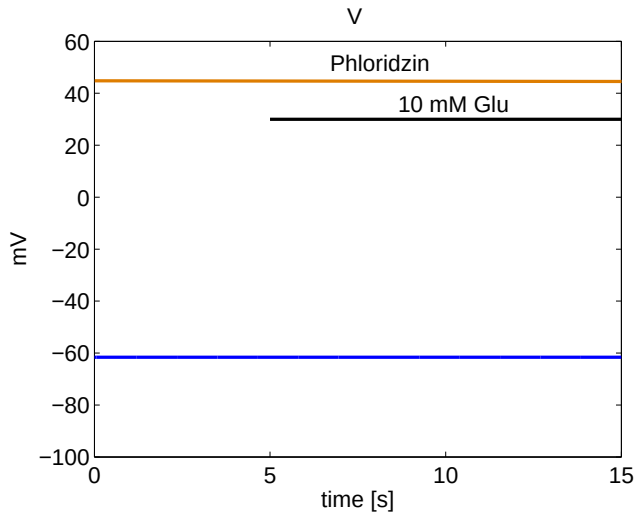

Figure 5.4.7: Simulation of membrane potential with default parameters and SGLT inhibition (n=0). Blood glucose concentration $[G]_{ext}$ changing from 1 mM to 10 mM (black bar indicates 10 mM glucose stimulus and orange bar indicates SGLT1 blockage with phloridzin).

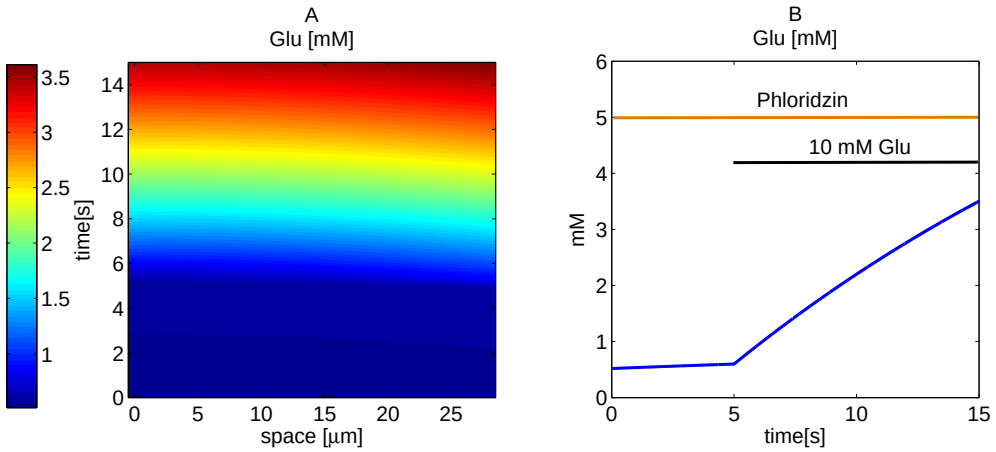

Figure 5.4.8: Simulation of intracellular glucose concentration with default parameters and SGLT inhibition (n=0). SGLT1-substrate concentration $[G]_{out}$ changing from 0 mM to 10 mM and blood glucose concentration $[G]_{ext}$ changing from 1 mM to 10 mM. A) intracellular glucose concentration as a function of time and space (color coded in mM). B) Intracellular glucose mean value (black bar indicates 10 mM glucose stimulus and orange bar indicates SGLT1 blockage with phloridzin).

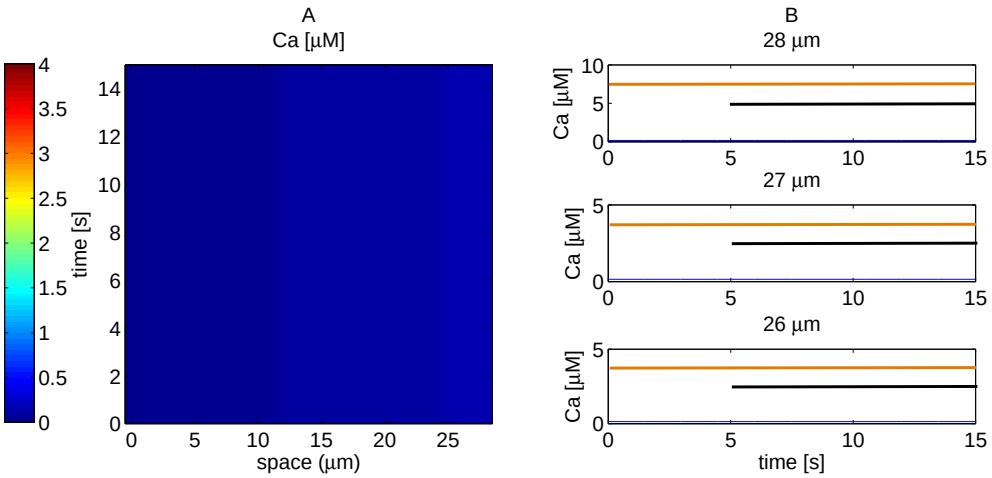

Figure 5.4.9: Simulation of intracellular Ca^{2+} concentration with default parameters and and SGLT inhibition (n=0). SGLT1-substrate concentration $[G]_{out}$ changing from 0 mM to 10 mM and blood glucose concentration $[G]_{ext}$ changing from 1 mM to 10 mM. A) intracellular Ca^{2+} concentration as a function of time and space (color coded in μM). B) Intracellular Ca^{2+} concentration at different space location $x = 28, 27, 26$ μm (black bar indicates 10 mM glucose stimulus and orange bar indicates SGLT1 blockage with phloridzin).

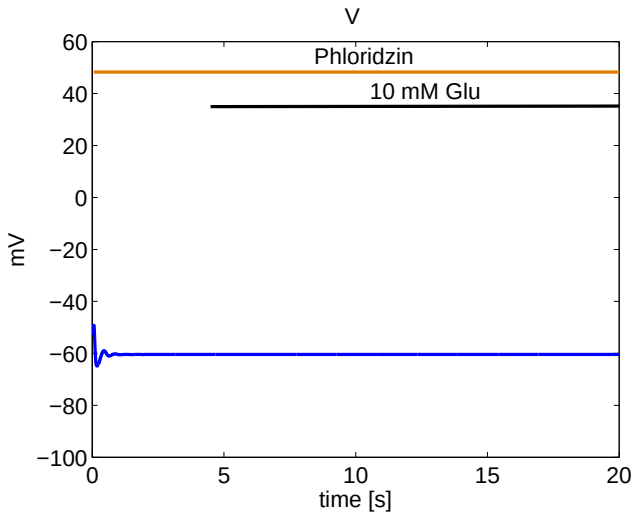

Figure 5.4.10: Simulation of electrical activity triggered by glucose stimulus with default parameters and SGLT inhibition (n=0). Blood glucose concentration $[G]_{ext}$ changing from 1 mM to 10 mM (black bar indicates 10 mM glucose stimulus and orange bar indicates SGLT1 blockage with phloridzin).

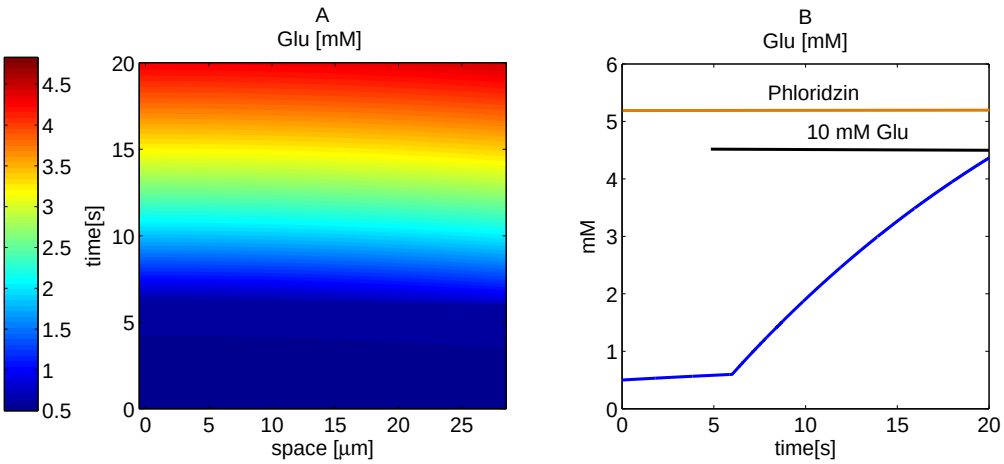

Figure 5.4.11: Simulation of intracellular glucose concentration with default parameters and SGLT inhibition (n=0). SGLT1-substrate concentration $[G]_{out}$ changing from 0 mM to 10 mM and blood glucose concentration $[G]_{ext}$ changing from 1 mM to 10 mM. A) intracellular glucose concentration as a function of time and space (color coded in mM). B) Intracellular glucose mean value (black bar indicates 10 mM glucose stimulus and orange bar indicates SGLT1 blockage with phloridzin).

three different conditions (control, SGLT1 inhibition and GLUT2 inhibition). Therefore, total number of granules fused in each conditions in response to glucose stimulus are normalized to those in response of glucose stimulus in the absence of the inhibitor (100%). It can be observed that when the SGLT1 transporter is inhibited, GLP-1 secretion is reduced of ∼75% [97, 101], ascribable to the fact that glucose metabolism alone is not sufficient to trigger cell depolarization and significant elevation in Ca^{2+} concentrations. Impairment of GLUT2 transporters slightly reduces GLP-1 secretion by ∼10%, suggesting that cell depolarization is due to the SGLT transporter, though glucose metabolism still plays a minor role in determining GLP-1 secretion, consistent with experimental results [97, 102] where GLP-1 exocytosis is induced by the non metabolizable glucose analogues (α-MGP), even though in this case secretion is slightly lower than with glucose. Fig. 5.4.13 and 5.4.14 show exocytosis simulation results when the model cell is depolarized by setting V_K=0 mV and the K(ATP) channels are open ($g_{K(ATP)}$=100 ns/pF), in order to simulate cell depolarization with external K^+ and diazoxide [97]. First,

the cell is stimulated with 0, 1, 5 and 10 mM of glucose, 5.4.13, and then the cell is stimulated as the previous three different conditions (control, SGLT1 inhibition and GLUT2 inhibition), in order to evaluate the contribution of SGLT/GLUT2 transporters when exocytosis is only glucose-dependent, Fig. 5.4.14. Experimental results in GLUTag cells in [97] where cells were depolarised by KCl and diazoxide, revealed a glucose-dependent contribution affecting GLP-1 secretion. The same results are found with the model confirming a minor role of glucose metabolism in GLP-1 secretion.

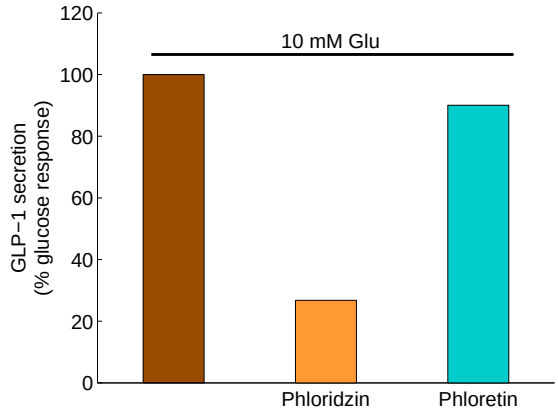

Figure 5.4.12: Exocytosis simulation results evoked by 10 mM of glucose simulating the effect of Phloretin (orange), SGLT1 transporter inhibition, and Phloridzin (light blue), GLUT2 inhibitor. Total granules released are normalized to the secretion response in the absence of inhibitors (100%).

5.5 Discussion

The relative roles of SGLT1 and GLUT2 glucose transporters underlying glucose sensing coupled to GLP1 secretion is a topic of debate. The two possible glucose-sensing pathways inducing GLP-1 secretion consist of either promotion of electrical activity by the electrogenic SGLT1 trans-

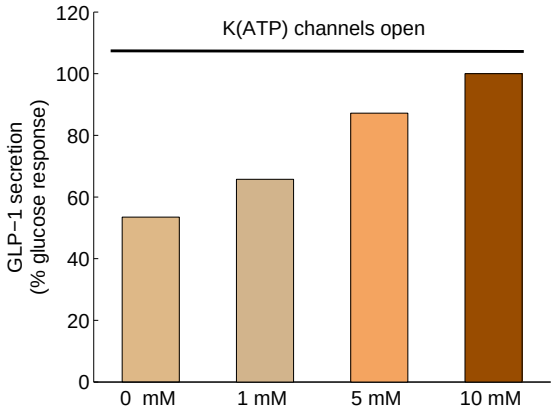

Figure 5.4.13: Exocytosis simulation results simulating cell depolarization and $g_{K(ATP)}$ opening evoked by 0, 1, 5 and 10 mM of glucose (G_{ext} and G_{out}=0, 1, 5, 10 mM) in 1 minute. Total granules released are normalized to the secretion response to 10 mM of glucose (100%).

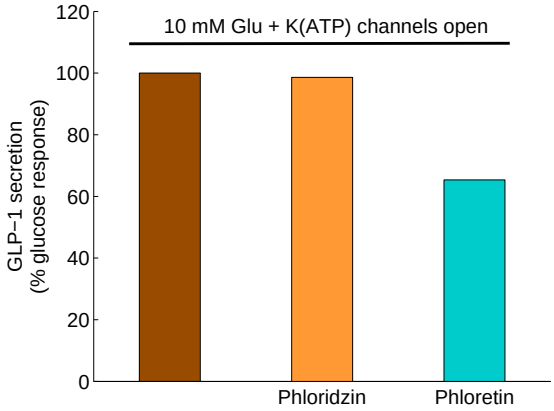

Figure 5.4.14: Exocytosis simulation results evoked by 10 mM of glucose in 1 minute and simulating cell depolarization, $g_{K(ATP)}$ opening, the effect of Phloretin (orange), and Phloridzin (light blue). Total granules released are normalized to the secretion response in the absence of inhibitors (100%).

porter or glucose metabolism that increases intracellular ATP concentrations and closes K(ATP)-channels. Studies on both primary cultured L-cells [97, 106] and GLUTag cells [95, 97] have been conducted as well as experiments with perfused rat small intestine [100, 102] to better understand how intestinal L-cells absorb glucose and evoke GLP-1 secretion.

A predominant role of SGLT1 transporter in glucose sensing mechanism has been found in L-cells in primary culture [97, 106]. However, electrophysiological differences between GLUTag cells and primary culture L-cells have been discovered and demonstrated to lead to diverse glucose-sensing mechanisms [95, 103]. Indeed, both SGLT1 currents and K(ATP)-channel closure contribute to stimulus-secretion coupling in GLUTag cells, differently to what has been found for primary L-cells. Furthermore, $in\ vivo$ studies of *sglt1* knockout mouse assessed the pivotal role of SGLT1 transporter in glucose sensing coupled to GLP-1 secretion [97].

Here we used a mathematical spatio-temporal model taking into account the cellular spatial organization to resemble the $in\ vivo$ configuration with the aim of having new insight into the glucose-sensing mechanisms involved in the L-cells. The model confims that SGLT1 is the main responsible for coupling glucose sensing to GLP-1 secretion. Its main role is to induce cell depolarization and promote glucose-triggered Ca^{2+} response. The predominant role of the SGLT1-mediated mechanism is further proven by studies reporting that non metabolisable glucose analogues, αMG, are effective stimuli of GLP-1 release $in\ vivo$ and $in\ vitro$ [95, 97, 102, 114, 117]. In isolated intestine, mimicking the *in vivo* situation, SGLT1 transporters are placed in the apical side of the cell on the luminal, side directly exposed to glucose in the intestine. Contrary, GLUT2 transporters are located at the basolateral side of the cell directly exposed to vascular system. Studies conducted on isolated intestine of *glut2* knock-out mice revealed just a reduction in GLP-1 secretion rather than a completely abolition of it [101]. Hence, $in\ vivo$ results ascribe a minor role to GLUT2 in glucose sensing. The same study conducted on isolated intestine of *sglt* knock-out mice confirms that GLP-1 secretion in absence of SGLT1 is almost completely abolished after an intragastric glu-

cose stimulus. These results certainly accredit the hypothesis of a crucial role of SGLT1 transporter in evoking GLP-1 secretion [100, 101].

Interestingly, model results show that SGLT1-mediated glucose uptake is low and intracellular glucose levels are marginally associated to this transporter. Therefore, these results advance exclusion of the metabolic mechanism controlling downstream GLP-1 secretion, at least in terms of acting on K(ATP)-channels closure and determining Ca^{2+} responses, since this mechanism alone is not sufficient to fire electrical activity.

Furthermore, our modeling results confirm the pivotal role of SGLT1 transporter in glucose sensing coupled to GLP-1 secretion, since it triggers the depolarization of the cell, according to experimental results both in $in\ vivo$ and $in\ vitro$. Depolarization opens voltage-gated Ca^{2+} channels, thus elevating Ca^{2+} concentrations, which induces exocytosis. Furthermore, model results suggest that the metabolic closure of K(ATP)-channels alone is insufficient to trigger electrical activity. Finally, metabolism might still have a role in facilitating exocytosis together with Ca^{2+} elevations. Exocytosis model supports this hypothesis since it takes into account both Ca^{2+} and ATP contribution over the total exocytosis rate and model results are consistent with both $in\ vivo$ and $in\ vitro$ recent observations [97, 101]. In particular, Parker et al. [97] observed a glucose-dependent amplification of secretion when the GLUTag cells are depolarized by KCl and diazoxide and stimulated with glucose. However, this amplification is reduced in presence of phloretin as a consequence of a reduction in glucose uptake mediated by GLUT2 and supporting the hypotheses that glucose metabolism facilitates exocytosis. In order to test this hypothesis with the model, we simulated the same experimental setting, and exocytosis resulted slightly reduced whith GLUT2 transporter blockage, while exocytosis was not affected by SGLT1 blockage, in agreement with [97].

6
Conclusions

The endocrine secretory system plays a fundamental role in regulating the body's machine. Among all the crucial tasks in which the system is involved, some endocrine cells have the specific responsibility of maintaining background levels of cell metabolism and euglycemia. Regulation of the blood glucose is the result of a complex network of mechanisms controlled by different cell types. A widespread disease that affects blood glucose concentration homeostasis is Diabetes. The number of people affected by such condition is continuously increasing due to the lifestyle, age, obesity and other reasons and it is becoming a social and economical problem because of its long-term complications. In light of the importance of understanding the different aspects of this disease, numerous efforts have been made to study the mechanisms implied.

Although euglycemia is a results of a complex feedback system, insulin hormone secreted by pancreatic β-cells is at the base of this system. Insulin is secreted in response to blood glucose elevations and it induces

other cells to metabolize glucose, thus bringing blood glucose back to the physiological steady state level. Another important hormone involved in controlling euglycemia is GLP-1 hormone secreted by intestinal L-cells, responsible of the incretin effect, and in advanced type 2 diabetes both insulin and GLP-1 are diminished.

On the other hand, cells of the pituitary gland are involved in the secretion of an ample type of hormones that act on other tissues and cells regulating growth, reproduction, behavior, temperature, and water intake. Unfortunately, the knowledge about the stimulus-secretion mechanism in these cells is still poorly understood and of extremely interest since the importance of pituitary hormones.

This Thesis focused on different aspects of the mechanism stimulus-secretion in these three main categories of endocrine cells. The aim of the work was to use a combination of modeling and experiments to better understand and investigate the stimulus-secretion system.

ROS AND CALCIUM OSCILLATIONS IN β-CELL

Insulin is secreted in distinct pulses [26, 27] and it has been suggested that disturbances in this pulsatile release might be an early marker of diabetes [28]. Pulsatile insulin is the result of oscillations in electrical activity and cytosolic Ca^{2+} levels. ROS as well as RNS species have been under investigation because of their presumable dual effect on insulin secretion: ROS/RNS can damage the cell and therefore abolish insulin release, on contrary they can stimulate short-term effect on insulin release.

In this Thesis ROS/RNS effect on a widely used insulin-secreting MIN6 β-cell line has been investigated. We focused on the mechanisms that generate Ca^{2+} oscillations disturbances induced by both moderate and elevated ROS/RNS amounts. In particular, a mathematical model of Ca^{2+} handling have been adapted to MIN6 cells to guide the interpretation of our experimental results. The limited knowledge of MIN6 cell electrophysiology prevents the construction of a bottom-up, data-driven model, in contrast to what has been realized for example for human β-cells [118].

However, the mathematical model was able to support and interpret experimental result conclusions.

We concluded that moderate ROS/RNS levels influence Ca^{2+} oscillations via inhibition of SERCA pumps and/or by increasing activity of ER release channels (IP3Rs/RyRs), all known targets of ROS/RNS [35, 39]. In addition, the model allowed us to advanced the hypothesis that high amounts of ROS/RNS also act on Ca^{2+} handling components at the plasma membrane, e.g. by inhibiting PMCAs, another ROS/RNS target [35, 39], which abolishes Ca^{2+} oscillations.

Calcium and granule dynamics in Pituitary cells

Endocrine pituitary cells are electrically excitable and often cell depolarization induces intracellular Ca^{2+} concentration elevations underlying hormone secretion. Pituitary cells show differences in the electrical activity due to differences in the ionic conductances. Specifically, two common electrical activities have been observed: continuous spiking, in luteinizing hormone-secreting gonadotrophs under basal conditions, and pseudo-plateau bursting, in prolactin-secreting lactotrophs, growth hormone-releasing somatotrophs, and ACTH-secreting corticotrophs [59]. Simultaneously measurement of electrical activity, Ca^{2+} and release from a single cell should be performed in order experimentally test this hypothesis, however it is barely realizable on single cell.

In this Thesis, a hybrid experimental/modeling approach has been exploited to explore the hypothesis that bursting cells release more hormone than spiking cells. We built a mathematical model of stochastic Ca^{2+} channel activity, Ca^{2+} diffusion and binding to buffer, and finally Ca^{2+}-driven exocytosis. Direct measurement of electrical spiking and bursting patterns from the same cell were obtained by pharmacologically blocking the large conductance potassium (BK) current from a bursting cell, or adding a BK current to a spiking cell via dynamic clamp. Experimental recordings were used as input to the mathematical model.

The modeling results showed the superiority of bursting compare to

spiking in evoking pituitary hormone release due to the fact that both local and global Ca^{2+} are augmented. Therefore, these results showed that this switch to bursting may improve the effect of hypothalamic stimulating neurohormones in increasing pituitary hormone secretion.

L-CELL SPATIAL MODEL AND GLP-1 SECRETION

The stimulus-secretion pathway in L-cells is still poorly understood and topic of debate. It is known that GLP-1 secreting cells can sense glucose in two possible pathways, promoting the electrical activity either by the electrogenic SGLT1 transporter or by K(ATP)-channels closure induced by glucose metabolism. Moreover, an important aspect to take into account is the spatial organization of the cell. Indeed, it was found that GLUT2 is located at the basolateral side, while SGLT1 is located at the apical side [101].

In this Thesis, the model of the electrical activity of primary cell [118] has been incorporated in a first spatial model of L-cell and coupled to a simple exocytosis model with the aim of investigating the glucose-sensing mechanisms and the role of the two transporters. The spatial model included glucose transportation through the SGLT1 in the apical side as well as GLUT2 in the basolateral, and diffusion; voltage activity in response to glucose transportation or/and metabolism; Ca^{2+} and Na^{+} dynamics. We validated the model by simulating the setting of the experiments conducted in [97, 102].

The model confirmed, in compliance with experimental results, that glucose transportation inside the cell through SGLT1 transporter induces Ca^{2+} influx and release of GLP-1 thanks to depolarization, while glucose metabolism alone is not sufficient to evoke depolarization, resulting in a lower GLP-1 secretion, and suggesting a marginal, but still participating, role of GLUT2 for GLP-1 secretion. It allowed us to simulate spatiotemporal dynamics in a polarized cell, the physiologically relevant situation, which is however still not possible to investigate experimentally.

Bibliography

[1] S. Misler, "Unifying concepts in stimulus-secretion coupling in endocrine cells and some implications for therapeutics.," *Advances in physiology education*, vol. 33, pp. 175–86, sep 2009.

[2] G. Wilcox, "Insulin and insulin resistance.," *The Clinical Biochemist Reviews*, vol. 26, no. 2, pp. 19–39, 2005.

[3] P. Rorsman and E. Renström, "Insulin granule dynamics in pancreatic beta cells.," *Diabetologia*, vol. 46, pp. 1029–45, aug 2003.

[4] J. J. Holst, "The physiology of glucagon-like peptide 1.," *Physiological reviews*, vol. 87, pp. 1409–39, oct 2007.

[5] American Diabetes Association, "Diagnosis and Classification of Diabetes Mellitus," *Diabetes Care*, vol. 27, no. Supplement 1, pp. S5–S10, 2004.

[6] B. B. Tripathy, H. B. Chandalia, and A. K. Das, *RSSDI Textbook of Diabetes Mellitus*. JP Medical Ltd, 2012.

[7] M. J. Fowler, "Hypoglycemia," *Clinical Diabetes*, vol. 26, pp. 170–173, oct 2008.

[8] F. M. Gribble, "RD Lawrence Lecture 2008: Targeting GLP-1 release as a potential strategy for the therapy of Type 2 diabetes.," *Diabetic medicine : a journal of the British Diabetic Association*, vol. 25, pp. 889–94, aug 2008.

[9] N. J. W. Albrechtsen, R. E. Kuhre, C. F. Deacon, and J. J. Holst, "Targeting the intestinal L-cell for obesity and type 2 diabetes treatment," *Expert Review of Endocrinology & Metabolism*, vol. 9, no. 1, pp. 61–72, 2014.

[10] S. S. Stojilkovic, J. Tabak, and R. Bertram, "Ion channels and signaling in the pituitary gland," *Endocrine Reviews*, vol. 31, pp. 845–915, 2010.

[11] R. Bertram, J. Tabak, and N. Toporikova, "Models of hypothalamus," *Scholarpedia*, vol. 1, p. 1330, dec 2006.

[12] R. D. Burgoyne and A. Morgan, "Secretory granule exocytosis.," *Physiological reviews*, vol. 83, no. 2, pp. 581–632, 2003.

[13] C. S. Olofsson, S. O. Göpel, S. Barg, J. Galvanovskis, X. Ma, A. Salehi, P. Rorsman, and L. Eliasson, "Fast insulin secretion reflects exocytosis of docked granules in mouse pancreatic B-cells.," *Pflügers Archiv : European journal of physiology*, vol. 444, pp. 43–51, may 2002.

[14] S. Houy, P. Croisé, O. Gubar, S. Chasserot-Golaz, P. Tryoen-Tóth, Y. Bailly, S. Ory, M.-F. Bader, and S. Gasman, "Exocytosis and endocytosis in neuroendocrine cells: inseparable membranes!," *Frontiers in endocrinology*, vol. 4, p. 135, jan 2013.

[15] H. D. Mansvelder and K. S. Kits, "The relation of exocytosis and rapid endocytosis to calcium entry evoked by short repetitive depolarizing pulses in rat melanotropic cells.," *The Journal of neuroscience : the official journal of the Society for Neuroscience*, vol. 18, no. 1, pp. 81–92, 1998.

[16] C. P. Fall, J. M. Wagner, E. S. Marland, and J. J. Tyson, *Computational cell biology*. Springer, 2002.

[17] J. Carroll, "Nature education." http://www.nature.com.

[18] H. Lodish, A. Berk, S. L. Zipursky, P. Matsudaira, D. Baltimore, and J. Darnell, "Molecular Cell Biology," 2000.

[19] https://en.wikipedia.org/wiki/Depolarization.

[20] A. A. Sharp, M. B. O'Neil, L. Abbott, and E. Marder, "The dynamic clamp: artificial conductances in biological neurons," *Trends in Neurosciences*, vol. 16, pp. 389–394, oct 1993.

[21] L. S. Milescu, T. Yamanishi, K. Ptak, M. Z. Mogri, and J. C. Smith, "Real-time kinetic modeling of voltage-gated ion channels using dynamic clamp.," *Biophysical journal*, vol. 95, pp. 66–87, jul 2008.

[22] A. L. Hodgking and A. F. Huxley, "A quantitative description of membrane current and its application to conduction and excitation in nerve.," *The Journal of physiology*, vol. 117, pp. 500–44, aug 1952.

[23] J. Keener and J. Sneyd, *Mathematical Physiology*. Springer, 1998.

[24] B. Thorens and M. Mueckler, "Glucose transporters in the 21st Century.," *American journal of physiology. Endocrinology and metabolism*, vol. 298, pp. E141–5, feb 2010.

[25] L. Parent, S. Supplisson, D. D. Loo, and E. M. Wright, "Electrogenic properties of the cloned Na+/glucose cotransporter: II. A transport model under nonrapid equilibrium conditions.," *The Journal of membrane biology*, vol. 125, pp. 63–79, jan 1992.

[26] P. Gilon, R. M. Shepherd, and J. C. Henquin, "Oscillations of secretion driven by oscillations of cytoplasmic Ca2+ as evidences in single pancreatic islets.," *The Journal of biological chemistry*, vol. 268, pp. 22265–8, oct 1993.

[27] R. A. Ritzel, J. D. Veldhuis, and P. C. Butler, "Glucose stimulates pulsatile insulin secretion from human pancreatic islets by increasing secretory burst mass: dose-response relationships.," *The Journal of clinical endocrinology and metabolism*, vol. 88, pp. 742–7, feb 2003.

[28] N. Pørksen, "The in vivo regulation of pulsatile insulin secretion.," *Diabetologia*, vol. 45, pp. 3–20, jan 2002.

[29] A. Tengholm and E. Gylfe, "Oscillatory control of insulin secretion.," *Molecular and cellular endocrinology*, vol. 297, pp. 58–72, jan 2009.

[30] D. R. Matthews, B. A. Naylor, R. G. Jones, G. M. Ward, and R. C. Turner, "Pulsatile insulin has greater hypoglycemic effect than continuous delivery.," *Diabetes*, vol. 32, pp. 617–21, jul 1983.

[31] G. Paolisso, A. J. Scheen, D. Giugliano, S. Sgambato, A. Albert, M. Varricchio, F. D'Onofrio, and P. J. Lefèbvre, "Pulsatile insulin delivery has greater metabolic effects than continuous hormone administration in man: importance of pulse frequency.," *The Journal of clinical endocrinology and metabolism*, vol. 72, pp. 607–15, mar 1991.

[32] M. Komjati, P. Bratusch-Marrain, and W. Waldhäusl, "Superior efficacy of pulsatile versus continuous hormone exposure on hepatic

glucose production in vitro.," *Endocrinology*, vol. 118, pp. 312–9, jan 1986.

[33] A. V. Matveyenko, D. Liuwantara, T. Gurlo, D. Kirakossian, C. Dalla Man, C. Cobelli, M. F. White, K. D. Copps, E. Volpi, S. Fujita, and P. C. Butler, "Pulsatile portal vein insulin delivery enhances hepatic insulin action and signaling.," *Diabetes*, vol. 61, pp. 2269–79, sep 2012.

[34] S. Supale, N. Li, T. Brun, and P. Maechler, "Mitochondrial dysfunction in pancreatic β cells," *Trends in Endocrinology & Metabolism*, vol. 23, pp. 477–487, sep 2012.

[35] R. F. Feissner, J. Skalska, W. E. Gaum, and S.-S. Sheu, "Crosstalk signaling between mitochondrial Ca2+ and ROS.," *Frontiers in bioscience (Landmark edition)*, vol. 14, pp. 1197–218, jan 2009.

[36] J. Pi, Y. Bai, Q. Zhang, V. Wong, L. M. Floering, K. Daniel, J. M. Reece, J. T. Deeney, M. E. Andersen, B. E. Corkey, and S. Collins, "Reactive Oxygen Species as a Signal in Glucose- Stimulated Insulin Secretion," *Diabetes*, vol. 56, pp. 1783–1791, Jul 2007.

[37] S. Collins, J. Pi, and E. Yehuda-Shnaidman, "Uncoupling and reactive oxygen species (ROS)–a double-edged sword for β-cell function? "Moderation in all things".," *Best practice & research. Clinical endocrinology & metabolism*, vol. 26, pp. 753–8, dec 2012.

[38] Y. Kaneko, T. Ishikawa, S. Amano, and K. Nakayama, "Dual effect of nitric oxide on cytosolic Ca2+ concentration and insulin secretion in rat pancreatic beta-cells.," *American journal of physiology. Cell physiology*, vol. 284, pp. C1215–22, may 2003.

[39] C. Hidalgo and P. Donoso, "Crosstalk between calcium and redox signaling: from molecular mechanisms to health implications.," *Antioxidants & redox signaling*, vol. 10, pp. 1275–312, jul 2008.

[40] P. Bernardi and A. Rasola, "Calcium and cell death: the mitochondrial connection.," *Sub-cellular biochemistry*, vol. 45, pp. 481–506, jan 2007.

[41] C. Tang, K. Koulajian, I. Schuiki, L. Zhang, T. Desai, A. Ivovic, P. Wang, C. Robson-Doucette, M. B. Wheeler, B. Minassian, A. Volchuk, and A. Giacca, "Glucose-induced beta cell dysfunction

in vivo in rats: link between oxidative stress and endoplasmic reticulum stress.," *Diabetologia*, vol. 55, pp. 1366–79, may 2012.

[42] C. S. Foote, "Definition of type I and type II photosensitized oxidation.," *Photochemistry and photobiology*, vol. 54, p. 659, nov 1991.

[43] S. Gupta, N. Ahmad, and H. Mukhtar, "Involvement of nitric oxide during phthalocyanine (Pc4) photodynamic therapy-mediated apoptosis.," *Cancer research*, vol. 58, pp. 1785–8, may 1998.

[44] V. H. C. Silva, M. P. Martins, H. C. B. de Oliveira, and A. J. Camargo, "Theoretical investigation of nitric oxide interaction with aluminum phthalocyanine.," *Journal of molecular graphics & modelling*, vol. 29, pp. 777–83, apr 2011.

[45] B. Calì, S. Ceolin, F. Ceriani, M. Bortolozzi, H. R. Agnellini, V. Zorzi, A. Predonzani, and V. Bronte, "Critical role of gap junction communication , calcium and nitric oxide signaling in bystander responses to focal photodynamic injury," *Oncotarget*, vol. 6, no. 12, 2015.

[46] H. Ishihara, T. Asano, K. Tsukuda, H. Katagiri, K. Inukai, M. Anai, M. Kikuchi, Y. Yazaki, J. I. Miyazaki, and Y. Oka, "Pancreatic beta cell line MIN6 exhibits characteristics of glucose metabolism and glucose-stimulated insulin secretion similar to those of normal islets.," *Diabetologia*, vol. 36, pp. 1139–45, nov 1993.

[47] L. R. Landa, M. Harbeck, K. Kaihara, O. Chepurny, K. Kitiphongspattana, O. Graf, V. O. Nikolaev, M. J. Lohse, G. G. Holz, and M. W. Roe, "Interplay of Ca2+ and cAMP signaling in the insulin-secreting MIN6 beta-cell line.," *The Journal of biological chemistry*, vol. 280, pp. 31294–302, sep 2005.

[48] M. H. Lim, D. Xu, and S. J. Lippard, "Visualization of nitric oxide in living cells by a copper-based fluorescent probe.," *Nature chemical biology*, vol. 2, pp. 375–80, jul 2006.

[49] R. Bertram and A. Sherman, "A calcium-based phantom bursting model for pancreatic islets.," *Bulletin of mathematical biology*, vol. 66, pp. 1313–44, sep 2004.

[50] J. Li, H. Y. Shuai, E. Gylfe, and A. Tengholm, "Oscillations of submembrane ATP in glucose-stimulated beta cells depend on negative feedback from Ca(2+).," *Diabetologia*, vol. 56, pp. 1577–86, jul 2013.

[51] P. E. MacDonald, S. Sewing, J. Wang, J. W. Joseph, S. R. Smukler, G. Sakellaropoulos, J. Wang, M. C. Saleh, C. B. Chan, R. G. Tsushima, A. M. F. Salapatek, and M. B. Wheeler, "Inhibition of Kv2.1 voltage-dependent K+ channels in pancreatic beta-cells enhances glucose-dependent insulin secretion.," *The Journal of biological chemistry*, vol. 277, pp. 44938–45, nov 2002.

[52] T. H. Hraha, A. B. Bernard, L. M. Nguyen, K. S. Anseth, and R. K. P. Benninger, "Dimensionality and Size Scaling of Coordinated Ca(2+) Dynamics in MIN6 β-cell Clusters.," *Biophysical journal*, vol. 106, pp. 299–309, jan 2014.

[53] Y. J. Liu, a. Tengholm, E. Grapengiesser, B. Hellman, and E. Gylfe, "Origin of slow and fast oscillations of Ca2+ in mouse pancreatic islets.," *The Journal of physiology*, vol. 508 (Pt 2, pp. 471–81, apr 1998.

[54] R. Bertram, A. Sherman, and L. S. Satin, "Metabolic and electrical oscillations: partners in controlling pulsatile insulin secretion.," *American journal of physiology. Endocrinology and metabolism*, vol. 293, pp. E890–E900, 2007.

[55] A. K. Grover and S. E. Samson, "Effect of superoxide radical on Ca2+ pumps of coronary artery.," *The American journal of physiology*, vol. 255, pp. C297–303, sep 1988.

[56] M. G. Pedersen, "A biophysical model of electrical activity in human β-cells.," *Biophysical journal*, vol. 99, pp. 3200–7, nov 2010.

[57] M. Riz, M. Braun, and M. G. Pedersen, "Mathematical modeling of heterogeneous electrophysiological responses in human β-cells.," *PLoS computational biology*, vol. 10, p. e1003389, jan 2014.

[58] A. Varadi and G. A. Rutter, "Dynamic imaging of endoplasmic reticulum Ca2+ concentration in insulin-secreting MIN6 Cells using recombinant targeted cameleons: roles of sarco(endo)plasmic reticulum Ca2+-ATPase (SERCA)-2 and ryanodine receptors.," *Diabetes*, vol. 51 Suppl 1, pp. S190–201, feb 2002.

[59] S. S. Stojilkovic, H. Zemkova, and F. Van Goor, "Biophysical basis of pituitary cell type-specific Ca2+ signaling-secretion coupling.," *Trends in endocrinology and metabolism: TEM*, vol. 16, pp. 152–9, jan 2005.

[60] M. E. Freeman, B. Kanyicska, A. Lerant, and N. Gyorgy, "Prolactin: Structure , Function , and Regulation of Secretion," *Physiological Review*, vol. 80, no. 4, pp. 1523–1631, 2000.

[61] F. Van Goor, D. Zivadinovic, A. J. Martinez-Fuentes, and S. S. Stojilkovic, "Dependence of pituitary hormone secretion on the pattern of spontaneus voltage-gated calcium influx. Cell type-specific action potential secretion coupling," *Journal of Biological Chemistry*, vol. 276, pp. 33840–33846, 2001.

[62] F. Van Goor, D. Zivadinovic, and S. S. Stojilkovic, "Differential expression of ionic channels in rat anterior pituitary cells.," *Molecular endocrinology (Baltimore, Md.)*, vol. 15, no. January, pp. 1222–1236, 2001.

[63] F. Van Goor, Y.-X. Li, and S. S. Stojilkovic, "Paradoxical Role of Large-Conductance Calcium-Activated K+ (BK) Channels in Controlling Action Potential-Driven Ca2+ Entry in Anterior Pituitary Cells," *J. Neurosci.*, vol. 21, pp. 5902–5915, aug 2001.

[64] A. H. Tashjian, Y. Yasumura, L. Levine, G. H. Sato, and M. L. Parker, "Establishment of clonal strains of rat pituitary tumor cells that secrete growth hormone.," *Endocrinology*, vol. 82, pp. 342–52, feb 1968.

[65] J. Tabak, A. E. Gonzalez-Iglesias, N. Toporikova, R. Bertram, and M. E. Freeman, "Variations in the response of pituitary lactotrophs to oxytocin during the rat estrous cycle.," *Endocrinology*, vol. 151, pp. 1806–13, apr 2010.

[66] A. Tse and B. Hille, "GnRH-induced Ca2+ oscillations and rhythmic hyperpolarizations of pituitary gonadotropes," *Science*, vol. 255, pp. 462–464, jan 1992.

[67] J. M. Dubinsky and G. S. Oxford, "Ionic currents in two strains of rat anterior pituitary tumor cells.," *The Journal of general physiology*, vol. 83, pp. 309–39, mar 1984.

[68] J. A. Keja and K. S. Kits, "Single-channel properties of high- and low-voltage-activated calcium channels in rat pituitary melanotropic cells.," *Journal of neurophysiology*, vol. 71, pp. 840–55, mar 1994.

[69] S. Hagiwara and H. Ohmori, "Studies of single calcium channel currents in rat clonal pituitary cells.," *The Journal of physiology*, vol. 336, pp. 649–61, mar 1983.

[70] K. S. Kits and H. D. Mansvelder, "Regulation of exocytosis in neuroendocrine cells: Spatial organization of channels and vesicles, stimulus-secretion coupling, calcium buffers and modulation," *Brain Research Reviews*, vol. 33, pp. 78–94, 2000.

[71] A. Sherman, J. Keizer, and J. Rinzel, "Domain model for Ca2(+)-inactivation of Ca2+ channels at low channel density.," *Biophysical journal*, vol. 58, pp. 985–95, oct 1990.

[72] N. L. Allbritton, T. Meyer, and L. Stryer, "Range of messenger action of calcium ion and inositol 1,4,5-trisphosphate.," *Science (New York, N.Y.)*, vol. 258, pp. 1812–5, dec 1992.

[73] V. Matveev, R. S. Zucker, and A. Sherman, "Facilitation through buffer saturation: constraints on endogenous buffering properties.," *Biophysical journal*, vol. 86, no. May, pp. 2691–2709, 2004.

[74] Y.-d. Chen, S. Wang, and A. Sherman, "Identifying the targets of the amplifying pathway for insulin secretion in pancreatic beta-cells by kinetic modeling of granule exocytosis.," *Biophysical journal*, vol. 95, no. 5, pp. 2226–2241, 2008.

[75] K. S. Kits, T. a. de Vlieger, B. W. Kooi, and H. D. Mansvelder, "Diffusion barriers limit the effect of mobile calcium buffers on exocytosis of large dense cored vesicles.," *Biophysical journal*, vol. 76, no. 3, pp. 1693–1705, 1999.

[76] T. Voets, "Dissection of Three Ca2+-Dependent Steps Leading to Secretion in Chromaffin Cells from Mouse Adrenal Slices," *Neuron*, vol. 28, pp. 537–545, nov 2000.

[77] P. Thomas, J. G. Wong, a. K. Lee, and W. Almers, "A low affinity Ca2+ receptor controls the final steps in peptide secretion from pituitary melanotrophs.," *Neuron*, vol. 11, pp. 93–104, 1993.

[78] P. Thomas, a. Surprenant, and W. Almers, "Cytosolic Ca2+, exocytosis, and endocytosis in single melanotrophs of the rat pituitary.," *Neuron*, vol. 5, no. 5, pp. 723–733, 1990.

[79] M. G. Pedersen, G. Cortese, and L. Eliasson, "Mathematical modeling and statistical analysis of calcium-regulated insulin granule exocytosis in beta-cells from mice and humans," *Progress in Biophysics and Molecular Biology*, vol. 107, no. 2, pp. 257–264, 2011.

[80] S. S. Stojilkovic, "Pituitary cell type-specific electrical activity, calcium signaling and secretion," *Biological Research*, vol. 39, no. 3, pp. 403–423, 2006.

[81] P. J. Duncan, S. Sengul, J. Tabak, P. Ruth, R. Bertram, and M. J. Shipston, "Large conductance Ca(2+) -activated K(+) channels (BK) promote secretagogue-induced transition from spiking to bursting in murine anterior pituitary corticotrophs.," *The Journal of physiology*, vol. 593, pp. 1197–1211, dec 2015.

[82] N. Vardjan, J. Jorgačevski, M. Stenovec, M. Kreft, and R. Zorec, "Compound exocytosis in pituitary cells," *Annals of the New York Academy of Sciences*, vol. 1152, pp. 63–75, 2009.

[83] R. Zorec, S. K. Sikdar, and W. T. Mason, "Increased cytosolic calcium stimulates exocytosis in bovine lactotrophs. Direct evidence from changes in membrane capacitance.," *The Journal of general physiology*, vol. 97, no. March 1991, pp. 473–497, 1991.

[84] J. Klingauf and E. Neher, "Modeling Buffered Ca2+ Diffusion Near the Membrane," *Biophysical Journal*, vol. 72, pp. 674–690, feb 1997.

[85] S. Barg, X. Ma, L. Eliasson, J. Galvanovskis, S. O. Göpel, S. Obermüller, J. Platzer, E. Renström, M. Trus, D. Atlas, J. Striessnig, and P. Rorsman, "Fast exocytosis with few Ca(2+) channels in insulin-secreting mouse pancreatic B cells.," *Biophysical journal*, vol. 81, pp. 3308–23, dec 2001.

[86] R. Bertram, G. D. Smith, and A. Sherman, "Modeling study of the effects of overlapping Ca2+ microdomains on neurotransmitter release.," *Biophysical journal*, vol. 76, pp. 735–50, feb 1999.

[87] J. Tabak, M. Tomaiuolo, a. E. Gonzalez-Iglesias, L. S. Milescu, and R. Bertram, "Fast-Activating Voltage- and Calcium-Dependent Potassium (BK) Conductance Promotes Bursting in Pituitary Cells: A Dynamic Clamp Study," *Journal of Neuroscience*, vol. 31, no. 46, pp. 16855–16863, 2011.

[88] Y. X. Li, J. Rinzel, L. Vergara, and S. S. Stojilković, "Spontaneous electrical and calcium oscillations in unstimulated pituitary gonadotrophs.," *Biophysical journal*, vol. 69, pp. 785–95, sep 1995.

[89] L. Wildt, A. Häusler, G. Marshall, J. S. Hutchison, T. M. Plant, P. E. Belchetz, and E. Knobil, "Frequency and amplitude of gonadotropin-releasing hormone stimulation and gonadotropin secretion in the rhesus monkey.," *Endocrinology*, vol. 109, pp. 376–85, aug 1981.

[90] P. Mollard and W. Schlegel, "Why are endocrine pituitary cells excitable?," *Trends in Endocrinology & Metabolism*, vol. 7, pp. 361–365, dec 1996.

[91] S. Misler, D. W. Barnett, K. D. Gillis, and D. M. Pressel, "Electrophysiology of stimulus-secretion coupling in human beta-cells.," *Diabetes*, vol. 41, pp. 1221–8, oct 1992.

[92] M. Nauck and U. Smith, "Incretin-based therapy: how do incretin mimetics and DPP-4 inhibitors fit into treatment algorithms for type 2 diabetic patients?," *Best practice & research. Clinical endocrinology & metabolism*, vol. 23, pp. 513–23, aug 2009.

[93] F. M. Gribble, L. Williams, A. K. Simpson, and F. Reimann, "A Novel Glucose-Sensing Mechanism Contributing to Glucagon-Like Peptide-1 Secretion From the GLUTag Cell Line," *Diabetes*, vol. 52, pp. 1147–1154, may 2003.

[94] F. M. Ashcroft and P. Rorsman, "Electrophysiology of the pancreatic β-cell," *Progress in Biophysics and Molecular Biology*, vol. 54, pp. 87–143, jan 1989.

[95] F. Reimann and F. M. Gribble, "Glucose-Sensing in Glucagon-Like Peptide-1-Secreting Cells," *Diabetes*, vol. 51, pp. 2757–2763, sep 2002.

[96] D. O'Malley, F. Reimann, A. K. Simpson, and F. M. Gribble, "Sodium-coupled glucose cotransporters contribute to hypothalamic glucose sensing.," *Diabetes*, vol. 55, pp. 3381–6, dec 2006.

[97] H. E. Parker, A. Adriaenssens, G. Rogers, P. Richards, H. Koepsell, F. Reimann, and F. M. Gribble, "Predominant role of active versus facilitative glucose transport for glucagon-like peptide-1 secretion.," *Diabetologia*, vol. 55, pp. 2445–55, sep 2012.

[98] F. Reimann, M. Maziarz, G. Flock, A. M. Habib, D. J. Drucker, and F. M. Gribble, "Characterization and functional role of voltage gated cation conductances in the glucagon-like peptide-1 secreting GLUTag cell line.," *The Journal of physiology*, vol. 563, pp. 161–75, feb 2005.

[99] G. J. Rogers, G. Tolhurst, A. Ramzan, A. M. Habib, H. E. Parker, F. M. Gribble, and F. Reimann, "Electrical activity-triggered glucagon-like peptide-1 secretion from primary murine L-cells.," *The Journal of physiology*, vol. 589, pp. 1081–93, mar 2011.

[100] V. Gorboulev, A. Schürmann, V. Vallon, H. Kipp, A. Jaschke, D. Klessen, A. Friedrich, S. Scherneck, T. Rieg, R. Cunard, M. Veyhl-Wichmann, A. Srinivasan, D. Balen, D. Breljak, R. Rexhepaj, H. E. Parker, F. M. Gribble, F. Reimann, F. Lang, S. Wiese, I. Sabolic, M. Sendtner, and H. Koepsell, "Na(+)-D-glucose cotransporter SGLT1 is pivotal for intestinal glucose absorption and glucose-dependent incretin secretion.," *Diabetes*, vol. 61, pp. 187–96, jan 2012.

[101] P. V. Röder, K. E. Geillinger, T. S. Zietek, B. Thorens, H. Koepsell, and H. Daniel, "The role of SGLT1 and GLUT2 in intestinal glucose transport and sensing.," *PloS one*, vol. 9, p. e89977, jan 2014.

[102] R. E. Kuhre, C. R. Frost, B. Svendsen, and J. J. Holst, "Molecular mechanisms of glucose-stimulated GLP-1 secretion from perfused rat small intestine.," *Diabetes*, vol. 64, pp. 370–82, feb 2015.

[103] M. Riz and M. G. Pedersen, "Mathematical Modeling of Interacting Glucose-Sensing Mechanisms and Electrical Activity Underlying Glucagon-Like Peptide 1 Secretion," *PLOS Computational Biology*, vol. 11, no. 12, p. e1004600, 2015.

[104] G. Magnus and J. Keizer, "Model of beta-cell mitochondrial calcium handling and electrical activity. II. Mitochondrial variables.," *The American journal of physiology*, vol. 274, pp. C1174–84, apr 1998.

[105] N. Petersen, F. Reimann, S. Bartfeld, H. F. Farin, F. C. Ringnalda, R. G. J. Vries, S. van den Brink, H. Clevers, F. M. Gribble, and E. J. P. de Koning, "Generation of L cells in mouse and human small intestine organoids.," *Diabetes*, vol. 63, pp. 410–20, mar 2014.

[106] F. Reimann, A. M. Habib, G. Tolhurst, H. E. Parker, G. J. Rogers, and F. M. Gribble, "Glucose sensing in L cells: a primary cell study.," *Cell metabolism*, vol. 8, pp. 532–9, dec 2008.

[107] K. Thorsen, T. Drengstig, and P. Ruoff, "Transepithelial glucose transport and Na+/K+ homeostasis in enterocytes: an integrative model," *AJP: Cell Physiology*, vol. 307, pp. C320–C337, jun 2014.

[108] M. Kreft, M. Lukšič, T. M. Zorec, M. Prebil, and R. Zorec, "Diffusion of D-glucose measured in the cytosol of a single astrocyte.," *Cellular and molecular life sciences : CMLS*, vol. 70, pp. 1483–92, apr 2013.

[109] H. Heimberg, A. De Vos, D. Pipeleers, B. Thorens, and F. Schuit, "Differences in Glucose Transporter Gene Expression between Rat Pancreatic - and -Cells Are Correlated to Differences in Glucose Transport but Not in Glucose Utilization," *Journal of Biological Chemistry*, vol. 270, pp. 8971–8975, apr 1995.

[110] F. Schuit, K. Moens, H. Heimberg, and D. Pipeleers, "Cellular origin of hexokinase in pancreatic islets.," *The Journal of biological chemistry*, vol. 274, pp. 32803–9, nov 1999.

[111] T. L. Jetton, Y. Liang, C. C. Pettepher, E. C. Zimmerman, F. G. Cox, K. Horvath, F. M. Matschinsky, and M. A. Magnuson, "Analysis of upstream glucokinase promoter activity in transgenic mice and identification of glucokinase in rare neuroendocrine cells in the brain and gut," *Journal of Biological Chemistry*, vol. 269, no. 5, pp. 3641–3654, 1994.

[112] P. O. Westermark and A. Lansner, "A model of phosphofructokinase and glycolytic oscillations in the pancreatic beta-cell.," *Biophysical journal*, vol. 85, pp. 126–39, jul 2003.

[113] L. F. Barros, A. San Martín, T. Sotelo-Hitschfeld, R. Lerchundi, I. Fernández-Moncada, I. Ruminot, R. Gutiérrez, R. Valdebenito, S. Ceballo, K. Alegría, F. Baeza-Lehnert, and D. Espinoza, "Small is fast: astrocytic glucose and lactate metabolism at cellular resolution.," *Frontiers in cellular neuroscience*, vol. 7, p. 27, jan 2013.

[114] U. Ritzel, A. Fromme, M. Ottleben, U. Leonhardt, and G. Ramadori, "Release of glucagon-like peptide-1 (GLP-1) by carbohydrates in the perfused rat ileum.," *Acta diabetologica*, vol. 34, pp. 18–21, mar 1997.

[115] J. Timmermans, R. Kaune, R. Bindels, and C. van Os, "Quantification of Ca2+-ATPases in porcine duodenum. Effects of 1,25(OH)2D3 deficiency," *Biochimica et Biophysica Acta (BBA) - Biomembranes*, vol. 1065, pp. 177–184, jun 1991.

[116] A. M. Babsky, S. Topper, H. Zhang, Y. Gao, J. R. James, S. K. Hekmatyar, and N. Bansal, "Evaluation of extra- and intracellular apparent diffusion coefficient of sodium in rat skeletal muscle: effects of prolonged ischemia.," *Magnetic resonance in medicine : official journal of the Society of Magnetic Resonance in Medicine / Society of Magnetic Resonance in Medicine*, vol. 59, no. 3, pp. 485–91, 2008.

[117] R. Moriya, T. Shirakura, J. Ito, S. Mashiko, and T. Seo, "Activation of sodium-glucose cotransporter 1 ameliorates hyperglycemia by mediating incretin secretion in mice.," *American journal of physiology. Endocrinology and metabolism*, vol. 297, pp. E1358–65, dec 2009.

[118] M. Riz, M. Braun, X. Wu, and M. G. Pedersen, "Inwardly rectifying Kir2.1 currents in human β-cells control electrical activity: Characterisation and mathematical modelling.," *Biochemical and biophysical research communications*, vol. 459, pp. 284–7, apr 2015.

Acknowledgments

First of all, I really would like to thank my supervisor Dr. Morten Gram Pedersen, I owe to him a lot, starting from the basic concepts about cellular mechanisms and going to the extremely important support he gave me. He always helped me with crucial advises during my PhD project.

Secondly, I would like to thank Prof. Richard Bertram for the possibility to spend a period at the Florida State University and collaborate with his research group. Thanks to him and its research group I learned more about the fascinating world of pituitary cells and I had the possibility to participate in the experiments conducted by the group. Furthermore, I would like to thank Dr. Joel Tabak and Dr. Patrick Fletcher for the support and help during my stay at the FSU.

I would like to thank Salvatore Antonucci for the experimental data of the MIN6 beta-cells and for the collaboration in the research.

I would like to thank Prof. Claudio Cobelli for the possibility to start a project with him and with his research group at the beginning of my PhD.

Above all, I would like to thank my family, especially my mother Daniela and my father Arrigo, but also my brother Andrea and my special grandmother Dina, for their unconditional love and to be always proud of me every single day. I would like to dedicate my work to them because it is only thanks to them that I could achieve this objective.

Finally, I would like to thank very much my PhD colleagues. They made these the best years ever, they made me feel part of a group, constantly supported and encouraged, even when I was physically distant. They helped me to overcome difficult times. They made me grow both from a scientific perspective, sharing ideas and discussion, but especially from the human point of view. They gave me so much and this is why the memory of these years, despite very difficult and challenging, will surely be a happy memory, thanks to them and to my supervisor.